POLITECNICO DI MILANO
DEPARTMENT OF PHYSICS
LAUREA MAGISTRALE IN ENGINEERING PHYSICS

CRYSTAL FIELD SCHEME OF THE HEAVY FERMION SYSTEM $CeRh_2As_2$ STUDIED BY MEANS OF X-RAY ABSORPTION AND X-RAY RAMAN SCATTERING SPECTROSCOPY

Master's thesis of:
Marco Magnaterra

Supervisor:
Prof. Marco Moretti

Tutor:
Dr. Christoph Sahle

Tutor:
Dr. Kurt Kummer

2018 – 2019

Grazie a tutti quelli che hanno reso questo possibile:
da Aristotele fino a mia mamma

Abstract

Heavy fermion systems are lanthanide- and actinide- based intermetallic compounds where the strong electronic correlation gives rise to a rich phase diagram and exotic physical phenomena. The description of these systems, after more than 80 years from their discovery, is still a big challenge. In this thesis the newly investigated heavy fermion system $CeRh_2As_2$ is analyzed. The goal of the research was to provide an independent determination of the crystal electric field (CEF) scheme and crystal electric field parameters acting on the rare earth Ce ion, starting with the mere knowledge of its crystal structure. The determination of the CEF scheme was carried out using x-ray absorption (XAS) at the $M_{4,5}$ edge of Ce and x-ray Raman spectroscopy (XRS) at the $N_{4,5}$ edge. The experiments were performed respectively at ID32 and ID20 of the ESRF. The symmetry reduction due to the presence of the neighbouring atoms causes the presence of a natural out of plane linear dichroism that is observed in the experimental spectra acquired with these techniques. The determination of the crystal field scheme was achieved via the comparison of the experimental spectra with atomic multiplet theory simulations performed with Quanty. Atomic models can be successfully applied in these systems due to the high localization of the $4f$ orbitals. A crystal field scheme $\Gamma_7^1 - \Gamma_6 - \Gamma_7^2$ is proposed, with a quasi-degenerate quartet ground state. In fact, the distance between the first excited state Γ_6 and the ground state Γ_7^1 is determined to be bounded between $0 \lesssim \Delta E_{76} \lesssim 6\,\mathrm{meV}$.

Sommario

I sistemi di elettroni pesanti sono materiali intermetallici a base di lantanoidi e attinoidi nei quali la forte correlazione elettronica dà origine ad un ricco diagramma di fase ed ad insoliti fenomeni fisici. Ad 80 anni dalla loro scoperta, la descrizione di questi fenomeni sta ancora mettendo alla prova le nostre conoscenze. In questa tesi è stato analizzato il nuovo sistema di elettroni pesanti $CeRh_2As_2$. Lo scopo della ricerca era di fornire una determinazione indipendente dello schema dei livelli energetici di campo elettrico cristallino (CEF) e i relativi parametri del campo elettrico cristallino che agisce sullo ione di terra rara Ce, partendo dalla conoscenza della sola struttura cristallina. La determinazione dello schema di CEF è stata raggiunta utilizzando le tecniche di spettroscopia ad assorbimento di raggi X (XAS) alla soglia $M_{4,5}$ del Ce e spettroscopia Raman di raggi X (XRS) alla soglia $N_{4,5}$. Gli esperimenti sono stati eseguiti rispettivamente all'ID32 e all'ID20 dell'ESRF. La riduzione della simmetria dovuta alla presenza degli atomi attorno allo ione causa la presenza di un dicroismo naturale lineare che è stato osservato negli spettri sperimentali acquisiti. La determinazione dello schema dei livelli di campo cristallino è stata ottenuta confrontando gli spettri sperimentali con le simulazioni, basate su una teoria di multipletti atomici, ottenute con Quanty. I modelli atomici possono essere applicati con successo in questi sistemi per via della alta localizzazione dell'orbitale $4f$. Uno schema dei livelli di campo cristallino $\Gamma_7^1 - \Gamma_6 - \Gamma_7^2$ è proposto, con lo stato fondamentale formato da un quartetto quasi-degenere. Infatti la distanza del primo stato eccitato Γ_6 dallo stato fondamentale Γ_7^1 è stata determinata essere compresa tra $0 \lesssim \Delta E_{76} \lesssim 6\,\mathrm{meV}$.

Contents

List of Figures

CHAPTER 1

Introduction

In the following chapter the exotic properties that were found on some f compounds are presented. The properties and the history of so-called heavy fermions are presented in detail in the reviews in Ref. [1–5].

1.1 Exotic properties of the f shell

Materials which contain lanthanides and actinides with unfilled $4f$ or $5f$ electron shells, belong to the class of *strongly correlated materials*, meaning that the interplay between the electrons play a fundamental role and the single non-interacting electron model is not enough to describe some of the exotic properties that these materials exhibit. The interaction between the partly filled f shell, whose electronic density is highly anisotropic, and the sea of itinerant delocalized electrons leads to a rich fauna of competing effects and of phase states. These f electrons behave as localized magnetic moments in a sea of itinerant conduction electrons. Their interaction can favor a magnetically ordered ground state when the conduction electrons mediate a coupling between the f electrons in different lattice sites via the so-called Ruderman-Kittel-Kasuya-Yoshida (RKKY) interaction [6]. But also the interaction can favor a non-magnetic state if the conduction electrons tend to screen the localized magnetic moments via the so-called Kondo screening. These effects manifest at low temperatures and their competition leads to peculiar magnetic, thermodynamic and electronic behaviour, which leads to a rich phase diagram. Varying the pressure, magnetic field or the chemical doping it is possible to tune the prevailing interaction. This behavior can be qualitatively pictured with the Doniach phase diagram as in Fig 1.1. The heavy fermion HF state rises when the Kondo effect becomes dominant and thus reduces the magnetic ordering temperature and the obtained ground state is paramagnetic and formed by strongly interacting electrons that

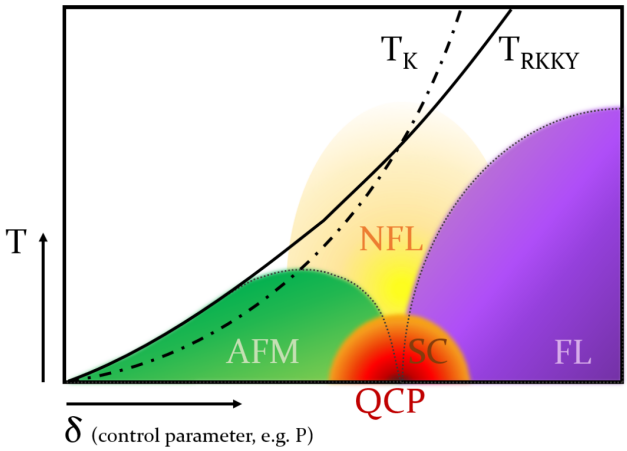

Figure 1.1: Qualitative illustration of the Doniach phase diagram: ground state as a function of the temperature and of a control parameter such as pressure or magnetic field. The Kondo and the RKKY interactions have different dependencies on these parameters. This leads to the presence of different possible ground states. Such as an antiferromagnetic (AFM) ordering where $T_{RKKY} > T_K$ or a paramagnetic Fermi liquid phase where $T_{RKKY} > T_K$. In between a quantum critical point (QCP) can arise and this leads to the presence of exotic phases such as non-Fermi liquid behaviour (NFL) and unconventional superconductivity. Figure redrawn from Ref. [7, 8].

can be described as a Fermi liquid (FL).

The ground state can be tuned through a quantum phase transition into a heavy fermion (HF) state by pressure, magnetic fields or chemical doping [7]. The HF state is a paramagnetic FL state where the Kondo interaction dominates and leads to non-ordered but interacting high effective mass electrons.

The first manifestations of the presence of heavy fermions was the discovery of the so-called Kondo effect [9]. It manifested in an anomalous rise of the resistivity as the temperature was decreased. The interaction between the conduction electrons and the localized magnetic impurity, which are the $4f$ electrons, leads to the formation of a quasi-particle state, which can be described as a conduction electron dressed with particles describing the interaction (scattering) with the localized electron. This results in an increase of the effective mass of the electron. As the temperature increases instead, the electrons become "asymptotically free" that means that they do not feel the interaction, so the f orbitals become more localized at higher temperature and the conduction electrons less heavy. Instead, decreasing the temperature, when the thermal energy is lower than the Kondo interaction energy, the interaction becomes dominant. In that case the f wave function is hybridized with the conduction electron wave function and the resulting state should be written as a combination of localized and delocalized wave functions. This results in the presence of a *mixed valence* state for the f ion.

The term heavy fermion was coined by Steglich [10] in 1976 to describe the electronic excitations in a new class of intermetallic compounds with an electronic density of states as much as 1000 times larger than copper. For example, $CeCu_2Si_2$ has a specific heat of $\gamma = 1100\,\mathrm{mJ\ mol\ K^2}$ and an effective mass of $m^* \approx 10^2 m_e$. From the first observation of this behaviour in 1975 on the compound $CeAl_3$ (Andres *et al.*, 1975 [11]) a diversity of heavy fermion compounds showing different kinds of phase states

have been discovered. A boost in the interest toward these compounds was given by the discovery of unconventional superconductivity (SC) in $CeCu_2Si_2$ where the Cooper pairs are formed by heavy electrons. This discovery proved that magnetic interactions and Cooper pairs formation are not incompatible [12]. In conventional BCS superconductors the doping with magnetic impurities leads to the suppression of the superconducting phase. On the contrary, the doping with non magnetic impurities of heavy fermion superconductors suppresses the SC phase as shown by experiments involving the chemical substitution of Ce with the non magnetic La ion [13, 14].

However, at the basis of the study of this complex phenomena the knowledge of the characteristics of the f ground state wave functions is fundamental. The interaction of the f shell with the surrounding ions in the crystal can be modeled as an *effective* crystal electric field that models the hybridization of the f orbital with the surrounding orbitals. The symmetry and the strength of this interaction strongly determines the properties of the ground state wave function of the f electrons. The significance of the characteristics of the crystal field ground state for the properties of Kondo systems was pointed out in several articles [15]. For example, Gunnarson and Christenses showed how the different crystal electric field split $4f$ states in $CeCu_2As_2$ hybridize differently with the conduction electrons and how the magnetic susceptibility is influenced by that [16]. Cerium compounds, in particular, are interesting because they show all the exotic phase states but their description is simplified by the fact that only one f electron is present since Ce is very often found as Ce^{3+} with configuration $4f^1$. This means that cerium compounds are an ideal playground for trying to understand the fundamental physics at the basis of these strongly correlated Kondo systems.

1.2 Aim of the thesis

In this thesis, the crystal field levels scheme of the new Ce-based heavy fermion system $CeRh_2As_2$ is investigated. The tools to describe the $4f$ shell and its interaction with the surrounding ions in a crystal are described in chapter 2, where the crystal electric field (CEF) model is presented. Chapter 3 describes in detail two core level spectroscopy techniques that proved to be able to give information about the crystal field and that were exploited in this thesis: x-ray absorption spectroscopy (XAS) at the $M_{4,5}$ edge and x-ray Raman scattering (XRS) spectroscopy at the $N_{4,5}$ edge. In chapter 4 it is described how the experiments were performed at ID32 and ID20 of the ESRF. In chapter 5 it is shown how it is possible to successfully simulate the experimental spectra through atomic multiplet calculations. In chapter 6 the crystal structure of $CeRh_2As_2$ is described and the XAS and XRS experimental spectra are shown. Via the comparison of the experimental data with the simulations a set of possible crystal field schemes is proposed. Finally the discussion of the results and possible ways to improve the analysis are presented in chapter 7.

CHAPTER 2

Effective crystal electric field theory

2.1 Physics of the atomic 4*f* shell

The properties of the 4*f* compounds outlined in the previous chapter are greatly determined by the properties of the 4*f* levels: their degeneracy, their energy, their symmetry, the anisotropy of their charge density distribution and their magnetic moment. In the following, the physics of the 4*f* electronic shell in a crystal environment is described following the discussion in Ref. [17]. In this section the Hamiltonian of a free ion is described and, successively, the crystal field Hamiltonian is introduced as a perturbation in section 2.1. This approach is justified by the fact that the 4*f* electrons in a material do not participate significantly in the chemical bondings and their interaction with the surrounding ions of a crystal can be modeled, to a good approximation, as an interaction with an effective electrostatic field, called the *crystal electric field* [18–22]. A small hybridization is often anyway present and for a correct description of the effects that arise due to this hybridization, a band model is required. However, for the experimental findings of this thesis a theoretical description within the *atomic multiplet theory* [23–25] is sufficient. The application of this model to the prediction of the x-ray spectroscopies spectra provides a concrete means to access the 4*f* (but also 5*f*) ground state [22, 26, 27]. The knowledge of the properties of the ground state level is the basis for the characterization of the *f* electron physics in Kondo lattice materials (see [26] and the references therein). In chapter 5.2 the limits of this approach and the physics that cannot be predicted within this model are shown.

2.1.1 Hamiltonian of the free ion

The calculation of the energy levels and wave functions of an atomic system is based on the solution of the Schrödinger equation

$$H\Psi = E\Psi. \tag{2.1}$$

Where H is the Hamiltonian, Ψ the eigenfunctions and E the eigenvalues of the system. Considering the nucleus of the atom as a point with a mass much higher than the electron mass and a charge Ze surrounded by N interacting electrons, of mass m and charge $-e$, the systems' Hamiltonian can be written as:

$$H = \sum_{i=1}^{N}\left(\frac{\mathbf{p}_i^2}{2m} - \frac{Ze^2}{\mathbf{r}_i} + \xi(\mathbf{r}_i)\boldsymbol{l}_i \cdot \boldsymbol{s}_i\right) + \sum_{i>j=1}^{N}\frac{e^2}{\mathbf{r}_{ij}}. \tag{2.2}$$

Where $\mathbf{p}$ is the momentum operator, $\boldsymbol{l}$ is the orbital angular momentum operator and $\boldsymbol{s}$ the spin angular momentum operator. The first summation considers only single electron terms and includes: the kinetic energy of each *i*-th electron, its potential energy produced by the nucleus and the spin-orbit interaction. The last term instead mixes the electrons' coordinates since it takes into account the interaction acting between each pair of electrons *ij* separated by a distance $\mathbf{r}_{ij} = \mathbf{r}_i - \mathbf{r}_j$. This prevents an analytic solution of the Schrödinger equation for atoms with more than 2 electrons. This Coulomb repulsion cannot be treated as a perturbation to the single electron Hamiltonian because its effect is of comparable magnitude than the interaction between the electron and the nucleus. A successful approach to tackle this problem is the *central field approximation* [28, 29]. In this approximation each electron is considered to be independently moving in an effective central field acting on single electron coordinates, which originates from the charge distribution of all the other electrons and behaves as an average potential that screens the nuclear charge. In this way the Hamiltonian in equation 2.2 can be rewritten as:

$$\begin{aligned} H &= H_0 + H_1, \\ H_0 &= \sum_{i=1}^{N}\left(\frac{\mathbf{p}_i^2}{2m} - \frac{Ze^2}{\mathbf{r}_i} + \langle\sum_{i>j=1}^{N}\frac{e^2}{\mathbf{r}_{ij}}\rangle\right) = \sum_{i=1}^{N}\left(\frac{\mathbf{p}_i^2}{2m} - U(\mathbf{r}_i)\right), \\ H_1 &= \sum_{i=1}^{N}\xi(\mathbf{r}_i)\boldsymbol{l}_i \cdot \boldsymbol{s}_i + \sum_{i>j=1}^{N}\frac{e^2}{\mathbf{r}_{ij}} - \langle\sum_{i>j=1}^{N}\frac{e^2}{\mathbf{r}_{ij}}\rangle = H_{SO} + H_{elec}, \end{aligned} \tag{2.3}$$

where $-U(\mathbf{r}_i)/e$ is the spherically symmetric effective potential, which depends only on the single electron coordinates, and $H_1 = H - H_0$ contains all the remaining interactions. The one particle Hamiltonian H_0 can now be used as the starting point for our calculation and successively H_1 can be added as a perturbation. The solution of the approximated multi-electron Schrödinger equation

$$H_0\Psi^0 = E^0\Psi^0 \tag{2.4}$$

can be expressed using single electron wave functions ψ_{k_i}, where *k* represents the set of quantum numbers (nlm_l). Moreover, since the Hamiltonian H_0 is spherically symmetric, the single electron wave functions can be separated into a radial and an angular

part:

$$\psi_{k_i} = R_{nl}(r)Y_{lm_l}(\theta,\phi), \tag{2.5}$$

where Y_{lm_l} are spherical harmonics and R_{nl} are the radial functions. The usual notation for the quantum numbers is used: *n* is the principal quantum number of the electron shell, *l* the orbital angular momentum quantum number and m_l the magnetic quantum number. The spin dependent wave function is introduced by multiplying ψ by one of the two spin wave functions corresponding to the two possible spin projections $m_s = \pm\frac{1}{2}$ along the z axis.

In the end, the full anti-symmetrized (in order to guarantee that the Pauli exclusion principle is not violated) many-electron wave function $\Psi^0(K_1, K_2, ..., K_N)$ solution of the Schrödinger equation 2.4 is given by the Slater determinant of the single-electron wave functions [28]:

$$\Psi^0(K_1,...,K_N) = \frac{1}{\sqrt{N!}}\begin{vmatrix} \psi_1(K_1) & \psi_1(K_2) & \cdots & \psi_1(K_N) \\ \psi_2(K_1) & \psi_2(K_2) & \cdots & \psi_2(K_N) \\ \vdots & \vdots & \ddots & \vdots \\ \psi_N(K_1) & \psi_N(K_2) & \cdots & \psi_N(K_N) \end{vmatrix}, \tag{2.6}$$

where $K = (nlm_lm_s)$. These wave functions are called *zero order wave functions* and make up the basis for calculating our first order corrections due to the perturbation potential H_1 which contains the spin-orbit and the remaining inter-electronic electrostatic interactions.

2.1.2 Spin-orbit and electrostatic electron-electron interaction

The calculations of the first order perturbation theory correction to the energy involve the evaluation of matrix elements of the kind:

$$\left\langle \Psi^0 \right| H_1 \left| \Psi^0 \right\rangle. \tag{2.7}$$

The details about the calculations are described by Condon *et al.* [29] for both the spin-orbit and the electrostatic perturbations. The separation of the wave function into an angular and a radial part is essential in the evaluation of the integrals. In particular, the radial part of the spin orbit interaction can be reduced to a parameter ζ_{nl} that stands for the integral

$$\zeta_{nl} = \int_0^\infty R_{nl}^2(r)\xi(r)r^2\,dr \tag{2.8}$$

so the spin orbit interaction operator acting on the angular part of the wave function of each electron can be written as:

$$\zeta_{nl}\,\boldsymbol{l}\cdot\boldsymbol{s}. \tag{2.9}$$

The electrostatic part involves integrals of the kind:

$$\left\langle R_{n_il_i}(r_i)Y_{l_im_{l_i}}(\theta_i,\phi_i)\right| \frac{1}{\mathbf{r}_{ij}} \left| R_{n_jl_j}(r_j)Y_{l_jm_{l_j}}(\theta_j,\phi_j)\right\rangle \tag{2.10}$$

where *i* and *j* are two electrons. Expanding the Hamiltonian $1/\mathbf{r}_{ij}$ in a series of Legendre polynomials and using the Wigner-Eckhart theorem [17], Eq. 2.10 can be written

as:

$$\sum_k f_k F^k + \sum_k g_k G^k. \tag{2.11}$$

F^k and G^k are the Slater integrals and involve integration over the radial part of the wave functions:

$$\begin{aligned} F^k(n_i l_i, n_j l_j) &= e^2 \int_0^\infty \int_0^\infty \frac{r_<^k}{r_>^{k+1}} R^2_{n_i l_i}(r_i) R^2_{n_j l_j}(r_j) r_i^2 r_j^2 \, dr_i dr_j \\ G^k(n_i l_i, n_j l_j) &= e^2 \int_0^\infty \int_0^\infty \frac{r_<^k}{r_>^{k+1}} R_{n_i l_i}(r_i) R_{n_i l_i}(r_j) R_{n_j l_j}(r_j) R_{n_j l_j}(r_i) r_i^2 r_j^2 \, dr_i dr_j, \end{aligned} \tag{2.12}$$

where *k* denotes the order of the multipole components in the interaction, $r_< = min(r_i, r_j)$ and $r_> = max(r_i, r_j)$. The integrals over the angular part of the wave functions instead gives rise to the f_k and g_k coefficients and they determine which multipole component of the Slater integrals contributes and their values can be found in tabulated form. See Ref.s [24, 30, 31] for more details. The values of the Slater integrals and of the spin-orbit parameters instead can be determined with the code by R.D.Cowan [30] based on the Hartree-Fock approximation.

2.1.3 Splitting of the atomic levels

Summing up: the Hamiltonian of a many electron free atom is $H = H_0 + H_{elec} + H_{SO}$. Where H_{elec} and H_{SO} are inserted as a perturbation to the one electron eigenfunctions of H_0. The leading term among the perturbations is H_{elec}. The effect of the electrostatic field is to differentiate the energy of some of the wave functions corresponding to different possible ways of arranging the electrons for a given electronic configuration. The obtained wave functions are characterized by the total angular momentum *L*, the total spin angular momentum *S*, given by the combination of the single electron angular momenta, and their components along the quantization axis M_L, M_S. These are the good quantum numbers to describe the system and usually the state is labeled using the *term symbols*: ^{2S+1}X, where X corresponds to a letter according to the value of L ($L = 0, 1, 2, 3, ...$ corresponds to $X = S, P, D, F, ...$). Wave functions characterized by the same L and S have the same energy so the degeneracy is $(2L + 1)(2S + 1)$.

In light rare-earth elements the next perturbation term to add is the spin-orbit Hamiltonian H_{SO}. It couples the spin and orbital angular momenta that are, in principle, no more conserved independently. The new good quantum number, which describes correctly the wave functions, is the total angular momentum $J = L + S$. So the H_{SO} term adds a correction to the previously calculated levels, splitting them into levels with the same S and L but different J. If this correction is small compared to the distance between levels with different term symbols, the levels can still be characterized in a good approximation by S and L and is possible to make use of the term symbol adding a subscript to differentiate the levels according to the value of J. This picture is called Russel-Saunders (or LS) coupling. The levels are still $(2J + 1)$-fold degenerate due to the M_J degeneracy. This group of levels indicated by the term symbol $^{2S+1}X_J$ is called a *multiplet*.

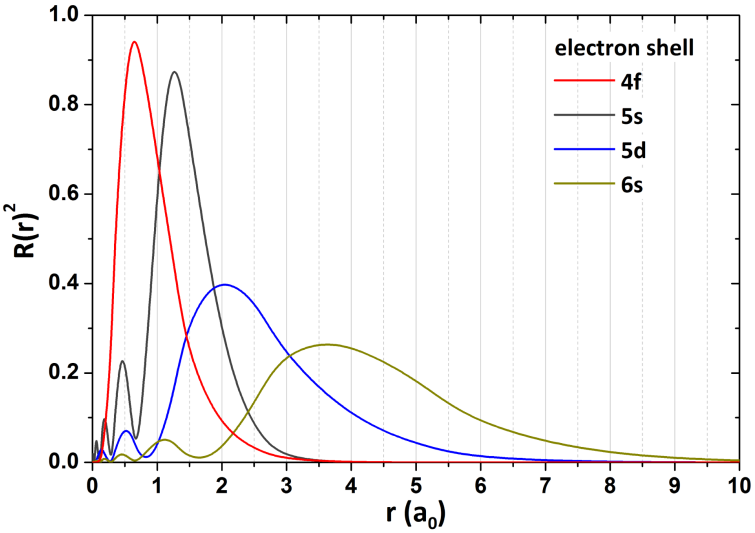

Figure 2.1: Square of the atomic radial wave functions for the 4*f*, 5*s*, 5*d* and 6*s* electronic shells, as calculated with the Hartree-Fock method for Ce^{3+}. On the x-axis the distance r from the nucleus is given in units of the Bohr radius a_0. Figure reproduced from Ref. [26].

2.2 Physics of the 4*f* shell in a crystal: crystal field theory

In this chapter it is considered how the atomic levels are modified when an atom is introduced into a crystal. The focus will be in particular on the behaviour of the levels of the 4*f* shell. In this case, the presence of the neighbouring atoms can be treated as a perturbation to the spin-orbit split system. This approach is justified considering the limited spatial extend of the atomic 4*f* radial wave functions. As an example the radial wave functions of Ce^{3+} are depicted in figure 2.1. Ce has an atomic configuration $[Xe]4f^15d^16s^2$. The $6s$ and $5d$ orbitals have the largest spatial extent and will overlap significantly with the wave functions of the neighbouring atoms, when inserted in a material, giving rise to molecular orbitals. Ce in materials is found very often as a Ce^{3+} ion, which means with a configuration $[Xe]4f^1$. The 4*f* electron does not participate in chemical bonding because its radial wave function is more localized and, moreover, it is partly screened by the full 5*s* shell. This justifies the use of perturbation theory to model the interactions of the $4f$-shell of a rare-earth atom with the crystal environment. This interaction can be modeled as an effective electrostatic field, which simulates the hybridization with the surrounding electrons, called *crystal electric field* (CEF) [18–22]. This interaction is described by the CEF Hamiltonian:

$$H_{CEF} = -e \cdot V_{CEF}(r, \theta, \phi), \tag{2.13}$$

where V_{CEF} is the CEF potential. This potential must reflect the symmetry of the environment in which the ion is inserted. The isolated atom has spherical symmetry and thus the levels are $(2J+1)$-fold degenerate. The effect of the CEF is to lower the symmetry and to lift the $(2J+1)$-fold degeneracy creating a splitting between the multiplet levels (see figure. 2.2).

To point out the role of the symmetry and to perform the calculations it is convenient

to expand the crystal field potential in terms of spherical harmonics:

$$V_{CEF}(r,\theta,\phi) = \sum_{k=0}^{\infty} \sum_{m=-k}^{k} \widetilde{A}_k^m \, r^k \, C_k^m(\theta,\phi) \tag{2.14}$$

where $C_k^m(\theta,\phi) = \sqrt{\frac{4\pi}{2k+1}} \cdot Y_k^m(\theta,\phi) = \sqrt{\frac{(k-m)!}{(k+m)!}} \cdot P_k(\cos\theta) \cdot e^{im\phi}$ are the renormalized spherical harmonics. The respective Hamiltonian can be applied as a first order perturbation to the atomic system. This involves the calculation of matrix elements in the basis of $\psi_k = R_{nl}(r)Y_{lm_l}(\theta,\phi)$:

$$\begin{aligned} &\langle \psi_{k_i} | H_{CEF} \left| \psi_{k_j} \right\rangle = \\ &\quad - e \sum_{k=0}^{\infty} \sum_{m=-k}^{k} A_k^m \left\langle Y_{l_i m_i}(\theta,\phi) \right| C_k^m(\theta,\phi) \left| Y_{l_j m_j}(\theta,\phi) \right\rangle . \end{aligned} \tag{2.15}$$

where $A_k^m = \widetilde{A}_k^m \left\langle R_{n_i l_i}(r) \right| r^k \left| R_{n_j l_j}(r) \right\rangle$. This radial integral could be solved within Hartree-Fock theory, but the radial wave functions are modified by the presence of the other ions in the solid and thus the calculation gives a non accurate value. In many cases, as in the studies presented here, the *crystal field parameters* A_k^m are unknown and have to be found via fitting of the experimental data with the calculated spectra [18]. The integration over the angular part in Eq. 2.15 determines those A_k^m that contribute to the sum. This can be solved analytically and can be expressed in terms of $3J$ symbols as:

$$\left\langle Y_{l_i}^{m_i} | C_k^m | Y_{l_j}^{m_j} \right\rangle = (-1)^{m_i} \sqrt{(2l_i+1)(2l_j+1)} \begin{pmatrix} l_i & k & l_j \\ 0 & 0 & 0 \end{pmatrix} \begin{pmatrix} l_i & k & l_j \\ -m_i & m & m_j \end{pmatrix} \tag{2.16}$$

where the $3J$ symbol is defined as:

$$\begin{pmatrix} j_1 & j_2 & j_3 \\ m_1 & m_2 & m_3 \end{pmatrix} = \frac{(-1)^{j_1 - j_2 - m_3}}{\sqrt{2j_3+1}} \left\langle j_1 m_1 j_2 m_2 | j_3 - m_3 \right\rangle . \tag{2.17}$$

The properties of the $3J$ symbol [18, 30] allows us to easily determine which crystal field parameters are required to describe the crystal field Hamiltonian. The triangular inequality imposes that only the terms with $k \leq l_i + l_j$ contribute. $k + l_i + l_j$ must be an even integer otherwise eq. 2.16 would be an integral over an odd function. An additional condition comes from the requirement of an hermitian Hamiltonian, which imposes $A_k^m = (-1)^m (A_k^{-m})^*$ [18]. This means that it is sufficient to determine the parameters for $m \geq 0$.

Additional restrictions can arise from the particular symmetry of the atomic site under investigation. The symmetry of the effective crystal field is defined as the point group of symmetry operators which leave the crystal field Hamiltonian invariant. For example, if the high symmetry axis has *q*-fold rotational symmetry, V_{CEF} has to fulfill the condition $V_{CEF}(r,\theta,\phi) = V_{CEF}(r,\theta,\phi + 2\pi/q)$. This translates into the condition $e^{im\phi} = e^{im(\phi+2\pi/q)}$, which is fulfilled if $m = N \cdot q$ with N an integer number. This condition directly implies that the crystal field Hamiltonian can only mix states with $\Delta J_z = q$ [32].

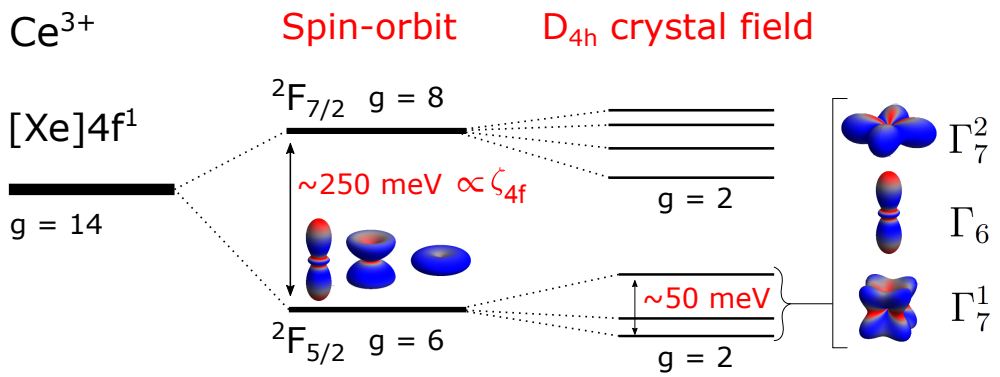

Figure 2.2: Schematic drawing of the energy levels splitting for Ce^{3+} inserted in a tetragonal crystal field. g is the degeneracy of the multiplets. Also plotted the electronic charge density of the orbitals of the ${}^2F_{5/2}$ multiplet in absence and in presence of the crystal field. The ${}^2F_{7/2}$ and ${}^2F_{5/2}$ multiplets are split, respectively, in 4 and 3 doubly degenerate Kramers doublets.

The parity is the behavior under the spatial inversion operation $i : \mathbf{r} \to -\mathbf{r}$. $f(\mathbf{r})$ has even parity if $f(\mathbf{r}) = f(-\mathbf{r})$ and odd parity if $f(\mathbf{r}) = -f(-\mathbf{r})$. The effective crystal field Hamiltonian is built from spherical harmonics, which are functions of well defined parity. In particular, the parity is connected to the order k by $parity = (-1)^k$ [33]. Also, the quantity r^k is such that $(-r)^k = (-1)^k r^k$. This means that applying the inversion operation to the crystal field potential one gets:

$$V_{CEF}(r,\theta,\phi) \xrightarrow{i} V_{CEF}(-r,\pi-\theta,\phi+\pi) = \sum_{k=0}^{\infty}\sum_{m=-k}^{k} \widetilde{A}_k^m\,(-1)^k r^k\,(-1)^k C_k^m(\theta,\phi). \tag{2.18}$$

This implies that V_{CEF} is always even under the inversion operation. This means that the point group symmetry of the effective crystal field always includes the inversion operation. The symmetry of the H_{CEF} may thus be higher than the geometrical/physical point symmetry of the crystal at the ion site [18].

2.3 Ce^{3+} ion in a tetragonal crystal field

The tools outlined in the previous chapters are applied here to the case of a Ce^{3+} ion in a tetragonal crystal field. As already pointed out, Ce is very often found in the oxidation state $3+$, which means it has the electronic configuration $4f^1$. Since there is only one electron in an unfilled shell while all the other shells are full, the inter electronic interaction can be fully modeled by the average potential screening. The f electron has $l = 3$ and $s = 1/2$, which are also the total atomic L and S. Thus the only possible term symbol is ${}^2F$. This configuration has a degeneracy $g = (2L+1)(2S+1) = 14$. Adding now as a perturbation the spin-orbit Hamiltonian, these states split according to their value of $J = |L \pm S| = 7/2, 5/2$. The energy of the two terms ${}^2F_{7/2}$ and ${}^2F_{5/2}$ is split by an amount proportional to ζ_{4f} (see fig. 2.2). The spin-orbit parameter is positive for shells that are less than half filled, which means that the states that decrease in energy will be the one with $\mathbf{L}\cdot\mathbf{S} < 0$. This means that the states with the lowest energies will be the states with the lowest $J = 5/2$. These energy levels are still $(2J+1) = 6$ fold degenerate. As already pointed out, this degeneracy is further split by the crystal field

Hamiltonian. In this work crystals with tetragonal structure will be encountered and a crystal field Hamiltonian of tetragonal D_{4h} symmetry is going to be used. The crystal field parameters A_k^m to be considered in the model are given by the previously outlined constraints. In this case $L = 3$, so $k \leq l_i + l_j = 3+3 = 6$, but also $k+6 = even$ implies k even. Thus for a $4f^1$ configuration in general the terms with $k = 0, 2, 4, 6$ contribute. The spherical harmonic of order $k = 0$ is spherically symmetric and its effect is usually neglected or can be included in the spherical symmetric effective potential of eq. 2.3. The D_{4h} symmetry shows a fourfold rotational axis which imposes $m = 0, 4$. This implies that the states resulting from the crystal field perturbation contains a mixture of states with $\Delta J_z = 4$. The lowest ${}^2F_{5/2}$ multiplet is formed by states that can be labeled by their magnetic quantum number $M_J = \pm 5/2, \pm 3/2, \pm 1/2$, or equivalently by their expectation value of the J_z operator $J_z = \pm 5/2, \pm 3/2, \pm 1/2$ (in units of $\hbar$). So the previous condition implies that the wave functions after the crystal field perturbation will be given by mixtures of: $J_z = \pm 5/2$ and $J_z = \mp 3/2$, while $J_z = \pm 1/2$ does not mix with any state belonging to the ${}^2F_{5/2}$ multiplet but can mix with the $J_z = \mp 7/2$ states of the ${}^2F_{7/2}$ multiplet.

For the sake of simplicity, this possible inter-multiplet mixing will be neglected, which means supposing that the spin-orbit splitting is higher than the crystal field splitting (so-called Stevens approximation [34]). This limits the analysis to the ${}^2F_{5/2}$ multiplet. This is often a good approximation for Ce. An additional condition rises in this case and limits k to $k \leq 2J = 5$ excluding the $k = 6$ term [35]. This means that the effective crystal field potential will be:

$$V_{CEF}(r, \theta, \phi) = \widetilde{A}_2^0 \, r^2 \, C_2^0 + \sum_{m=-4,0,4} \widetilde{A}_4^m \, r^4 \, C_4^m. \tag{2.19}$$

The ${}^2F_{5/2}$ multiplet has a half-integral total angular momentum. This must be reflected in the symmetry behaviour of the wave function under rotations. These considerations lead to the introduction of the so called Bethe double groups, which correctly describe the symmetry of half-integral total angular momentum wave functions. It is possible to find, based uniquely on symmetry considerations, how the levels of the ${}^2F_{5/2}$ multiplet split when its symmetry is reduced from spherical to tetragonal. In particular the multiplet splits in three doubly degenerate levels: one of symmetry Γ_6, and two of symmetry Γ_7. Where the Bethe notation has been used to identify the irreducible representations of the D_{4h} double group. The behaviour of these states under the symmetry operations of the tetragonal point group D_{4h} can be found in Ref. [36]. The fact that the states are doubly degenerate is a general result called Kramers degeneracy theorem [37]. It states that every eigenstate of a time-reversal symmetric system with half-integral total spin is at least doubly degenerate [38]. The effective crystal electric field always contains the time reversal symmetry.

Applying the CEF Hamiltonian as a perturbation to the atomic system, one obtains the expressions of the wave functions and of the energy levels as a function of the values of the crystal field parameters A_k^m of eq. 2.15. The calculations can be performed using the SolidStatePackage for Mathematica by Maurits Haverkort [39]. The obtained wave functions can be written as a combination of the pure J_z wave functions $|J, J_z\rangle$, or more

simply $|J_z\rangle$ since all belong to the same $J = 5/2$ multiplet:

$$\begin{aligned}\Gamma_7^1 &= \frac{1}{\sqrt{a^2+b^2}}(a\,|\pm 5/2\rangle + b\,|\mp 3/2\rangle)\\ \Gamma_7^2 &= \frac{1}{\sqrt{a^2+b^2}}(b\,|\pm 5/2\rangle - a\,|\mp 3/2\rangle)\\ \Gamma_6 &= |\pm 1/2\rangle\,,\end{aligned} \tag{2.20}$$

A *mixing parameter* α is defined and expressed in terms of the crystal field parameters as:

$$\alpha = \frac{a}{\sqrt{a^2+b^2}} = \frac{-5\sqrt{14}\mathrm{A}_4^4}{\sqrt{350\mathrm{A}_4^{4\,2} + \left(18\mathrm{A}_2^0 - 10\mathrm{A}_4^0 - \sqrt{4(9\mathrm{A}_2^0 - 5\mathrm{A}_4^0)^2 + 350\mathrm{A}_4^{4\,2}}\right)^2}}. \tag{2.21}$$

The respective energies of the crystal field split states are:

$$\begin{aligned}\mathrm{E}_{\Gamma_7^1} &= \frac{1}{105}\left[-12\mathrm{A}_2^0 - 5\mathrm{A}_4^0 - \sqrt{4(9\mathrm{A}_2^0 - 5\mathrm{A}_4^0)^2 + 350\mathrm{A}_4^{4\,2}}\right],\\ \mathrm{E}_{\Gamma_7^2} &= \frac{1}{105}\left[-12\mathrm{A}_2^0 - 5\mathrm{A}_4^0 + \sqrt{4(9\mathrm{A}_2^0 - 5\mathrm{A}_4^0)^2 + 350\mathrm{A}_4^{4\,2}}\right],\\ \mathrm{E}_{\Gamma_6} &= \frac{8}{35}\mathrm{A}_2^0 + \frac{2}{21}\mathrm{A}_4^0.\end{aligned} \tag{2.22}$$

The inequality $\mathrm{E}_{\Gamma_7^1} < \mathrm{E}_{\Gamma_7^2}$ always holds (this is the reason for the superscripts 1 and 2), however E_{Γ_6} can both be lower or higher than $\mathrm{E}_{\Gamma_7^1}$. The *sign* of the parameter A_4^4 does not influence the splitting of the energy levels. Moreover, the *sign* does not influence the magnitude of the mixing parameter α, of which it determines uniquely the sign. The sign of the mixing parameter is related to the orientation of the orbital with respect to the crystallographic axes.

2.4 Experimental techniques to determine the crystal field

The most direct way to determine the CEF scheme consists in measuring the absorption of optical radiation [40], but this is not applicable in non-transparent metallic materials such as the intermetallic compounds containing rare earths considered in this thesis. Indirect measurements can be effectively applied, for example exploiting the measurement of physical quantities connected to the magnetic properties of the material. In fact, in f materials the magnetic properties are mainly determined by the rare earth ion. The measurement of the *magnetic susceptibility* (χ) [41] can therefore give a measure of the atomic magnetic moment μ that can be related to the J_z mixing. The measurement of the dependence of the susceptibility on the direction of the applied magnetic field gives insight also about the anisotropy of the state, related to the J_z of the state. Another indirect way is the measurement of the *specific heat*. The occupancy of the excited crystal field states increases as the temperature increases and this leads to an increase in the specific heat, which can be related to the splitting between the levels [21]. Inelastic Neutron Scattering (INS) [21] has become the dominant method because it gives directly the splitting between the $4f$ levels as peaks in the energy loss

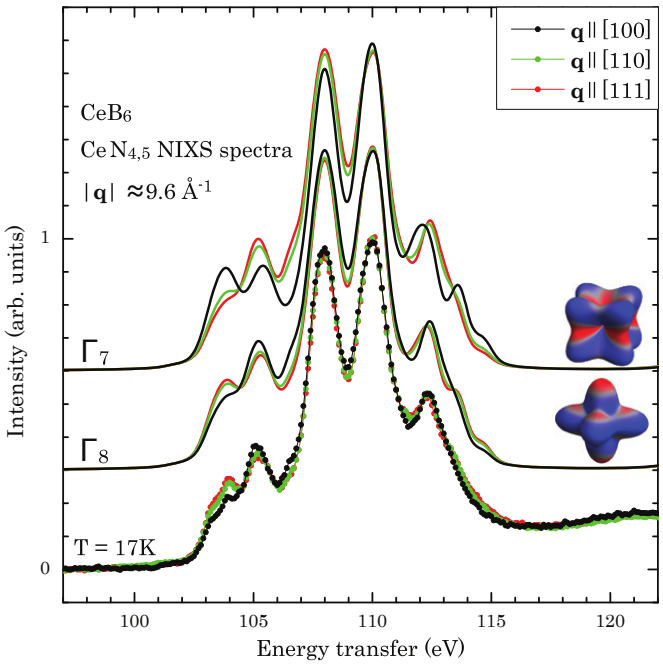

Figure 2.3: Calculated and experimental NIXS spectra of the Ce^{3+} $N_{4,5}$ edge in CeB_6 for the three transferred momentum directions $\mathbf{q} \parallel [100], [110]$ and $[111]$. Reproduced from [47]. Each wave function Γ_7 and Γ_8 has a clearly distinguishable dependence on the direction of $\mathbf{q}$. This allows to easily identify the quartet Γ_8 as the ground state level.

spectrum at the energy corresponding to the CEF-splitting. However, in the following the focus lies on more recent techniques that overcome the limitations of the INS as the need for centimeter-sized crystals, the low counting rate and the superposition of the phonon scattering. X-ray absorption spectroscopy, described in chapter 3.2.2, was first proposed as a complementary tool to determine the crystal field ground state in rare earth intermetallics by Hansmann *et. al* [42–44]. The crystal field orbitals are anisotropic, this gives rise to a dependence of the absorption probability as a function of the direction of the linear polarization [45]. This is clearly shown in the simulations in chapter 6.3. This X-ray Linear Dichroism (XLD) strongly depends on the ground state wave function's J_z.

Later, it was proposed by Gordon *et. al* [46] that the natural linear dichroism could be probed also using orientation-dependent x-ray Raman scattering (XRS), described in chapter 3.3. This kind of non-resonant inelastic x-ray scattering (NIXS) technique has the advantage, with respect to XAS, of being sensitive to lower than 2-fold symmetries, since it is not limited by dipolar transitions. This technique was thus applied to determine the crystal field ground state in cubic compounds such as CeB_6 [47]. In figure 2.3 the NIXS experimental spectra of CeB_6 are shown and compared with the simulations. The dependence on the direction of the exchanged momentum is different for the two crystal field wave functions. The comparison of the simulated spectra with the experimental data allows one to determine the ground state wave function.

Both in XAS and XRS the experimental resolution can be orders of magnitude lower than the crystal field splittings they are required to resolve.

Recently, resonant inelastic x-ray scattering (RIXS) has become available as a tool to characterize the crystal field thanks to the very high resolution ($\approx 20\,\mathrm{meV}$) that has been achieved in the soft x-ray range that allows to resolve the $4f \rightarrow 4f$ transitions [27].

CHAPTER 3

X-ray absorption and x-ray Raman core level spectroscopies

The properties of solids are strongly determined by the outer electronic states of the atoms, called the valence electron states (VES). These states are for example the filled conduction bands in metals, the completely filled and completely empty bands in insulators, but also the 4f states of rare earth (RE) elements with their peculiar behaviour. The VES are therefore the main object of study of solid state physics because the knowledge of their characteristics can provide an explanation for the observed properties of the solids. Instead, the inner electrons, called core electrons are almost unchanged by the formation of the solid. Core level spectroscopies are powerful tools to study the VES [24]. A core electron is excited creating a vacancy in an inner state, which can be described as a positively charged particle called core hole. This state has a well known character because it is well modeled by atomic physics theories. This core hole state will be the probe that allows us to get information on the VES. A core electron can be excited in several ways, for example through electron, proton or ion scattering, but in this thesis the focus is on exciting the core electron via x-ray absorption and inelastic x-ray scattering. In an x-ray absorption process an electron can be excited into an empty state below the ionization threshold, thus remaining "trapped" and forming an excitonic state, or the electron can absorb enough energy to leave the atom with a certain kinetic energy. These processes form the basis of x-ray absorption spectroscopy (XAS) [22, 24, 26] and x-ray photoemission spectroscopy (XPS). An x-ray photon can also scatter inelastically off of a core electron losing part of its energy in the process and this energy can excite the core electron. This process is known as x-ray Raman scattering (XRS), in analogy to the optical and infrared Raman scattering [48, 49]. The spectroscopy technique that exploits the XRS process will be presented in detail in chapter 3.3. The choice of the core electron that is being excited is important and a notation [50] is used

Orbital	1s	2s	$2p_{1/2}$	$2p_{3/2}$	...	$3p_{3/2}$	$3d_{3/2}$	$3d_{5/2}$	...	$4d_{3/2}$, $4d_{5/2}$
Energy [eV]	40443	6549	6164	5723	...	1187	902.4	883.8	...	109
Label	K	L_1	L_2	L_3	...	M_3	M_4	M_5	...	$N_{4,5}$

Table 3.1: Cerium binding energies. Data taken from X-ray data booklet, 2009 [51].

to label the exploited core-hole state. To indicate the principal quantum number *n*= 1, 2, 3, 4, ... a letter is used instead of the number: respectively K, L, M, N, ... The different angular momentum states s, p, d, f are numbered from the high binding energy to the low binding energy as you can see for example in table 3.1 for the case of Ce.

3.1 Hamiltonian for the photon-electron interaction

The discussion by Schülke in [52] will be followed, which consists of writing the interaction Hamiltonian, applying perturbation theory in order to obtain Fermi's golden rule and obtain the double differential scattering cross section (DDCS). The Hamiltonian for electrons in a quantized electromagnetic field is given by terms describing the radiation field, the kinetic and potential energy of the electrons and the interaction between the photon field and the electrons:

$$\begin{aligned} H = & \sum_j \frac{1}{2m}[\mathbf{p}_j - (e/c)\mathbf{A}(\mathbf{k},\mathbf{r}_j)]^2 + \sum_{jj'} V(r_{jj'}) \\ & - \frac{e\hbar}{2mc}\sum_j \sigma_j \cdot \nabla \times \mathbf{A}(\mathbf{k},\mathbf{r}_j) \\ & - \frac{e\hbar}{4m^2c^2}\sum_j \sigma_j \cdot \mathbf{E}(\mathbf{k},\mathbf{r}_j) \times [\mathbf{p}_j - (e/c)\mathbf{A}(\mathbf{k},\mathbf{r}_j)] + H_{field}]. \end{aligned} \tag{3.1}$$

Here the summation j, j' is over all the electrons of the scattering system; m is the mass of the electron; c is the speed of light; **p** is the momentum operator; $V(r_{jj'})$ is the electron electron interaction; **A**(**k**,**r**) is the vector potential of the electromagnetic wave with wave vector **k** at the position **r** of the electron, expressed in second quantization as:

$$\mathbf{A}(\mathbf{k},\mathbf{r}) = A_0 \mathbf{e}_{\mathbf{k}\lambda}(b_{\mathbf{k}\lambda}e^{i\mathbf{k}\cdot\mathbf{r}} + b^\dagger_{\mathbf{k}\lambda}e^{-i\mathbf{k}\cdot\mathbf{r}}), \tag{3.2}$$

where $\mathbf{e}_{\mathbf{k}\lambda}$ is the polarization vector, $b_{\mathbf{k}\lambda}$ is the photon annihilation operator and its hermitian $b^\dagger$ is the photon creation operator. σ is the spin vector operator whose components are the Pauli matrices; **E** is the operator of the electric field at the electron position **r**, which can be expressed in terms of the vector potential operator **A** via the gauge equation:

$$\mathbf{E} = -\nabla\phi - \frac{1}{c}\dot{\mathbf{A}} \tag{3.3}$$

where $\phi(\mathbf{r})$ is the Coulomb potential. The first term in Eq. (3.1) represents the kinetic energy of the electron system in the presence of the radiation field. The second term is the potential energy of the interacting electrons, discussed in chapter 2.1. The third term is the potential energy of the magnetic moment $(e\hbar/2mc^2)\sigma$ in the magnetic field $\nabla \times \mathbf{A} = \mathbf{B}$ of the radiation. The fourth term is the energy of the magnetic moment $(e\hbar/2mc^2)\sigma$ in a magnetic field $(1/c)(\mathbf{v} \times \mathbf{E})$. This is the magnetic field one finds in

the rest frame of the electron, when the electron is moving with a velocity **v**, expressed in terms of canonical momentum according to $\mathbf{v} = (1/m)[\mathbf{p} - (e/c)\mathbf{A}]$. Part of this term is responsible for the intrinsic spin orbit effect (see below). The last term is the energy of the photon field.

A perturbation treatment will be used to calculate the scattering cross-section, i.e. use the interaction terms as a small perturbation of the system. It is needed to separate the terms describing the atomic system from the terms describing the radiation field containing the vector potential **A**. The square in the first term of Eq. (3.1) has to be evaluated, the expression of **E** inserted from Eq. (3.3), and the spin-orbit term has to be evaluated. The Hamiltonian 3.1 can be separated into three terms $H = H_{atomic} + H_{int} + H_{field}$: the interaction Hamiltonian collects all the terms which contain the vector potential **A**

$$\begin{aligned} H_{int} = \sum_j \Big[& -\frac{e}{mc}\mathbf{A}(\mathbf{k},\mathbf{r}_j)\cdot\mathbf{p}_j \\ & + \frac{e^2}{2mc^2}\mathbf{A}^2(\mathbf{k},\mathbf{r}_j) \\ & - \frac{e\hbar}{2mc}\sigma_j\cdot[\nabla\times\mathbf{A}(\mathbf{k},\mathbf{r}_j)] \\ & - \frac{e^2\hbar}{4m^2c^4}\sigma_j\cdot[\dot{\mathbf{A}}(\mathbf{k},\mathbf{r}_j)\times\mathbf{A}(\mathbf{k},\mathbf{r}_j)] \ + ... \Big], \end{aligned} \tag{3.4}$$

where the additional spin orbit terms, that are negligible in our non-relativistic approximation, are omitted; the remaining part that describes the electron system

$$H_{atomic} = \sum_j \frac{1}{2m}\mathbf{p}_j^2 + \sum_{jj'} V(r_{jj'}) + \frac{e\hbar}{4m^2c^2}\sum_j \sigma_j\cdot(\nabla\phi\times\mathbf{p}_j); \tag{3.5}$$

and the field Hamiltonian H_{field}, which from now on will be neglected for simplicity even though in a detailed theoretical treatment it should be taken into account. The first two terms of Eq. 3.4 arise from the kinetic energy operator, the third from the Dirac equation and the fourth from the spin orbit. The additional terms are neglected as they would lead to higher order corrections or negligible contributions in the cases considered here. In this non-relativistic calculation approximation, the terms are restricted to second order in (v/c). The crystal field Hamiltonian could also be introduced as a perturbation to the atomic one as described in chapter 2.

This Hamiltonian is general and from this the expression of the scattering cross section of several different experimental techniques can be obtained applying the interaction Hamiltonian in Eq. 3.4 as a perturbation to the eigenstates of the Hamiltonian 3.5. The first term $\mathbf{A}\cdot\mathbf{p}$ gives rise to resonant electric multipole scattering. In first order perturbation it describes x-ray absorption (XAS, chapter 3.2), while with a second order perturbation the resonant inelastic x-ray scattering (RIXS [53]) can be described. The second term $\mathbf{A}^2$ gives rise, in first order perturbation, to non-resonant inelastic x-ray scattering (NIXS, see chapter 3.3). While the third and fourth terms containing the spin matrix σ give rise to magnetic scattering, whose cross section can be found to be much smaller than the other by a factor $\hbar\omega/mc^2 \approx 10\,\mathrm{keV}/510\,\mathrm{keV}$ smaller than the spin-independent one. For the purpose of this discussion, these terms are neglected even though they are at the basis of interesting spectroscopic techniques [54].

3.2 X-ray Absorption Spectroscopy (XAS)

3.2.1 Absorption edges

In x-ray absorption spectroscopy (XAS) [22, 24, 26] a deeply-bound core electron is excited into an unoccupied valence state by the absorption of a photon. If the energy of the incident photons corresponds to the binding energy of a core level, a sharp rise of the absorption probability will occur and this rise is called an absorption edge. This corresponds to the transition from the ground state to the lowest empty state that can be reached. Every element has its own value of the energies for the edge thresholds, which makes this technique, together with the other core level spectroscopies, an element-selective technique. When the threshold is overcome the electron can be excited into an excitonic state, which means that the core hole interacts strongly with the excited electron forming a bound state. The electron can also be excited into a non bound-state. This transition gives rise to the continuum edge jump and to describe this transitions a many body description of the conduction band states is required. The excitons instead are highly localized and have large binding energies so that an atomic multiplet description can provide an adequate prediction of the spectral features. The lifetime of the excited state is of the order of 10^{-15}s as the core-hole is filled by another electron. Via Heisenberg's uncertainty principle this results in an energy broadening of the order of some $100\,\mathrm{meV}$ which varies from edge to edge. There are different processes through which the core-hole can decay. For example through x-ray fluorescence in which an electron in an upper level can decay into the core-hole emitting a radiation corresponding to the energy difference between the initial and final level. In another case, this energy difference can be transferred directly to another electron giving rise to the so called Auger effect: an electron decays into the hole transferring the energy difference to another electron, which can acquire enough kinetic energy to overcome the surface potential of the material and ionize it.

3.2.2 Theoretical description

To describe an x-ray absorption process, which involves one photon, a first order perturbation of the $\mathbf{p}\cdot\mathbf{A}$ term in the interaction Hamiltonian of eq. 3.4 is applied to the atomic system described by the Hamiltonian of eq. 3.5. The transition probability is thus given by Fermi's Golden Rule, which states that the probability of having a transition from an initial state i to a final state f by absorbing the incident photon energy $\hbar\omega$ is given by:

$$w = \frac{2\pi}{\hbar}|\langle f|\, H_{XAS}\,|i\rangle|^2\delta(E_i - E_f + \hbar\omega), \tag{3.6}$$

where

$$H_{XAS} = \frac{e}{mc}\mathbf{A}(\mathbf{k},\mathbf{r}_j)\cdot\mathbf{p}_j. \tag{3.7}$$

Expressing the vector potential $\mathbf{A}$ in second quantization and summing over the possible modes $\mathbf{k}$ it is obtained:

$$\mathbf{A}(\mathbf{r}) = \sum_{\mathbf{k},\lambda} A_0\mathbf{e}_{\mathbf{k}\lambda}(b_{\mathbf{k}\lambda}e^{i\mathbf{k}\cdot\mathbf{r}} + b^\dagger_{\mathbf{k}\lambda}e^{-i\mathbf{k}\cdot\mathbf{r}}), \tag{3.8}$$

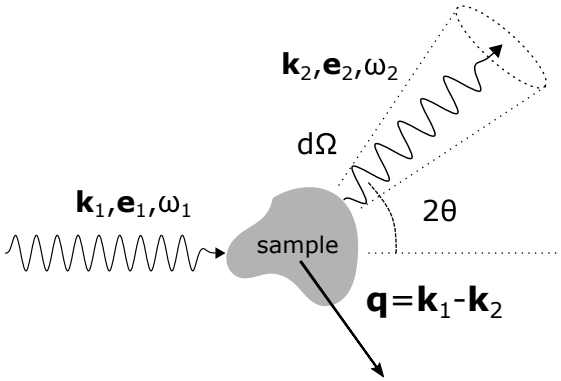

Figure 3.1: Schematic drawing of an IXS experiment. An incoming x-ray with wave vector $\mathbf{k}_1$, polarization $\mathbf{e}_1$ and energy $\hbar\omega_1$ is scattered off the sample at a scattering angle 2θ. After the scattering it has a wave vector $\mathbf{k}_2$, a polarization $\mathbf{e}_2$ and an energy $\hbar\omega_2$.

where $b_{\mathbf{k}\lambda}$ is the annihilation operator that is needed to describe the absorption of a photon, and $\mathbf{e}_{\mathbf{k}\lambda}$ is the vector describing the polarization. Expanding using a Taylor expansion $e^{i\mathbf{k}\cdot\mathbf{r}} = 1 + i\mathbf{k}\mathbf{r} + ...$, and considering the case in which $\mathbf{k}\mathbf{r} \ll 1$ (dipole approximation: valid if $\hbar\omega \ll 10\,\mathrm{keV}$ as in the cases discussed in the thesis) the XAS Hamiltonian is obtained as:

$$H_{XAS} = \sum_{\mathbf{k},\lambda} b_{\mathbf{k}\lambda} \frac{e}{mc} A_0 (\mathbf{e}_{\mathbf{k}\lambda} \cdot \mathbf{p}). \tag{3.9}$$

Therefore, the spectral intensity I that one expects from a XAS experiment for a dipole excitation will be proportional to the matrix element:

$$I \propto |\langle f| \mathbf{e}_{\mathbf{k}\lambda} \cdot \mathbf{p} |i\rangle|^2 \tag{3.10}$$

This is usually rewritten in terms of the position vector $\mathbf{r}$ using the equation of motion $\mathbf{p} \equiv -i\hbar\nabla = [\mathbf{r}, H]m/i\hbar$ as:

$$\langle f| \mathbf{e}_{\mathbf{k}\lambda} \cdot \mathbf{p} |i\rangle = im(E_f - E_i) \langle f| \mathbf{e}_{\mathbf{k}\lambda} \cdot \mathbf{r} |i\rangle . \tag{3.11}$$

The bracket corresponds to an integral over the whole space and, exploiting parity considerations, it is possible to understand which transitions are allowed. Since the dipole operator is odd, transitions are allowed only between states with different parity. Considering also the conservation of orbital and spin angular momentum the following selection rules are obtained:

$$\Delta L = \pm 1, 0; \quad \Delta J = \pm 1, 0; \quad \Delta S = 0. \tag{3.12}$$

3.3 X-ray Raman Spectroscopy (XRS)

3.3.1 Double differential scattering cross section

In this thesis, the focus lies on the Non-resonant Inelastic X-ray Scattering (NIXS) technique, which, when connected with core-electron excitations, is called non-resonant X-ray Raman Scattering (XRS). Like all the other Inelastic X-ray Scattering (IXS) processes it is a two photons process the basic kinematics of which can be sketched as

in Fig. 3.1: a photon of wave vector $\mathbf{k}_1$, polarization $\mathbf{e}_1$ and energy $\hbar\omega_1$ impinges on the sample characterized by an initial state $|i\rangle$ with an energy E_i and is scattered by an angle 2θ leaving the sample with a wave vector $\mathbf{k}_2$, a polarization $\mathbf{e}_2$ and an energy $\hbar\omega_2$. After the scattering the sample will be in a state $|f\rangle$ with energy E_f due to the transfer of energy $\hbar\omega$ and momentum $\hbar\mathbf{q}$. Conservation of energy and momentum requires that

$$\begin{aligned} \hbar\omega &= E_f - E_i = \hbar(\omega_1 - \omega_2), \\ \hbar\mathbf{q} &= \hbar(\mathbf{k}_1 - \mathbf{k}_2). \end{aligned} \tag{3.13}$$

From the conservation of momentum it is found that the transferred momentum is connected to the scattering angle by

$$|\mathbf{q}| = |\mathbf{k}_1 - \mathbf{k}_2| = (\omega_1^2 + \omega_2^2 - 2\omega_1\omega_2 \cos 2\theta)^{1/2}/c. \tag{3.14}$$

If the exchanged energy is much smaller than the incident energy $\omega \ll \omega_1$ and $\omega_2 \approx \omega_1$ equation 3.14 can be approximated as:

$$q \approx \frac{\omega_1}{c}(2 - 2\cos 2\theta))^{1/2} = k_1 2\sin\theta = 2\frac{\hbar\omega}{\hbar c}\sin\theta. \tag{3.15}$$

An IXS experiment consists in producing a well collimated and monochromatic x-ray beam and detecting the radiation scattered from the sample by an angle 2θ (thus fixing $\mathbf{q}$) into a solid angle element $d\Omega$ with an energy in the range dE_2, what is measured is the so called double differential scattering cross-section (DDSCS) as a function of $\mathbf{q}$ and ω defined as:

$$\frac{d\sigma}{d\Omega d\omega_2} \equiv \frac{\begin{array}{c}\text{current of photons scattered into } [\Omega_2,\, \mathrm{d}\Omega_2] \\ \text{with an energy in the range } [\hbar\omega_2,\, \mathrm{d}\hbar\omega_2]\end{array}}{\text{current density of the incident photons} \times\, \mathrm{d}\Omega_2 \times\, \mathrm{d}\hbar\omega_2}. \tag{3.16}$$

IXS is a two photon process. The vector potential is linear in the creation and annihilation operators as shown in equation 3.2. To describe an IXS process a first order perturbation for the term $\mathbf{A}^2$ in the interaction Hamiltonian of Eq. 3.4 is required. Also the term $\mathbf{A}\cdot\mathbf{p}$ describes a IXS process in second order perturbation. This contribution dominates only at resonance and gives rise to RIXS, while if the energy of the radiation is far from an absorption edge this scattering can be neglected. In the case of non-resonant inelastic x-ray scattering (NIXS) the transition probability per unit time is given by Fermi's Golden Rule

$$w = \frac{2\pi}{\hbar}|\langle f|\, H_{NIXS}\, |i\rangle|^2 \delta(E_i - E_f + \hbar\omega), \tag{3.17}$$

where

$$H_{NIXS} = \frac{e^2}{2mc^2}\mathbf{A}^2(\mathbf{k}, \mathbf{r}_j). \tag{3.18}$$

From these equations the double differential scattering cross section is obtained (Schülke [52]). The transition from the initial electrons system state $|i\rangle$ to the final state $|f\rangle$ is given by:

$$\begin{aligned} \left(\frac{d\sigma}{d\Omega d\omega_2}\right)_{|i\rangle\to|f\rangle} = \left(\frac{e^2}{mc^2}\right)^2 \left(\frac{\omega_2}{\omega_1}\right) |\langle f| \sum_j \exp(i\mathbf{q}\cdot\mathbf{r}_j)\, |i\rangle\, (\mathbf{e}_1 \cdot \mathbf{e}_2^*)| \\ \times\, \delta(E_i - Ef + \hbar\omega) \end{aligned} \tag{3.19}$$

Summing over all the possible final states and weighing the initial states $|i\rangle$ by their probability of occupation

$$p_i = Z^{-1} \exp(-E_i/k_B T) \tag{3.20}$$

where Z is the partition function, k_B the Boltzmann constant and T the temperature, the DDSCS can be written as a product of two terms:

$$\frac{d\sigma}{d\Omega d\omega_2} = \left(\frac{d\sigma}{d\Omega}\right)_{\mathrm{Th}} S(\mathbf{q}, \omega). \tag{3.21}$$

The first term $(d\sigma/d\Omega)_{\mathrm{Th}}$ is the Thomson scattering cross section and introducing the classical electron radius $r_0 \equiv e^2/mc^2$ it can be written as:

$$\left(\frac{d\sigma}{d\Omega}\right)_{\mathrm{Th}} \equiv r_0^2 \left(\frac{\omega_2}{\omega_1}\right) |\mathbf{e}_1 \cdot \mathbf{e}_2^*|^2. \tag{3.22}$$

It describes the strength of the photon-electron coupling. The second term in Eq. 3.21 is the dynamic structure factor and contains all the information about the many-body system that can be obtained by non-resonant IXS:

$$S(\mathbf{q}, \omega) = \sum_{i,f} \sum_j p_i |\langle f| \exp(i\mathbf{q} \cdot \mathbf{r}_j) |i\rangle|^2 \delta(E_i - E_f + \hbar\omega) \tag{3.23}$$

Some considerations about the transition operator $\exp(i\mathbf{q} \cdot \mathbf{r})$ allow to understand the strength of the NIXS technique. For small q the transition operator can be expanded in a Taylor series:

$$\exp(i\mathbf{q} \cdot \mathbf{r}) \approx 1 + i\mathbf{q} \cdot \mathbf{r} - \frac{(\mathbf{q} \cdot \mathbf{r})^2}{2} + ... \tag{3.24}$$

At low q the NIXS cross section is dominated by dipole transitions and it becomes equivalent to the XAS Hamiltonian 3.9 (see [55] for details). Instead, as q increases higher order terms become dominant and the technique becomes sensitive to dipole forbidden transitions (quadrupole, sextupole, octupole, ...). For large q and to better understand the role of the symmetry of the operator in these transitions the operator is conveniently expanded in a sum over spherical harmonics. In order to follow the formalism that is used in the calculations, the transition operator is expressed in terms of spherical harmonics as done by Haverkort (2007) in Ref. [56]:

$$\exp(i\mathbf{q} \cdot \mathbf{r}) = \sum_{k=0}^{\infty} \sum_{m=-k}^{k} i^k (2k+1) j_k(qr) C^*_{k,m}(\theta_q, \phi_q) \cdot C_{k,m}(\theta_r, \phi_r), \tag{3.25}$$

where $j_k(qr)$ is the *k*th-order spherical Bessel function, which contains the dependence on the modulus of the exchanged momentum and $C_{k,m} = \sqrt{4\pi/(2k+1)} Y_{k,m}$ are the renormalized spherical harmonics, which contain the dependence on the direction of the momentum. In the calculations the many body wave functions are built from one particle orbital basis functions, which are written as a product of a radial wave function times a spherical harmonic. In this way is possible to separate the matrix element in Eq. (3.23) calculated for a one particle orbital into a radial and an angular part:

$$\left\langle R_f(r) \cdot Y_{l_f,m_f}(\theta_r, \phi_r) \right| e^{i\mathbf{q}\cdot\mathbf{r}} \left| R_i(r) \cdot Y_{l_i,m_i}(\theta_r, \phi_r) \right\rangle = \sum_{k,m} A_{k,m} I_{k,m} \tag{3.26}$$

where

$$A_{k,m} = i^k (2k+1) C^*_{k,m}(\theta_q, \phi_q) \langle R_f | j_k(qr) | R_i \rangle , \tag{3.27}$$

and

$$I_{k,m} = \left\langle Y_{l_f,m_f} \right| C_{k,m}(\theta_r, \phi_r) \left| Y_{l_i,m_i} \right\rangle . \tag{3.28}$$

Eq. 3.28 is the angular part of the 2^k-pole spectrum and the integral between the three spherical harmonics can be rewritten in terms of the Wigner 3j-symbols as:

$$I_{k,m} \propto \begin{pmatrix} l_f & k & l_i \\ 0 & 0 & 0 \end{pmatrix} \begin{pmatrix} l_f & k & l_i \\ -m_f & m & m_i \end{pmatrix} . \tag{3.29}$$

From this expression the transition selection rules can be obtained. $I_{k,m}$ does not vanish only if the triangular inequality $|l_f - l_i| \leq k \leq l_f + l_i$ holds and if $l_f + k + l_i$ is equal to an even integer since the expectation value over an odd function is zero. This means that for a transition $d \rightarrow f$, for example, for which the initial angular momentum is $l_i = 2$ and the final is $l_f = 3$, $I_{k,m}$ is non zero for $k = 1$ (dipole), $k = 3$ (octupole) and $k = 5$ (triakontadipole).

The dipole transition has the same transition rules of the dipolar XAS as in the equations 3.12. In general the inequalities $|J_i - k| \leq J_f \leq J_i + k$ and $|L_i - k| \leq L_f \leq L_i + k$ are valid. If the LS coupling holds $\Delta S = 0$, which is the case of light rare earths elements, otherwise in intermediate coupling it is possible to have $\Delta S = \pm 1, 0$. XRS then allows access to transitions with $\Delta L = \Delta J = \pm 5, \pm 4, \pm 3, \pm 2, \pm 1, 0$, hugely increasing the number of accessible excited states with respect to XAS.

A schematic drawing of a XRS process for $N_{4,5}$ edge of Ce^{3+} with the energy levels for the initial and final configurations and the simulated DDSCS are sketched in figure 3.2. The energy $\hbar(\omega_1 - \omega_2)$ lost by the photon in the scattering process is transferred to the system in the initial state $|i\rangle$ of configuration $4f^1$. The energy can excite a $4d$ electron promoting it into the $4f$ shell. In the image all the possible energy levels of the final configuration $4d^9 4f^2$ are shown. Through dipole transitions (blue) only some of them can be reached. Through higher order transitions (green and red) instead a higher number of final states can be reached.

3.3.2 Radial integrals

Focus now on Eq. 3.27, and in particular on the radial integral $\langle R_f | j_k(qr) | R_i \rangle$, which contains the dependence on the modulus of **q**. In our calculations the radial wave functions are the ones of the free ion and have been calculated within the Hartree-Fock approximation with the use of Cowan's code [30]. The results of the calculations of the radial integrals for the three different transitions allowed for the $4d \rightarrow 4f$ excitation in Ce^{3+}, Gd^{3+} and Ho^{3+} are shown in figure 3.3. They agree sufficiently well with the experiments but the resulting curves are spread out too much because the Hartree-Fock calculations yields radial integrals that are too tight. It is possible to see that the different transition orders k exhibit maxima at different values of q. This means that by controlling the exchanged momentum it is possible to select which transition (whether dipole, octupole or triakontadipole in this case) dominates the spectrum [57]. So, the dipole forbidden transitions can be favoured maximizing the exchanged momentum. Equation 3.15 suggests how to control the exchanged momentum in an experiment,

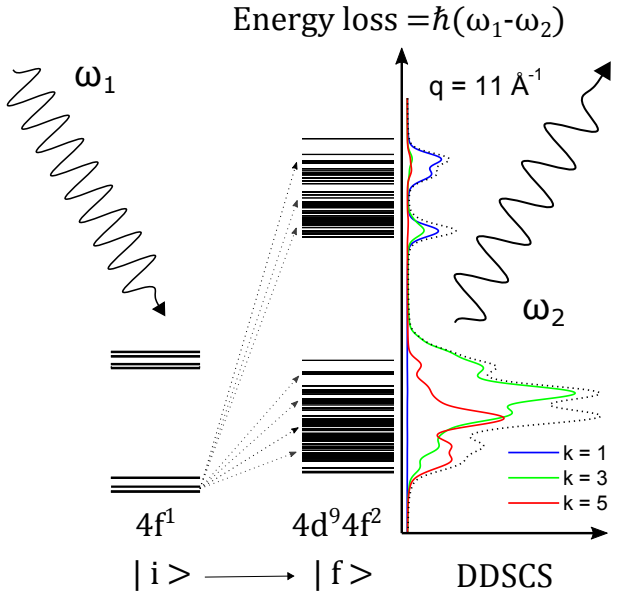

Figure 3.2: Schematic drawing of the NIXS process for the $N_{4,5}$ edge of Ce^{3+}. The energy loss $\hbar(\omega_1 - \omega_2)$ is the difference between the energy of the photon before and after the inelastic scattering process. This energy excites the system from the initial state $|i\rangle$ of configuration $4f^1$ to the final state $|f\rangle$ of configuration $4d^9 4f^2$. The energy levels and the DDSCS was calculated using Quanty. Through dipolar transitions (blue) only a limited number of final states can be reached. Higher order multipolar transitions (octupole in green, triakontadipole in red) allow to reach an higher number of final state energy levels.

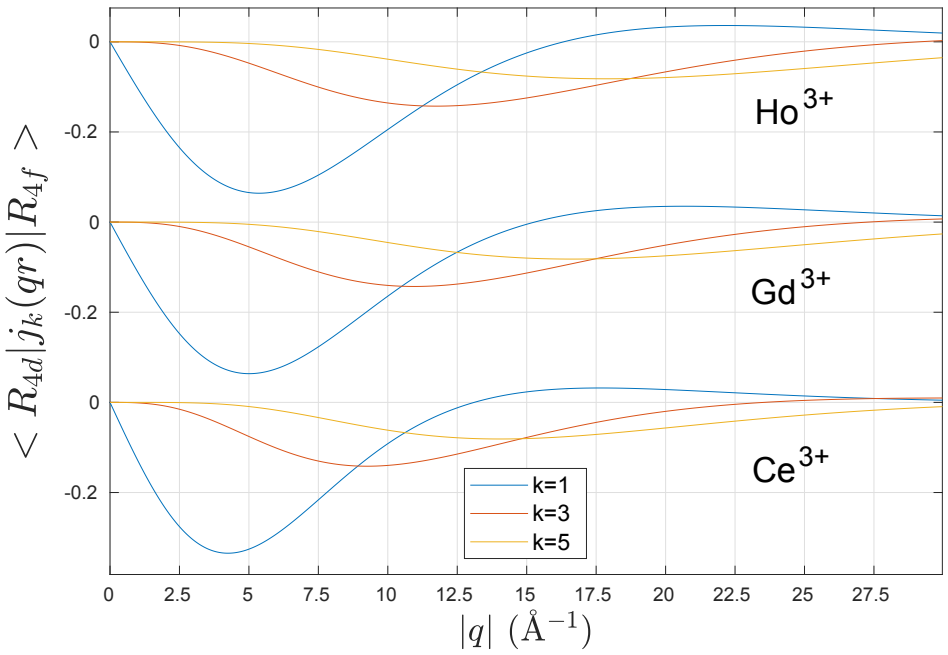

Figure 3.3: Plot of the radial integrals for the transition $4d \rightarrow 4f$ for the different ions Ce^{3+}, Gd^{3+} and Ho^{3+}. An higher atomic number (respectively 58, 64 and 67) results in a less extended radial wave function which thus results in maxima at a higher q.

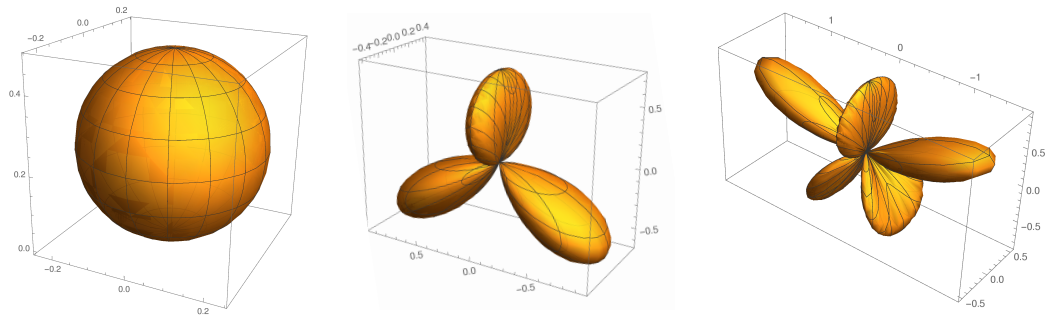

(a) (b) (c)

Figure 3.4: Plot of the angular part of the transition operators in case of coherent sum of all the terms: $\sum_m C_{k,m}(\theta_r, \phi_r)$. (a) $k = 1$ dipole, (b) $k = 3$ ocutpole and (c) $k = 5$ tetrakontadipole.

either by changing the scattering angle or changing the incident energy. The maximum possible q is obtained for $2\theta = \pi$ which means in a backscattering geometry, and the maximum possible obtainable exchanged q is higher the higher the energy of the incoming radiation is. Typically in NIXS experiments the energy of the incoming radiation is about $10\,\mathrm{keV}$, so in that case the highest possible q is given approximately by:

$$\frac{\hbar\omega \text{ eV}}{987\,\text{eV} \cdot \text{Å}} \approx 10\ \text{Å}^{-1}. \tag{3.30}$$

The radial integral is the highest if the initial and final radial wave functions have the same principal quantum number n. The higher the radial integral the higher will be the scattering probability and also the easier it will be to probe the multipolar transitions that can be reached with a lower q. So, for XRS experiments on rare earths it is more convenient to study the $N_{4,5}$ edge, which means the transition $4d \rightarrow 4f$, rather than the $M_{4,5}$ edge which corresponds to $3d \rightarrow 4f$ transitions [58]. The use of this shallow core excitation is also favorable for the previous approximation $\omega \ll \omega_1$.

3.3.3 Dichroism and lower symmetries sensitivity

The renormalized spherical harmonic $C^*_{k,m}(\theta_q, \phi_q)$ in eq. 3.27 is the only term that contains the dependence on the direction of the exchanged momentum $\mathbf{q}$. This is responsible for the natural dichroism observable for single crystal samples [59].

The symmetry of the dipole operator does not allow to XAS to resolve lower than 2-fold symmetries. For example the XAS spectra of a perfectly cubic system are the same for all the directions of the polarization. Instead, XRS allows to study higher order transitions. The corresponding operators have a lower symmetry with respect to the dipole operator, which means that they can resolve lower than 2-fold symmetries. This can be easily seen plotting the coherent sum over m for a given k of the angular part of the operators $\sum_m C_{k,m}(\theta_r, \phi_r)$.

This means that by analyzing the signal in the experimental spectra coming from the contribution of the higher multipole transitions it is possible to study lower than 2-fold symmetries.

CHAPTER 4

Experimental setups

The non-resonant inelastic x-ray scattering experimental data presented in this thesis on chapter 5.2 and chapter 6 were acquired at ID20 of the ESRF, which will be described in section 4.1. The description of this beamline and the experimental end-station follows the presentation in Ref. [60]. The x-ray absorption experiments instead, presented on chapter 6, were acquired at ID32 of the ESRF, which will be described in section 4.2.

4.1 ID20 beamline

4.1.1 Synchrotron radiation: undulators and x-ray optics

The main drawback of XRS is the orders of magnitude smaller scattering cross section in comparison with the probability for photoelectric absorption. This technique has become accessible with third generation synchrotron light sources due to their very high brilliance and thanks to the developments in the instrumentation that allows an efficient signal collection. Figure 4.1 shows the layout of the main components of the

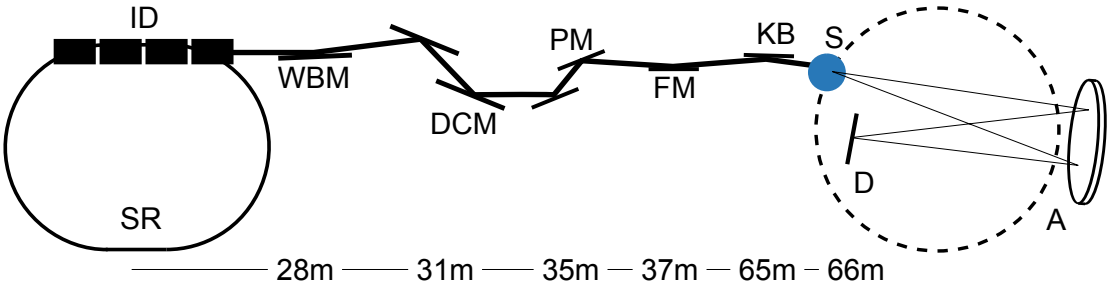

Figure 4.1: Layout of the ID20 beamline x-ray optics system.

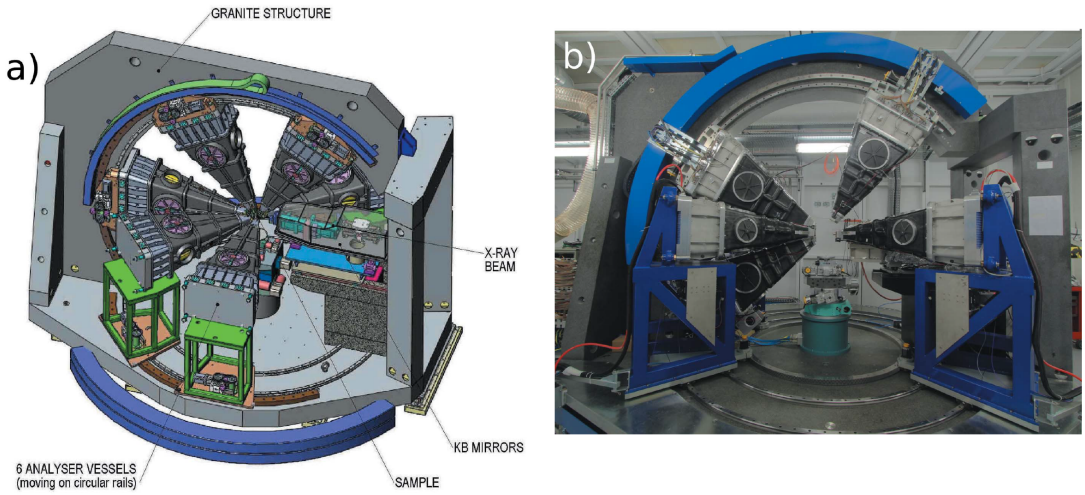

Figure 4.2: (a) Schematic view of the entire spectrometer assembly consisting of six independently movable crystal analyzer chambers, each hosting 12 spherically bent crystal analyzers. Three chambers are movable in the vertical plane and three in the horizontal plane. (b) Photo of the spectrometer installed in the experimental hutch.

x-ray optics of the ID20 beamline at the ESRF. The storage ring (SR) of the ESRF operates at a kinetic energy of $6\,\mathrm{GeV}$ with a maximum ring current of $200\,\mathrm{mA}$. The x-ray source for ID20 is an assembly of 4 undulators. Undulators are so-called insertion devices (ID) that consist of an array of magnets, which produce a magnetic field of alternating sign along the path of the electron beam [61]. This magnetic field configuration forces the electron beam to execute periodic oscillations in the horizontal plane as it traverses through the section. In this way the bremsstrahlung emitted by the accelerated electron adds coherently. This allows to have a collimated beam with a small energy spread (FWHM). Due to the finite number of magnets the undulator generates a quasi monochromatic spectrum (pink beam). The period, the distance between the magnets and the magnetic field strength determine the energy of the generated x-ray beam. Its energy is tuned usually changing the gap between the upper and lower row of permanent magnets while the undulator period is held constant.

Before impinging on the sample the beam goes through a series of x-ray mirrors. First a white-beam mirror (WBM) collimates the beam in the vertical plane and also serves as a heat-load filter for the successive liquid-nitrogen-cooled double crystal Si(111) pre-monochromator (DCM). In order to reach a better energy resolution a post-monochromator (PM) is used. In particular, a Si(311) channel-cut monochromator was used. The system of monochromators select the energy of the x-ray beam that impinges on the sample. Downstream, a toroidal mirror (FM) focuses the beam onto a secondary source. This secondary source is refocused by a Kirkpatrick-Baez (KB) mirror ensembly to a $10\,\mu\mathrm{m} \times 20\,\mu\mathrm{m}$ spot size (V $\times$ H) at the sample (S) position. The typical photon flux at the sample position at $9.7\,\mathrm{keV}$ for the described configuration is of about 1×10^{13} photons s^{-1}.

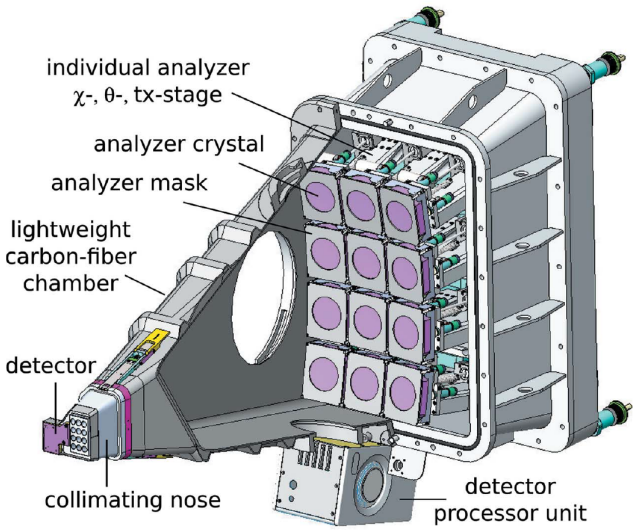

Figure 4.3: Sketch of an analyzer module hosting 12 analyzer crystals on a 1 m Rowland circle.

4.1.2 Spectrometer

The radiation scattered by the sample is then measured with the large solid angle spectrometer described in detail in [60] and shown in figure 4.2. Part (a) of this figure shows a schematic view of the spectrometer and part (b) a photo of the spectrometer installed at ID20. The spectrometer is composed of six independently movable crystal analyzer chambers, three in the horizontal and three in the vertical plane. This allowed to measure simultaneously the scattering at different angles and observe the dependence of the XRS spectra on the exchanged momentum q. The chambers were operated in a rough vacuum of approximately $10^{-1}\mathrm{mbar}$ in order to minimize absorption and parasitic scattering from air. The parasitic scattering was further reduced using collimators at the entrance of each of the analyzer module.

Each one of the 6 analyzer unit chambers contains 12 spherically bent Si(*nn*0) crystal analyzers, for a total of 72, as sketched in figure 4.3. Each individual analyzer crystal has three degrees of freedom (θ, χ and a translation along the beam direction). The crystal analyzers have a diameter of $100\,\mathrm{mm}$ but a mask with a diameter of $60\,\mathrm{mm}$ was used to increase the energy resolution. The spectrometer is based on Johann-type bent analyzer crystals with a radius of curvature of $1\,\mathrm{m}$. The fundamental concept is to have a crystal surface taking a shape that matches the request that all the x-rays from the sample impinging on the crystal have almost the same angle of incidence, as depicted in figure 4.4. This angle of incidence transfers to the corresponding energy of the Bragg reflection via Bragg's law. The best configuration to increase the energy resolution is the backscattering configuration, with the Bragg angle of $\pi/2$. This is impossible to obtain since it is necessary to reserve a certain amount of space for the sample and sample environment. In practice, the detector is placed inside the Rowland circle by a distance of $2z$. To maintain the focus of the analyzer onto the detector the crystal is consequently moved away by a distance z. This causes the Bragg angles to vary across the analyzer and as a consequence the energy bandwidth of the analyzer increases. The contribution of this broadening is given approximately by $\Delta E/E = zD\cot\Theta_B/R^2$,

where D is the active diameter of the analyzer crystal. This can become an important limiting factor in the total resolving power.

Since the measured quantity in a NIXS experiment depends only on the energy transfer $\omega = \omega_1 - \omega_2$ the exact values of ω_1 and ω_2 are less relevant. This allows one to simplify the design of a non-resonant IXS spectrometer because it is possible to run it in the so-called inverse geometry (Schülke): the energy analyzed by the analyzer crystals (ω_2) is fixed, while the incident energy (ω_1) is varied, consequently varying the exchanged energy (ω). In an experiment, to obtain the energy loss scale, a scan of the elastic peak is performed before performing the scan on the energy region of interest.

Recalling what was already said in 3.3.1, an IXS experiment consists in producing a well collimated and monochromatic x-ray beam and detecting the radiation scattered from the sample by an angle 2θ (thus fixing $\mathbf{q}$) into a solid angle element $d\Omega$ with an energy in the range dE_2, what is measured is the so called double differential scattering cross-section (DDSCS). It is possible to highlight which part of the spectrometer controls a certain quantity:

- the energy of the x-ray beam is controlled and scanned varying the Bragg angle of the monochromator(s);
- the scattering angles 2θ are determined by the individual position of the six crystal analyzer chambers;
- the exchanged momentum $\mathbf{q}$ for a given energy is determined by the position of the crystal analyzer chambers;
- the exchanged momentum $\mathbf{q}$ for a fixed scattering angle is determined by the energy of the x-ray beam;
- the solid angle $d\Omega$ is fixed by the active diameter of the crystal analyzers and their distance from the sample;
- the analyzed energy E_2 is kept fixed by the orientation (χ, θ, tx) of the individual crystal analyzer;
- the energy resolution dE_2 is determined by the performances of the monochromator(s) and of the crystal analyzers and other geometric contributions (source size, off-Rowland contribution, etc.).
- the DDSCS is measured as the number of counts detected by a photon-counting 2D detector (Maxipix).

Since q depends on the energy of the beam, during a scan, if the scattering angle is fixed, the value of the exchanged momentum changes, but for typical values $\Delta E_0/E_0 = 100/10000$ and since $\Delta q/q = \Delta E_0/E_0$ is obtained a $\Delta q = 0.1\text{Å}^{-1}$ for a $q = 10\text{Å}^{-1}$, which is negligible.

4.1.3 Sample environment

For the measurements performed at a temperature of $10\,\mathrm{K}$ the dynamic flow cryostat described in [62] was used. In figure 4.5 a picture of the cryostat installed in the experimental hutch of ID20 is shown. The six crystal analyzer modules are visible and

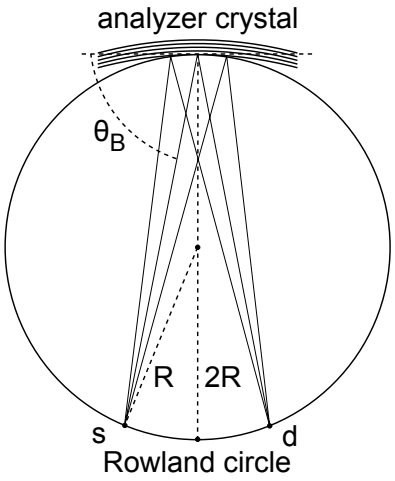

Figure 4.4: Schematic drawing of a Johann-type analyzer crystal. 2R is the radius of curvature of the analyzer crystal. If the sample (s) is placed onto the Rowland circle of radius R, this configuration has the property that all the x-rays coming from the sample impinge on the analyzer crystal with the same angle of incidence. In this way all the x-rays are Bragg reflected onto the point d where it is possible to place the detector.

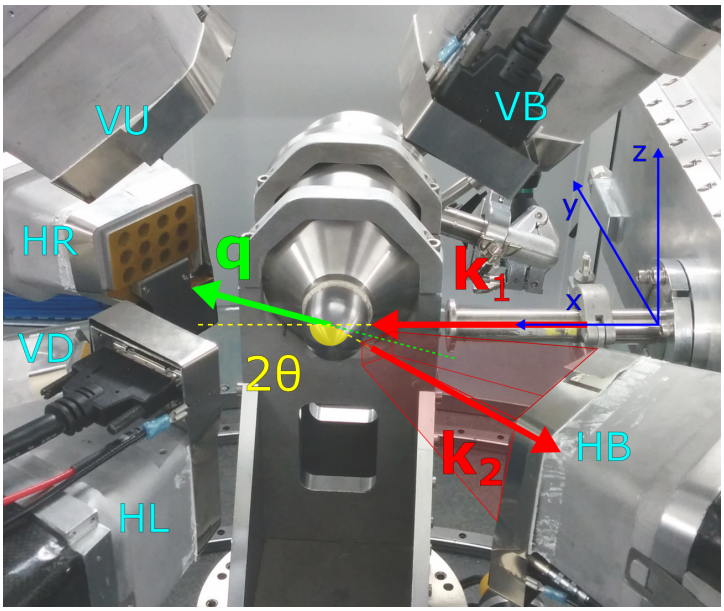

Figure 4.5: Picture of the cryostat installed in the experimental hutch of ID20. The geometry of the experiment is sketched. The incoming x-ray beam of wave vector $\mathbf{k}_1$ exits from the KB mirror chamber. The horizontal (moving on the plane xy) back (HB) module is placed at a scattering angle 2θ. It collects the x-rays scattered with wave vector $\mathbf{k}_2$ after the exchange of a momentum $\mathbf{q}$. The red shaded area corresponds qualitatively to the solid angle collected by the HB module.

labeled according to their position: vertical down (VD), vertical up (VU), horizontal left (HL) and horizontal right (HR) modules in the forward scattering direction, and vertical back (VB) and horizontal back (HB) modules for the backscattering one. The window of the cryostat allowed only for scattering on the horizontal plane. On top of the picture is sketched the geometry of the experiment. The x-ray beam exits from the KB mirror chamber with wave vector $\mathbf{k}_1$. The HB module collects the x-rays scattered at a scattering angle 2θ and wave vector $\mathbf{k}_2$. The red shaded area corresponds qualitatively to the solid angle collected by the HB module.

4.1.4 Data Analysis

ROIs selection

The crystal analyzers focus the scattered x-rays onto a 2D position sensitive detector. These are 2D Maxipix single photon counting detectors. Since each crystal analyzer can be moved independently, each focal spot is focused on a different point of the detector. Figure 4.6 (a) shows an image acquired with the spectrometer. The 2D images

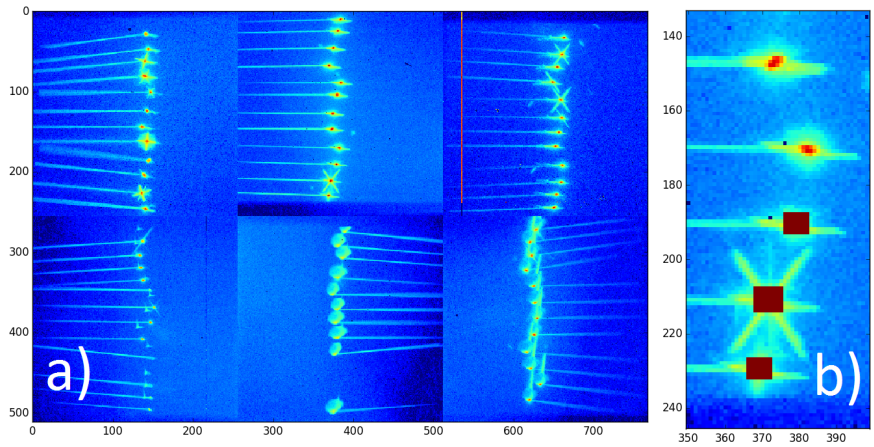

Figure 4.6: a) Composite image of all six 2D position sensitive detectors. Each of the 72 crystal analyzers is focused on a different point. The bright lines are the signal coming from the x-rays scattered by the air. b) A region of interest (ROI) has to be selected for every spot in order to cut out the signal not coming from the sample. Brown pixels are already selected areas.

of the six detectors are merged together in a single image that contains the signal from all the 72 crystal analyzers. The use of a position sensitive detector allows to select only the signal that comes from the sample, reducing the unwanted signal. This is useful when a complex environment like a cryostat is used. In this case, for example, the x-rays scattered from the windows of the cryostat can be cut out. This is obtained through the selection of the *regions of interest* (ROIs) in the image. In figure 4.6 (b), for example, the areas that have been already selected are shown in brown colour. The signal coming from all the 12 crystal analyzers of a single module are usually summed up. Also images acquired during different scans are summed. As an example, figure 4.7 shows all 12 spectra coming from a single crystal analyzer module.

Since the detector relies on x-ray absorption, which is governed by Poisson statistics the standard deviation is equal to $\sigma_{counts} = \sqrt{counts}$. Supposing for simplicity that the signal coming from the 12 crystal analyzer is the same, if all the spectra are summed the error is reduced by a factor $1/\sqrt{12}$.

Compton profile subtraction

In figure 4.8.(a) a scan performed on a long energy loss range on a polycristalline diamond sample is plotted. The spectrum of the edges lies on top of the so-called valence Compton profile. This contribution can have a much higher intensity than the near edge features. This scattering arises from the response of the valence electrons [63]. The energy position of the peak of the valence Compton profile is a function of the exchanged momentum q. In figure 4.8.(b) this dependence is shown. The position of the edge is independent on the value of q, so there will be cases in which the Compton profile is peaked at lower energy loss, at almost the same energy loss or at higher energy loss.

The shift of the peak of the Compton profile as a function of the exchanged momentum q is clear looking at the experimental spectra acquired at the $N_{4,5}$ edge ($109\,\mathrm{eV}$). In figure 4.9 the spectrum acquired with $q = 3.4$ Å^{-1} is shown. The Compton profile

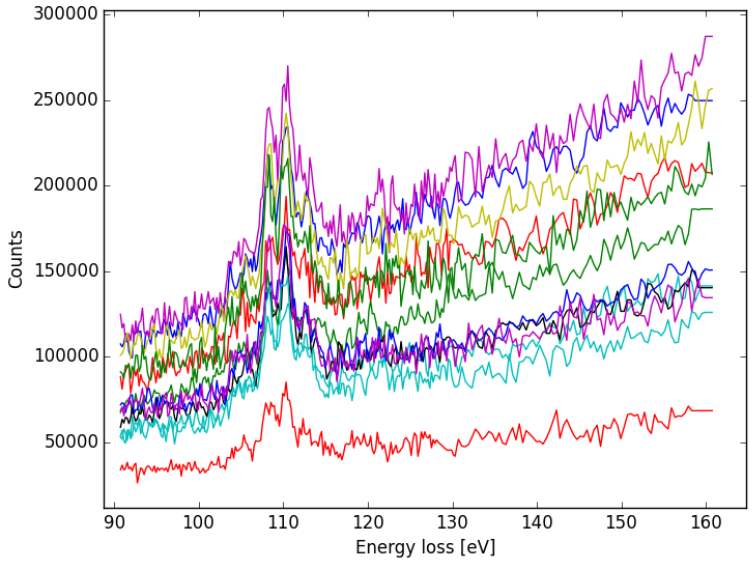

Figure 4.7: All the 12 spectra coming from the 12 crystal analyzers of a crystal analyzer module. All the spectra from a module are usually summed up.

is peaked at an energy lower than the energy of the Ce edge. Increasing the exchanged momentum to $q = 6.3$ Å^{-1} instead, as in figure 4.10, the edge lies right on top of the Compton profile. Further increasing the momentum transfer to $q = 8.5$ Å^{-1}, as in figure 4.11, the peak of the Compton profile is at higher energy losses than the edge.

In this thesis, the edge features are analyzed. In order to compare different spectra, the Compton profile has to be subtracted. In practice, the Compton profile is fitted from the experimental data. In figures 4.9, 4.10 and 4.11 the function interpolated from the background is plotted in green. The interpolating function is composed of: the shape of the Compton profile, modeled as a parametrized Pearson-VII function and a linear function, plus the response of the core electrons contributing with a step, that corresponds to the transitions into continuum states.

The background is fitted in the regions of the experimental spectra containing no signal from the edge features. For example, in the aforementioned figures possible intervals for the fitting of the Compton profile could be: $[90, 100]$eV and $[150, 160]$eV. In the figures is shown also in red the resulting spectra after the subtraction of the Compton profile (Pearson-VII and linear functions).

4.2 XAS

4.2.1 Experimental measurements

The XAS experimental data were acquired at ID32 [65, 66] of the ESRF using the total electron yield (TEY) technique.

To measure the absorption properties of a material it is possible to work in *transmission*, which means measuring the attenuation of x-rays as a function of energy by a sample of given thickness t. The quantity which describes the absorption is the linear

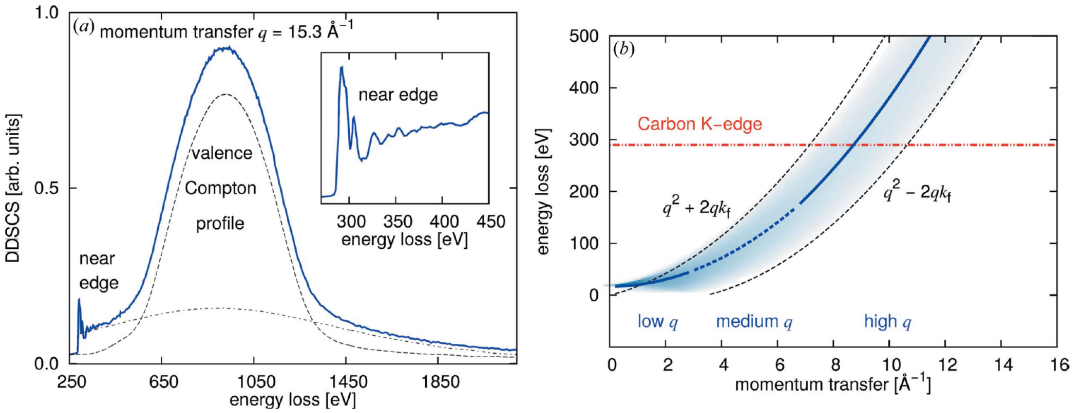

Figure 4.8: (a) Measured spectrum from polycristalline diamond with $q = 15.3\text{Å}^{-1}$. The response of the valence electrons leads to the valence Compton profile peaked at 950 eV; (b) Dispersion of the valence electron response. The valence Compton profile has its peak at different values depending on the value of q. Data taken from Huotari *et al.* (2012) [64].

Figure 4.9: Spectra acquired at the $N_{4,5}$ edge of Ce with $q = 3.4 \pm 0.2\text{Å}^{-1}$. The blue spectrum results from the sum of the signal from 12 crystal analyzers. The valence Compton profile is peaked at an energy value lower than the edge one. The red spectrum is obtained after the subtraction procedure.

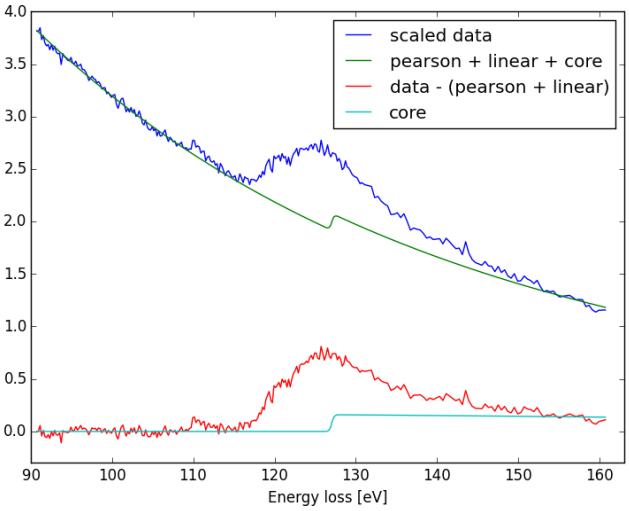

Figure 4.10: Spectra acquired at the $N_{4,5}$ edge of Ce with $q = 6.3 \pm 0.15\text{Å}^{-1}$. The blue spectrum results from the sum of the signal from 12 crystal analyzers. The edge features lie right on top of the valence Compton profile. The red spectrum is obtained after the subtraction procedure.

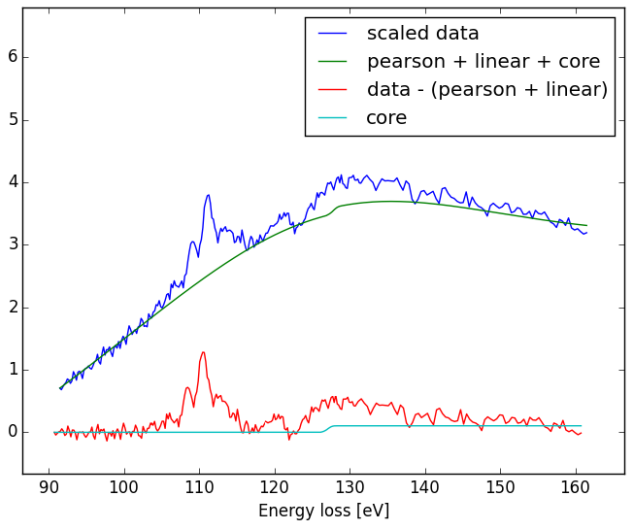

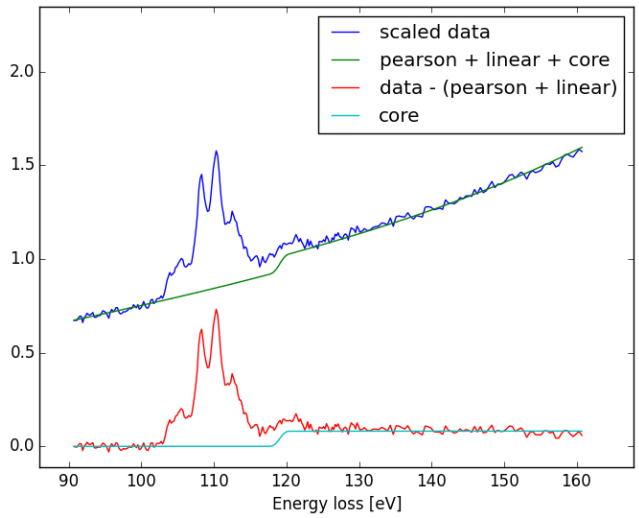

Figure 4.11: Spectra acquired at the $N_{4,5}$ edge of Ce with $q = 8.5 \pm 0.1 \text{Å}^{-1}$. The blue spectrum results from the sum of the signal from 12 crystal analyzers. The valence Compton profile is peaked at an energy value higher than the edge one. The red spectrum is obtained after the subtraction procedure.

absorption coefficient $\mu(\hbar\omega)$ and determines the transmitted intensity $I(\hbar\omega)$ as:

$$I(\hbar\omega) = I_0(\hbar\omega)e^{-\mu(\hbar\omega)\cdot t} \tag{4.1}$$

where $I_0(\hbar\omega)$ is the initial intensity and t is the thickness of the sample. But this technique requires thin, homogeneous samples and is not viable with soft x-rays because the absorption coefficient is too high.

However, is possible also to exploit the decay channels of the photo-generated core-hole. These techniques are called *yield modes* (see Figure 4.12), and are based on the assumption that the number of core-holes is proportional to the absorption coefficient. The measure of the intensity of the radiation re-emitted from the sample due to fluorescence processes it is called *total fluorescence yield* (TFY). However, this technique suffers from self-absorption, which means that the fluorescence photon can be reabsorbed in materials with a high absorption coefficient leading to a feedback mechanism, which can distort the spectrum. This issue should be carefully taken into account in the analysis. Another technique, which avoids this issue, is the *total electron yield* (TEY). In this kind of experiment the signal is the number of electrons emitted from the sample due to the Auger effect, electron scattering or photoionization. Electrically grounding the metallic sample every ejected electron will be compensated, so measuring the current that flows through the sample with an amperometer a measure of the number of emitted electrons is obtained. This quantity is proportional to the generated core-holes which is proportional to the absorption coefficient. Since the electrons have very small mean free path ($5\,\text{nm} - 50\,\text{nm}$) the information comes from the first layers of the material and this technique avoids the problems of self absorption.

4.2.2 Background subtraction and normalization

The data were divided for every energy value by the estimate of the value of the incident x-ray intensity. Successively the edge step is subtracted. The edge step is fitted from the signal in the regions indicated in figure 4.13 where there are no edge features. The fitting is performed using two arctangent functions centered respectively at $883.5\,\text{eV}$ and $903.0\,\text{eV}$ and a linear function:

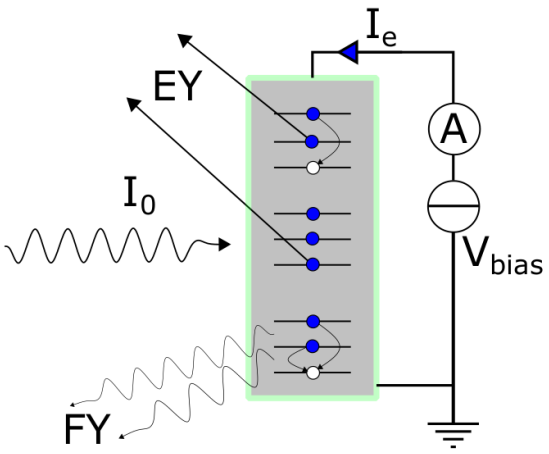

Figure 4.12: Schematic drawing of a XAS TY experiment. The amount of radiation absorbed from the impinging intensity I_0 is proportional to the number of generated electron-holes. In a *total fluorescence yield* (TFY) experiment the radiation re-emitted from the sample is measured with a photodiode. In a *total electron yield* (TEY) experiment the number of electrons that are emitted from the sample by Auger effect, through electron electron scattering or through photoionization can be measured with amperometer. In metallic materials an electron current provided by the V_{bias} compensates for the electrons that leave the material.

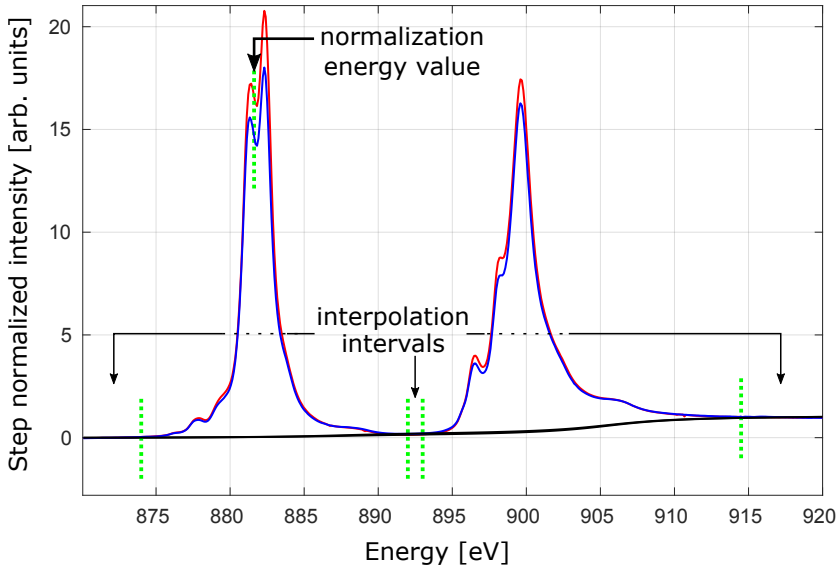

Figure 4.13: XAS background subtraction and normalization. In green are delimited the intervals used for the interpolation of the function in equation 4.2. In black are plotted the functions obtained from the interpolation.

$$f(x) = g_1 \cdot (g_2 + \arctan\left(\frac{x - 883.5}{4}\right)) + \\ + g_3 \cdot (g_4 + \arctan\left(\frac{x - 903.0}{4}\right)) + g_5 \cdot x + g_6, \tag{4.2}$$

where $f(x)$ is the function that is subtracted to the experimental spectrum after the best fitting of the six parameters g_{1-6}. The spectra are then normalized dividing each spectrum by its value in the point where it is expected that the dichroism is zero. As will be shown in section 6.3 all the simulations show a zero in the dichroism for a point at an energy $881.5\,\mathrm{eV}$.

CHAPTER 5

Atomic multiplet calculation of XAS and XRS spectra: Quanty

In the following sections it is shown in a practical way how to convert the models developed in chapter 2 and chapter 3 into a Quanty (`http://www.quanty.org/`) script. Quanty can be used to simulate a variety of different core level spectroscopies using different approximations. In this discussion an atomic multiplet approach is used to describe a Ce^{3+} ion in a tetragonal crystal field. The script to calculate the XAS and XRS spectra will be built piece by piece. In the last section 5.2 it is shown how these calculations can be used to analyze the spectra of rare earth elements, their strength and their limits.

5.1 Quanty: a quantum many body script language

Quanty is a scripting language based on the programming language Lua that provides tools to solve complex many body problems. Quanty solves many problems that are encountered on many body calculations but provides to the user an high scripting language. Both the basis states and the operators are expressed in second quantization in terms of creation and annihilation operators. Following the philosophy of Quanty, the complexity of the operators in second quantization will be hidden when not relevant. A detailed documentation can be found in Ref. [67].

5.1.1 Atomic shells

Basis states

The many body wave functions are expressed in terms of one particle modes. These are the basis states and describe whether an orbital is occupied by a particle or not. The

orbitals are given by a radial and an angular part. As in equation 2.5, the orbitals ψ_{k_i} are given as a product of a radial part and an angular part as in $\psi_{k_i} = R_{nl}(r)Y_{lm_l}(\theta, \phi)$. By default, Quanty uses the complex spherical harmonics for the angular part. Also the spin part can be defined creating the so called spin-orbitals. Bases with more than one electron will be given by Slater determinant basis states. A many particle state is written then as a linear combination of Slater determinants.

To define an atomic shell one has to group the necessary number of spin-orbitals. Grouping a number n of orbitals, as in the following code, automatically lets Quanty know that the user is describing an atomic shell with orbital angular momentum quantum number $l = (n-1)/2$ and the spin-orbitals have to be labeled through the quantum number $m_l = -l, ..., l$.

```
-- Definition of the electronic shells
-- Total number of Fermionic and Bosonic modes
NBosons = 0
NFermions = 24

-- Creation of the basis sets defined by one particle spin-orbitals
-- d shell
IndexDn_4d = {0, 2, 4, 6, 8}
IndexUp_4d = {1, 3, 5, 7, 9}
-- f shell
IndexDn_4f = {10, 12, 14, 16, 18, 20, 22}
IndexUp_4f = {11, 13, 15, 17, 19, 21, 23}
```

Spin-orbit interaction

To create operators that act on these states one can use the function NewOperator(). With this function the operators describing the atomic Hamiltonian can be defined. There are several standard operators already defined. For example the spin-orbit operator $\zeta_{nl}\, \boldsymbol{l} \cdot \boldsymbol{s}$ of equation 2.9 can be defined as in the following code:

```
-- Definition of the spin-orbit term.
-- initialization of the hamiltonian
H_i = 0
H_f = 0
-- creation of the spin-orbit operators l*s for the 2 shells
ldots_4f = NewOperator('ldots', NFermions, IndexUp_4f, IndexDn_4f)

ldots_4d = NewOperator('ldots', NFermions, IndexUp_4d, IndexDn_4d)

-- scaling of the spin-orbit HF value
scal_zeta_4f = 0.88
scal_zeta_4d = 0.97

-- initial spin orbit interaction parameter zeta4f
zeta_4f_i = 0.087 * scal_zeta_4f

-- final spin orbit interaction parameter zeta4f and zeta 4d
zeta_4f_f = 0.0913 * scal_zeta_4f
zeta_4d_f = 1.2444 * scal_zeta_4d

-- creation of the spin-orbit Hamiltonians: H_so = zeta*l*s
    H_i = H_i + Chop(
          zeta_4f_i * ldots_4f)

    H_f = H_f + Chop(
```

```
        zeta_4f_f * ldots_4f
      + zeta_4d_f * ldots_4d)
```

H_i and H_f are the Hamiltonians describing the atomic system in the initial electronic configuration $4f^1$ and final configuration $4d^9 4f^2$, respectively. The values of the spin-orbit coupling ζ_{4f} and ζ_{4d} are obtained from Hartree-Fock calculations for the initial and final configurations. The values were taken from Crispy, a graphical user interface to generate Quanty input files. These values have to be scaled by scal_zeta_4f and scal_zeta_4d in order to best fit the experimental data (see appendix A).

Electron-electron interaction

The interaction between the electrons is introduced via the Slater integrals as defined in equation 2.12. They contribute to the Hamiltonian as $\sum_k f_k F^k + \sum_k g_k G^k$. Selection rules govern which of the coefficients f_k and g_k are non-null. In the initial configuration $4f^1$ there is no electron-electron interaction contributions. In the final configuration $4d^9 4f^2$, instead, there is an interaction between the two f electrons, which is described by the terms $F^2, F^4$and F^6. There is further an interaction between the $4f$ electrons and the $4d$ hole, which is described by the terms F^2, F^4, G^1, G^3 and G^5. The associated operators can be created in Quanty using the Coulomb repulsion operator (U). The contributes of order $k = 0$ are neglected because their contribute just shifts the spectrum.

```
-- ------------------------------------------------------------------------
-- Definition of the Coulomb repulsion operators:
-- Fk and Gk Slater integrals
-- ------------------------------------------------------------------------

-- Operators describing the 4f-4f electrons interaction
F2_4f_4f = NewOperator('U', NFermions, IndexUp_4f, IndexDn_4f, {0, 1, 0, 0})
F4_4f_4f = NewOperator('U', NFermions, IndexUp_4f, IndexDn_4f, {0, 0, 1, 0})
F6_4f_4f = NewOperator('U', NFermions, IndexUp_4f, IndexDn_4f, {0, 0, 0, 1})

-- Operators describing the 4d-4f electrons interaction
F2_4d_4f = NewOperator('U', NFermions, IndexUp_4d, IndexDn_4d,
                       IndexUp_4f, IndexDn_4f, {0, 1, 0}, {0, 0, 0});
F4_4d_4f = NewOperator('U', NFermions, IndexUp_4d, IndexDn_4d,
                       IndexUp_4f, IndexDn_4f, {0, 0, 1}, {0, 0, 0});
G1_4d_4f = NewOperator('U', NFermions, IndexUp_4d, IndexDn_4d,
                       IndexUp_4f, IndexDn_4f, {0, 0, 0}, {1, 0, 0});
G3_4d_4f = NewOperator('U', NFermions, IndexUp_4d, IndexDn_4d,
                       IndexUp_4f, IndexDn_4f, {0, 0, 0}, {0, 1, 0});
G5_4d_4f = NewOperator('U', NFermions, IndexUp_4d, IndexDn_4d,
                       IndexUp_4f, IndexDn_4f, {0, 0, 0}, {0, 0, 1});
```

The values of the Slater Integrals F^k and G^k can be calculated using Hartree-Fock calculations and in this case are tabulated in Crispy [68]. As for the spin orbit parameter, their values have to be scaled by a quantity scal_4f4f and scal_4d4f in order to fit the experimental data.

```
-- Scaling of the Slater-Condon HF values
scal_4f4f = 0.7
scal_4d4f = 0.78

-- initial configuration 4f1
F2_4f_4f_i = 0.0
F4_4f_4f_i = 0.0
F6_4f_4f_i = 0.0

-- final configuration 4d9 4f2
```

```
F2_4f_4f_f = 11.9732 * scal_4f4f
F4_4f_4f_f = 7.5185 * scal_4f4f
F6_4f_4f_f = 5.4106 * scal_4f4f

F2_4d_4f_f = 13.611 * scal_4d4f
F4_4d_4f_f = 8.682 * scal_4d4f
G1_4d_4f_f = 16.1569 * scal_4d4f
G3_4d_4f_f = 10.0831 * scal_4d4f
G5_4d_4f_f = 7.1143 * scal_4d4f

-- creation of the Coulomb Hamiltonian in the initial and final state
    H_i =  H_i + chop(
        F2_4f_4f_i * F2_4f_4f
          + F4_4f_4f_i * F4_4f_4f
          + F6_4f_4f_i * F6_4f_4f)

    H_f =  H_f + chop(
        F2_4f_4f_f * F2_4f_4f
          + F4_4f_4f_f * F4_4f_4f
          + F6_4f_4f_f * F6_4f_4f
          + F2_4d_4f_f * F2_4d_4f
          + F4_4d_4f_f * F4_4d_4f
          + G1_4d_4f_f * G1_4d_4f
          + G3_4d_4f_f * G3_4d_4f
          + G5_4d_4f_f * G5_4d_4f)
```

Effective crystal field

The Hamiltonians H_i and H_f built up to this point can describe an isolated Ce^{3+} ion. It is possible to introduce the effective crystal field Hamiltonian of equation 2.15, which in second quantization can be written as:

$$H_{CEF} = \sum_{\tau_1,\tau_2} \sum_{k,m} A_k^m \langle Y_{l_1,m_1} | C_{k,m} | Y_{l_2,m_2} \rangle a_{\tau_1}^\dagger a_{\tau_2}, \tag{5.1}$$

where τ represents the combination of the quantum numbers $nlms$, $a_{\tau_1}^\dagger$ is the creation operator which creates an electron in the spin-orbital with quantum numbers τ_1, while a_{τ_2} is the annihilation operator. As pointed out in chapter 2.3 the only terms that act on the Ce^{3+} are the $A_2^0, A_4^0, A_4^{\pm 4}$. This operator can be created using the function NewOperator('CF', ..., Akm) with the first input string 'CF' and as last input a list of the crystal field parameters of the form: $\{\{k_1, m_1, A_{k_1}^{m_1}\}, \{k_2, m_2, A_{k_2}^{m_2}\}, ...\}$

```
-------------------------------------------------------------------------------
-- Definition of the crystal field operator
-------------------------------------------------------------------------------
-- assign values to the Crystal Field parameters A_km
A20 = -0.015
A40 =  0.023
A44 =  0.025

Akm = {{0, 0, 0} ,
       {2, 0, A20} ,
       {4, 0, A40} ,
       {4,-4, A44} ,
       {4, 4, A44} }

-- creation of the crystal field operator 'CF' acting on the 4f shell
  H_i = H_i + Chop(NewOperator('CF', NFermions, IndexUp_4f, IndexDn_4f, Akm))

  H_f = H_f + Chop(NewOperator('CF', NFermions, IndexUp_4f, IndexDn_4f, Akm))
```

The function NewOperator() allows one to create several different operators, for example the following one with intuitive meaning:

```
Sx_4f = NewOperator('Sx', NFermions, IndexUp_4f, IndexDn_4f)
Sy_4f = NewOperator('Sy', NFermions, IndexUp_4f, IndexDn_4f)
Sz_4f = NewOperator('Sz', NFermions, IndexUp_4f, IndexDn_4f)
Ssqr_4f = NewOperator('Ssqr', NFermions, IndexUp_4f, IndexDn_4f)

Lx_4f = NewOperator('Lx', NFermions, IndexUp_4f, IndexDn_4f)
Ly_4f = NewOperator('Ly', NFermions, IndexUp_4f, IndexDn_4f)
Lz_4f = NewOperator('Lz', NFermions, IndexUp_4f, IndexDn_4f)
Lsqr_4f = NewOperator('Lsqr', NFermions, IndexUp_4f, IndexDn_4f)

Jx_4f = NewOperator('Jx', NFermions, IndexUp_4f, IndexDn_4f)
Jy_4f = NewOperator('Jy', NFermions, IndexUp_4f, IndexDn_4f)
Jz_4f = NewOperator('Jz', NFermions, IndexUp_4f, IndexDn_4f)
Jsqr_4f = NewOperator('Jsqr', NFermions, IndexUp_4f, IndexDn_4f)
```

These operators allow one to add a term describing the interaction with a magnetic field to the Hamiltonian.

```
-- magnetic field expressed in eV
    Bx_i = 0.0
    By_i = 0
    Bz_i = 1e-07

    Bx_f = 0.0
    By_f = 0
    Bz_f = 1e-07

    H_i = H_i + Chop(
          Bx_i * (2 * Sx_4f + Lx_4f)
        + By_i * (2 * Sy_4f + Ly_4f)
        + Bz_i * (2 * Sz_4f + Lz_4f))

    H_f = H_f + Chop(
          Bx_f * (2 * Sx_4f + Lx_4f)
        + By_f * (2 * Sy_4f + Ly_4f)
        + Bz_f * (2 * Sz_4f + Lz_4f))
```

Eigenfunctions

Note that the number of electrons in the shells has not been specified until now. This is because no actual calculation has been performed until this moment, only operators have been stored in memory. To calculate the initial state wave functions one needs to define through some restrictions the occupation of the shells and the number of states to compute:

```
-- Definition of the restrictions and of the number of initial states
-- for the calculation of the initial state wavefunctions
NElectrons_4d = 10
NElectrons_4f = 1

InitialRestrictions = {  NFermions, NBosons,
            {'1111111111 00000000000000', NElectrons_4d, NElectrons_4d},
                      {'0000000000 11111111111111', NElectrons_4f, NElectrons_4f} }

-- number of initial state wavefunctions to compute
NPsis = 14
-- calculation of the eigenfunctions of the initial hamiltonian
Psis_i = Eigensystem(H_i, InitialRestrictions, NPsis)

print(Psis_i[1])
```

Psis_i is a list which contains the calculated wave functions expressed as a list of creation operators which represent the linear combination of the Slater determinants needed to describe the many particle state. Using print(Psis_i[1]) information about the first wave function is printed on the terminal:

```
WaveFunction: Wave Function
QComplex          =          0 (Real==0 or Complex==1)
N                 =         14 (Number of basis functions used to discribe psi)
NFermionic modes  =         24 (Number of fermions in the one particle basis)
NBosonic modes    =          0 (Number of bosons in the one particle basis)

#       pre-factor          Determinant
   1   1.578810408582E-01       111111111100000000000100
   2  -3.355346558658E-01       111111111100000000000010
   3  -7.853377779514E-01       111111111100010000000000
   4   4.957162960534E-01       111111111100001000000000
   5   0.000000000000E+00       111111111101000000000000
   6   0.000000000000E+00       111111111100100000000000
   7   0.000000000000E+00       111111111100000000010000
   8   0.000000000000E+00       111111111100000000000001
   9   0.000000000000E+00       111111111100000100000000
  10   0.000000000000E+00       111111111100000000001000
  11   0.000000000000E+00       111111111110000000000000
  12   0.000000000000E+00       111111111100000000100000
  13   0.000000000000E+00       111111111100000001000000
  14   0.000000000000E+00       111111111100000010000000
```

This does not give much information about the wave function. It is most useful to calculate the expectation values of some operators on the wave functions. It possible to calculate expectation values of the operators simply through the expression Psi*Operator*Psi, which Quanty interprets as the expectation value $\langle \mathrm{Psi} | \, \mathrm{Operator} \, | \mathrm{Psi} \rangle$. Creating a list of operators it is possible to get information on the obtained wave functions:

```
-- Print details about all the initial states
-- List of operators of which to calculate the expectation value
Operators = {H_i, Ssqr_4f, Lsqr_4f, ldots_4f, Jsqr_4f, Sz_4f, Lz_4f, Jz_4f}

header = 'Analysis of the initial Hamiltonian:\n'
header = header .. '=============================================================\n'
header = header .. 'State <E> <S^2> <L^2> <l.s> <J^2> <Sz> <Lz> <Jz> \n'
header = header .. '=============================================================\n'
footer = '=============================================================================\n'
io.write(header)
for i, Psi in ipairs(Psis_i) do
    io.write(string.format('%5d', i))
    for j, Operator in ipairs(Operators) do

    -- the expectation value is simply performed as
    -- Psi*Operator*Psi which stands for <Psi|Operator|Psi>
        io.write(string.format('%10.4f', Complex.Re(Psi * Operator * Psi)))

    end
    io.write('\n')
end
io.write(footer)
```

Running this code in Quanty one gets as output the following lines on the terminal:

```
Analysis of the initial Hamiltonian:
================================================================================================
  State      <E>       <S^2>      <L^2>      <l.s>      <J^2>      <Sz>       <Lz>       <Jz>
================================================================================================
    1    -0.1591     0.7500    12.0000    -1.9987     8.7526     0.1417    -1.0916    -0.9500
    2    -0.1591     0.7500    12.0000    -1.9987     8.7526    -0.1417     1.0916     0.9499
    3    -0.1544     0.7500    12.0000    -1.9993     8.7514     0.0762    -0.5755    -0.4993
```

4	−0.1544	0.7500	12.0000	−1.9993	8.7514	−0.0762	0.5755	0.4993
5	−0.1460	0.7500	12.0000	−1.9993	8.7514	0.2690	−2.2194	−1.9504
6	−0.1460	0.7500	12.0000	−1.9993	8.7514	−0.2691	2.2195	1.9504
7	0.1071	0.7500	12.0000	1.4993	15.7486	−0.0617	−0.4455	−0.5071
8	0.1071	0.7500	12.0000	1.4993	15.7486	0.0616	0.4453	0.5069
9	0.1128	0.7500	12.0000	1.4997	15.7494	−0.0175	−0.0464	−0.0639
10	0.1128	0.7500	12.0000	1.4997	15.7494	0.0174	0.0464	0.0638
11	0.1165	0.7500	12.0000	1.4987	15.7474	−0.0657	−0.4267	−0.4924
12	0.1165	0.7500	12.0000	1.4987	15.7474	0.0657	0.4268	0.4926
13	0.1231	0.7500	12.0000	1.4996	15.7491	−0.4413	−2.6218	−3.0631
14	0.1231	0.7500	12.0000	1.4996	15.7491	0.4413	2.6219	3.0632

The 14 states are ordered from the one with lowest energy one to the one with highest energy. All the Levels are characterized by the same expectation value of the spin and orbital angular momentum: $< S^2 >= S(S+1) = 0.75$, which means $S = 1/2$, and $< L^2 >= L(L+1) = 12$ implies $L = 3$. Which means that the 14 states can be labelled with the spectroscopic term ${}^2F$. They differ in terms of spin-orbit interaction. For the first 6 levels this interaction reduces the energy as can be seen from the negative expectation value of the $\mathbf{l} \cdot \mathbf{s}$ operator. The remaining 8 levels are increased in energy instead. For the first 6 levels the spin and angular momentum operators S_z and L_z have opposite sign, which means that the total angular momentum is given by $J = L - S = 5/2$. The first 6 states belong to the ${}^2F_{5/2}$ multiplet. The remaining states instead to the ${}^2F_{7/2}$ multiplet. This is confirmed by the expectation value of the operator J^2.

The levels of the ${}^2F_{5/2}$ are not degenerate with respect to the magnetic quantum number $m_J = \pm 1/2, \pm 3/2, \pm 5/2$ due to the effect of the crystal field. The levels are coupled in Kramer's doublets and each couple is characterized by the modulus of the expectation value of the operator J_z. These doublets are the Γ levels described in equation 2.20. The order of the doublets in this case is $\Gamma_7^1 - \Gamma_6 - \Gamma_7^2$. The value of $< J_z >$ differs from that of the degenerate states, which would be given by $< J_z^{pure} >= m_J = \pm 1/2, \pm 3/2, \pm 5/2$. Identifying among the levels the level Γ_7^1 it is possible to determine from its value of $< J_z >$ the mixing parameter α because it is given by

$$\left\langle \Gamma_7^1 | J_z | \Gamma_7^1 \right\rangle = \pm \left(\alpha^2 \frac{5}{2} - (1-\alpha^2)\frac{3}{2} \right). \tag{5.2}$$

Usually the values of α estimated in this way are very close to the values given by equation 2.21. A big difference between the two values means that the intermixing with the ${}^2F_{7/2}$ multiplet cannot be neglected.

From the wave functions is possible to obtain the density matrix and obtain the list of spherical harmonics needed to describe the angular electronic density of the spin-orbital. In this way, it is possible to plot the angular part of the electronic density of the spin-orbitals. In figure 5.1 the densities for the Γ_7^1, Γ_6 and Γ_7^2 states are plotted. One can intuitively guess, looking at the anisotropic distribution of the orbitals, that these states will respond differently to an incoming photon depending on the direction of its polarization.

State	<E>	<Jz>
1	−0.1591	−0.9500
2	−0.1591	0.9499
3	−0.1544	−0.4993
4	−0.1544	0.4993
5	−0.1460	−1.9504
6	−0.1460	1.9504

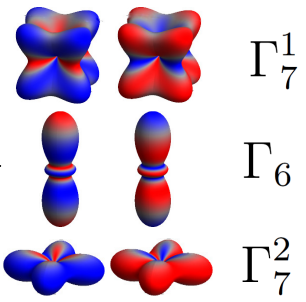

Figure 5.1: Energy levels, expectation value of the operator J_z and density plot of the spin-orbitals of the crystal field states Γ_7^1, Γ_6 and Γ_7^2 of Ce^{3+}.

5.1.2 X-ray spectroscopy operators

In Quanty the complex energy dependent spectra $G(\omega)$ are obtained calculating the Green's function:

$$G(\omega) = \left\langle \Psi_i \left| T^\dagger \frac{1}{\omega - H_f + i\Gamma/2} T \right| \Psi_i \right\rangle. \tag{5.3}$$

Ψ_i are the many particle initial wave functions, T is the transition operator, H_f is the final Hamiltonian and Γ is the Lorentzian broadening to take into account the energy broadening due to finite lifetime of the core-hole. The quantities measured in the experiments are proportional to the imaginary part of $G(\omega)$ [69].

XAS

As described in chapter 3.2.2 the transition operator for XAS is $T = \mathbf{e} \cdot \hat{\mathbf{r}}$, where $\mathbf{e} = (e_x, e_y, e_z)$ is the unit vector of the polarization and $\hat{\mathbf{r}}$ is the position operator. This operator is conveniently expressed in terms of renormalized spherical Harmonics as:

$$\mathbf{e} \cdot \hat{\mathbf{r}} = (e_x + ie_y)C_{1,-1} + e_z C_{1,0} + (-e_x + ie_y)C_{1,1} \tag{5.4}$$

In this way it is possible to use the function NewOperator('CF', ..., Akm) as done for the crystal field operator. In this case the coefficients of the complex spherical harmonics are: $A_{1,-1} = e_x + ie_y$, $A_{1,0} = e_z$, $A_{1,1} = -e_x + ie_y$.

```
-- Definition of the Trasition operator T = e*r and calculation of the spectrum

theta = 90
phi   = 0

ex= math.sin(math.rad(theta))*math.sin(math.rad(phi))
ey= math.cos(math.rad(phi))
ez= math.cos(math.rad(theta))*math.sin(math.rad(phi))

Akm = {{1, -1,( ex + I * ey)/math.sqrt(2)},
       {1,  0,  ez},
       {1,  1,(-ex + I * ey)/math.sqrt(2)}}

T = NewOperator('CF', NFermions, IndexUp_4f, IndexDn_4f, IndexUp_3d, IndexDn_3d, Akm)

-- calculation of the spectrum
XAS_spectrum = CreateSpectra(H_f, T, Psi_i, {{"Emin",-10}, {"Emax",20}, {"NE",3500}})
```

NIXS

As shown in chapter 3.3.1, the transition operator that describes the non-resonant inelastic x-ray scattering is $T = e^{i\mathbf{q}\cdot\mathbf{r}}$ which can be separated into an operator acting on the radial and one on the angular part of the wave functions:

$$T = \sum_{k=0}^{\infty} \sum_{m=-k}^{k} T_{k,m}^{rad} T_{k,m}^{ang}, \tag{5.5}$$

where

$$T_{k,m}^{rad} = i^k (2k+1) j_k(qr) C_{k,m}^*(\theta_q, \phi_q), \tag{5.6}$$

and

$$T_{k,m}^{ang} = C_{k,m}(\theta_r, \phi_r). \tag{5.7}$$

The radial operator gives rise to radial integrals $\langle R_f | \, j_k(qr) \, | R_i \rangle$. The modulus of q and its angular coordinates θ_q, ϕ_q are fixed parameters chosen to reproduce the experimental ones. The radial wave functions can be calculated for example by means of Hartree-Fock calculations and then loaded into Quanty where the radial integrals can be evaluated.

```
--------------------------------------------------------------------------------
-- NIXS operator definition
--------------------------------------------------------------------------------
-- the transition operator is given by  Akm * C(theta_r, phi_r)
-- where Akm = i^k.(2k+1).C^*(theta_q, phi_q).<R(r)|j_k(q r)|R(r)>
-- which is a potential expanded on spherical harmonics with coefficients Akm

-- read the radial wave functions from a file
-- order of the radial functions in the file
-- r(a0)  4d  5s  5p  4f
file = io.open( "Ce_radial_4f.txt", "r")
Rnl = {}
for line in file:lines() do
  RnlLine={}
  for i in string.gmatch(line, "%S+") do
    table.insert(RnlLine,i)
  end
  table.insert(Rnl,RnlLine)
end

-- transitions from 4d (index 2 in Rnl) to 4f (index 5 in Rnl)
-- calculation of the radial integral <R(r) | j_k(q r) | R(r)>  for a chosen  q
function RjRpd (q)
  Rj1R = 0
  Rj3R = 0
  Rj5R = 0
  dr = Rnl[3][1]-Rnl[2][1]
  r0 = Rnl[2][1]-2*dr
  for ir = 2, #Rnl, 1 do
    r = r0 + ir * dr
    Rj1R = Rj1R + Rnl[ir][2] * math.SphericalBesselJ(1,q*r) * Rnl[ir][5] * dr
    Rj3R = Rj3R + Rnl[ir][2] * math.SphericalBesselJ(3,q*r) * Rnl[ir][5] * dr
    Rj5R = Rj5R + Rnl[ir][2] * math.SphericalBesselJ(5,q*r) * Rnl[ir][5] * dr
  end
  return Rj1R, Rj3R, Rj5R
end
```

The transition operator acting on the angular part of the wave function that has to be used in the function CreateSpectra() is then:

$$T = \sum_{k,m} A_{k,m} \, C_{k,m}(\theta_r, \phi_r), \tag{5.8}$$

where

$$A_{k,m} = i^k(2k+1)C^*_{k,m}(\theta_q, \phi_q) \langle R_f | j_k(qr) | R_i \rangle . \tag{5.9}$$

This is a potential expanded in spherical Harmonics with coefficients $A_{k,m}$. This means that the function NewOperator('CF', ..., Akm) can be used.

```
-- creation of the list of the coefficients
-- Akm = i^k.(2k+1).C^*(theta_q, phi_q).<R(r)|j_k(q r)|R(r)>
function ExpandOnClm(k,theta,phi,scale)
  ret={}
  for m=-k, k, 1 do
    table.insert(ret,{k,m,scale * math.SphericalHarmonicC(k,m,theta,phi)})
  end
  return ret
end

-- function to create the nIXS transition operators
-- calling all the previous functions
function TnIXS_pd(q, theta, phi)
  Rj1R, Rj3R, Rj5R = RjRpd(q)

  k=1
  A1 = ExpandOnClm(k, theta, phi, I*(2*k+1)*Rj1R)
  T1 = NewOperator("CF", NFermions, IndexUp_4f, IndexDn_4f,
                                    IndexUp_4d, IndexDn_4d, A1)

  k=3
  A3 = ExpandOnClm(k, theta, phi, -I*(2*k+1)*Rj3R)
  T3 = NewOperator("CF", NFermions, IndexUp_4f, IndexDn_4f,
                                    IndexUp_4d, IndexDn_4d, A3)

  k=5
  A5 = ExpandOnClm(k, theta, phi, I*(2*k+1)*Rj5R)
  T5 = NewOperator("CF", NFermions, IndexUp_4f, IndexDn_4f,
                                    IndexUp_4d, IndexDn_4d, A5)

  T = T1+T3+T5
  return T, T1, T3, T5
end
```

With all these function the NIXS spectra can be calculated specifying the module and the direction of the exchanged momentum $\mathbf{q}$

```
-- q in units per a0 (multiply by a0 the value you want to have in A)
-- some constants
a0= 0.52917721092
q = 9.8 * a0

-- define the direction of the exchanged momentum q
qtheta = 0  -- pi/2  for q100   -- pi/2  for q110
qphi   = 0  -- 0                -- pi/4
T_q001_all, T_q001_k1, T_q001_k3, T_q001_k5 = TnIXS_pd(q, qtheta, qphi)

nIXS_Spectra = CreateSpectra(H_f, {Tq001_all,  T_q001_k1, T_q001_k3, T_q001_k5},
                 Psi_i, {{"Emin",-30}, {"Emax",30}, {"NE",10000}, {"Gamma", 0.1}})
```

Gamma is the Lorentzian broadening expressed in eV. An additional Gaussian broadening is usually applied to the simulated spectra in order to reproduce the experimental broadening.

5.2 Atomic multiplet simulations of $4f$ XRS $N_{4,5}$ edges

The calculations presented in this thesis are based on an atomic model of the ion under investigation. It can be successfully applied in cases in which the atomic model is a

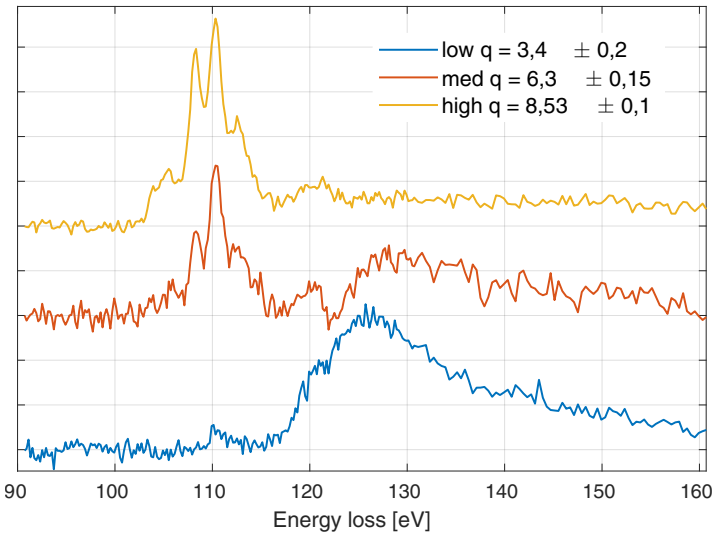

Figure 5.2: XRS experimental spectra of the $N_{4,5}$ edge of Ce in $CeRh_2As_2$, measured at $T = 295\,\mathrm{K}$. At low q the spectrum is dominated by a broad dipole feature peaked at $126\,\mathrm{eV}$. This feature gradually disappears going from the low to the high q spectrum. At high q the peaks in the energy range $100\,\mathrm{eV}$-$115\,\mathrm{eV}$ dominate the spectrum. They are separated in energy from the broad dipole peak.

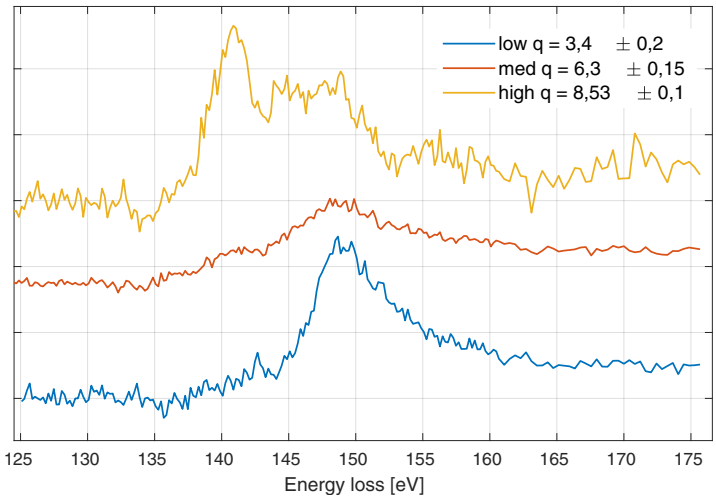

Figure 5.3: XRS experimental spectra of the $N_{4,5}$ edge of Gd in $GdRh_2Si_2$ measured at $T = 295\,\mathrm{K}$. At low q a broad feature peaked at $148\,\mathrm{eV}$ dominates. At high q a sharp peak appears at $141\,\mathrm{eV}$ and dominates the spectrum.

good approximation of the behaviour of the atom in the solid. For the highly localized $4f$ shell this picture proved to be a good one.

In the following the XRS data acquired with the spectrometer at ID20 of the ESRF are presented. The samples are described in more detail in chapter 6.1. They are ternary compounds of the family 122 containing the rare-earths: Ce, Gd and Ho. In particular the samples are: $CeRh_2As_2$, $GdRh_2Si_2$ and $HoRh_2Si_2$. In these materials the rare-earth elements are found as trivalent ions Ce^{3+}, Gd^{3+} and Ho^{3+}, with electronic configuration $4f^1$, $4f^7$ and $4f^{10}$, respectively. The spectra were acquired with three different crystal analyzer modules composed of 12 crystal analyzers each. The measurements were performed with an incoming energy $E_0 = 9.7\,\mathrm{keV}$. The three modules where placed at angles such that the exchanged momenta were about 3.4Å^{-1}, 6.3Å^{-1} and 8.5Å^{-1}. The measurements were performed at ambient temperature ($T = 295\,\mathrm{K}$). After the subtraction of the Compton profile, as described in 4.1.4, the edge step height has been set equal to 1 for all the spectra.

The experimental XRS spectra of the $N_{4,5}$ edge of Ce, Gd and Ho are shown respectively in figure 5.2, 5.3 and 5.4.

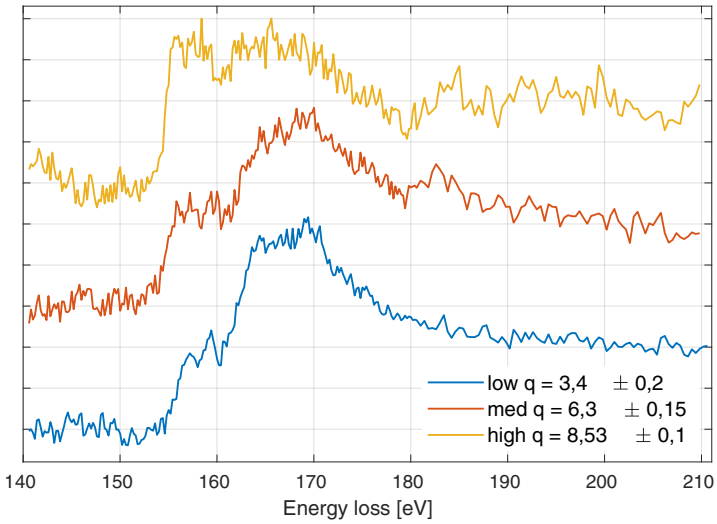

Figure 5.4: XRS experimental spectra of the $N_{4,5}$ edge of Ho in $HoRh_2Si_2$ measured at $T = 295\,\mathrm{K}$. A broad feature is still present in the high q spectrum. The peaks in the energy range $155\,\mathrm{eV}$-$160\,\mathrm{eV}$ gradually increase in intensity as q increases.

At low exchanged momentum q all the experimental spectra show a peak with an asymmetric broadening of about $10\,\mathrm{eV} - 15\,\mathrm{eV}$. This feature arises from the fact that for the shallow core transition $4d \rightarrow 4f$ the core-valence multiplet spread is $\approx 20\,\mathrm{eV} - 25\,\mathrm{eV}$, as estimable from the experimental data. Often this value is larger than the hole-electron attractive potential. This pushes the higher lying levels of the excited final state configuration $4d^9 4f^2$ at higher energies, in resonance with the conduction band [70]. These transitions do not correspond to transitions into excitonic states, but rather to transitions into non bounded states hybridized with conduction band states. This means that these virtual-bounded Fano-resonances cannot be described in terms of local atomic models. The peaks at the lowest energy loss values are instead sharper than this feature. The intensity at low energy loss corresponds to transitions into states with a higher binding energy. These states are far in energy from the conduction band states. This means that these states are not hybridized and correspond to transitions into excitonic bounded states. These states are well described by an atomic model. The broad features are very often dipole allowed while the sharp peaks at lower energy loss correspond very often to higher order transitions.

The experimental spectra are dominated at low q by dipole transitions that gradually reduce in intensity as the exchanged momentum q increases. At high q some sharp peaks start to dominate the spectra. This is most clear for Ce in figure 5.2. At low exchanged momentum $q = 3.4$Å a broad feature peaked at $126\,\mathrm{eV}$ dominates. Instead, in the Ce spectrum measured with $q = 8.5$Å some peaks in the energy range $100\,\mathrm{eV}$-$115\,\mathrm{eV}$ are the most intense. These are due to higher order transitions (octupole and triakontadipole) which contribute most at high exchanged momentum, as pointed out discussing the radial integrals in figure 3.3.

In figure 5.5, 5.6 and 5.7 the XRS spectra calculations performed on Ce^{3+}, Gd^{3+} and Ho^{3+}, respectively, are shown. These calculations were performed using a script based on the code presented on chapter 5.1. The atomic multiplet simulations of the XRS spectra were calculated as a function of the exchanged momentum q. The colored areas correspond to the different contributions from the different transition orders: in blue for $k = 1$ (dipole), in green $k = 3$ (octupole) and in red $k = 5$ (triakontadipole). The experimental data acquired with $q = 3.4\text{Å}^{-1}$, 6.3Å^{-1} and 8.5Å^{-1} are superimposed,

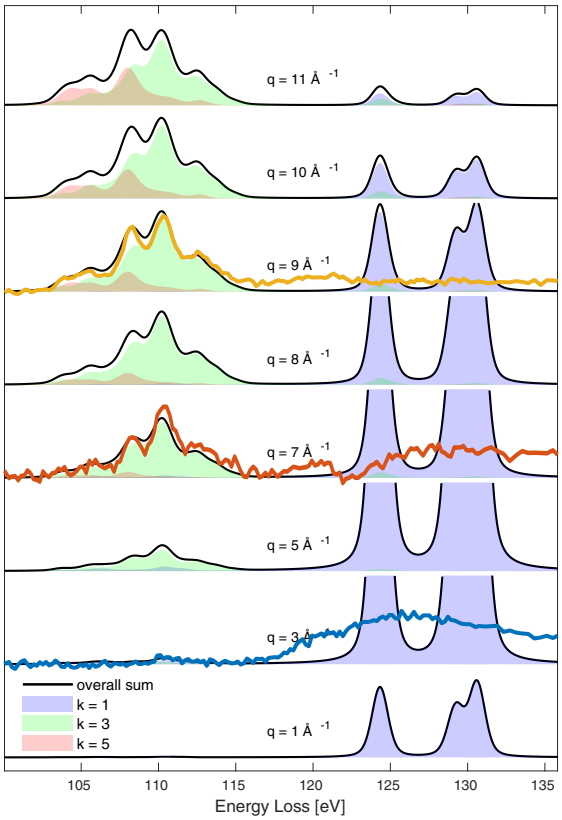

Figure 5.5: Dependence of XRS $N_{4,5}$ edge simulations of Ce^{3+} on the modulus of the exchanged momentum. The shaded areas correspond to the different transition orders: $k = 1$ dipole, $k = 3$ octupole and $k = 5$ triakontadipole. The experimental data of $CeRh_2As_2$ are superimposed with arbitrary normalization. Simulated spectra are shifted positively by 115 eV. The simulations in the energy range 120 eV-135 eV do not predict the experimental data. The simulations in the energy range 100 eV-120 eV instead predict the correct shape of the peaks. The simulated dependence on the exchanged momentum q predicts correctly the experimental dependence.

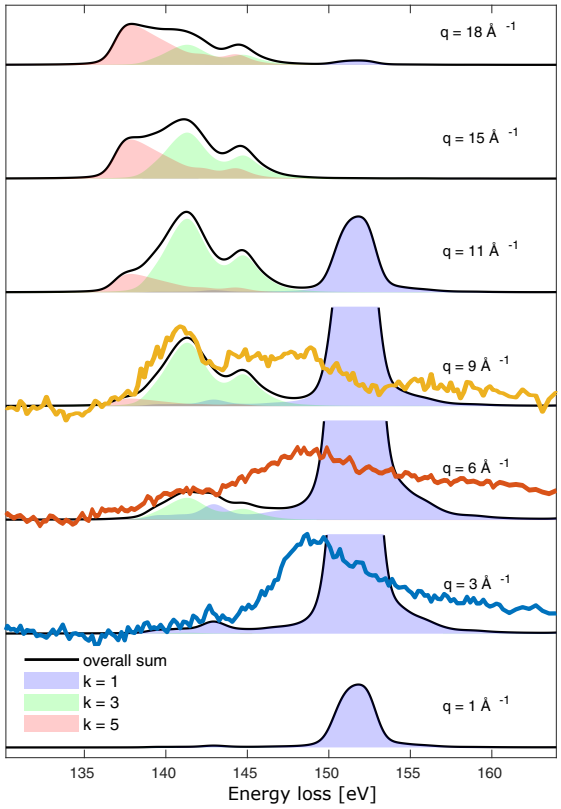

Figure 5.6: Dependence of XRS $N_{4,5}$ edge simulations of Gd^{3+} on the modulus of the exchanged momentum. The shaded areas correspond to the different transition orders: $k = 1$ dipole, $k = 3$ octupole and $k = 5$ triakontadipole. The experimental data of $GdRh_2Si_2$ are superimposed with arbitrary normalization. Simulated spectra are shifted positively by 145 eV. The dipolar peak at 152 eV does not reproduce the experimental spectra. Also the position is not reproduced. The shape of the peaks in the energy range 135 eV-146 eV instead is reproduced.

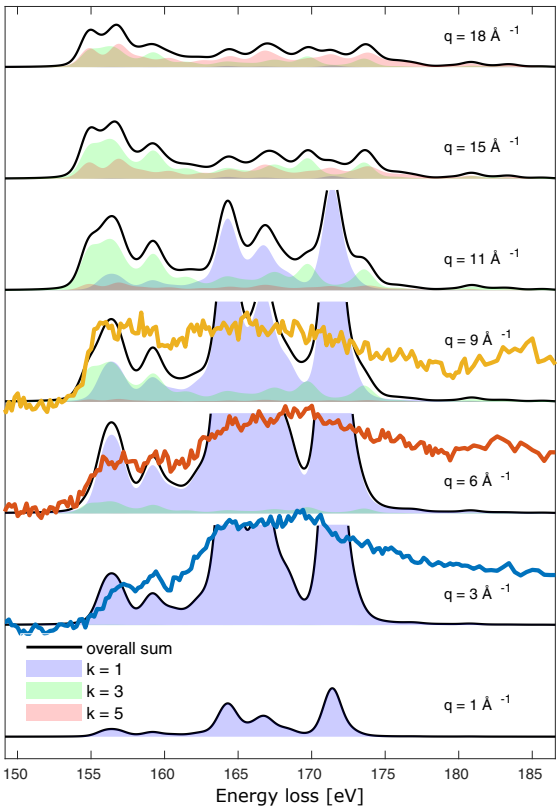

Figure 5.7: Dependence of XRS $N_{4,5}$ edge simulations of Ho^{3+} on the modulus of the exchanged momentum. The shaded areas correspond to the different transition orders: $k = 1$ dipole, $k = 3$ octupole and $k = 5$ triakontadipole. The experimental data of $HoRh_2Si_2$ are superimposed with arbitrary normalization. Simulated spectra are shifted positively by $164\,\mathrm{eV}$. The peaks in the energy range $161\,\mathrm{eV}$-$175\,\mathrm{eV}$ are not reproduced by the simulations. The shape of the peaks in the energy range $154\,\mathrm{eV}$-$161\,\mathrm{eV}$ instead is reproduced.

with arbitrary normalization, for comparison.

The simulations predict sharp and intense dipole peaks, which dominates the spectra at low q. The simulations clearly show how the higher order transitions gradually start to dominate the spectra as the exchanged momentum q grows. The dependence on the exchanged momentum q reproduces the experimental one. The value of q that reproduces best the experimental data is usually higher than the experimental one. This is due to the fact that the calculated atomic radial wave functions have to be scaled with respect to the Hartree-Fock one.

The simulated spectra have to be shifted because the simulations do not predict the position of the edge. The simulated spectra has been positively shifted by $115\,\mathrm{eV}$ in the case of Ce, $145\,\mathrm{eV}$ for Gd and $164\,\mathrm{eV}$ for Ho.

Clearly, the atomic simulations cannot predict the broad features. They could be reproduced including local correlations as well as the full (dynamical) meanfield approximated band structure in the model, as explained in Ref. [71]. Likewise, the simulations cannot reproduce the edge step that arises from transitions into continuum states. Instead, the peaks at lower energy loss are well reproduced. In fact these spectral features correspond to bounded excitonic states that can be successfully modeled with atomic multiplet theory.

The simulations predict that the multipole transition for Ce give rise to features clearly detached from the dipole transition peaks. This is still true for Gd, but is not true for Ho, where the contributions from the higher order transitions are at same energy position as those of the dipole transitions. The position of the peaks at high energy loss is not reliable because in that energy region the atomic model fails. The position is

usually overestimated.

The broadening of the features depends on the energy position of the final level and not only on the dipolar or multipolar character of the transition. A justification for this statement can be the presence of two sharp peaks at 158 and 159 eV in the experimental spectrum of Ho. The simulations predict that these peaks are, at low exchanged momentum, predominantly of dipolar character.

CHAPTER 6

Determination of $CeRh_2As_2$ crystal field scheme by means of XAS and XRS natural LD

In this chapter, the experimental results of the XAS and XRS natural linear dichroism experiments of the compound $CeRh_2As_2$ are presented. First, in section 6.1, the peculiarity of its crystal structure is described, comparing it with similar samples. Then the experimental data are described in 6.2. Finally it is shown, in chapter 6.3, how it is possible to extract information about the crystal field levels scheme. This means determining the order of the three doublets in which the multiplet $^2F_{5/2}$ is split by the crystal field, the values of the splittings and the mixing parameter α. This will be accomplished through the comparison of the experimental spectra with the spectra simulated using atomic multiplet theory.

6.1 $CeRh_2As_2$: heavy fermion system of $CaBe_2Ge_2$ structure type

The materials discussed in this thesis are 122 ternary alloys characterized in general by a composition RET_2X_2. RE represents a rare earth ion (Ce, Gd, Ho, ...), T indicates $3d$, $4d$ and $5d$ transition metals (Cu, Ru, Rh, Ag, Ir, ...) and X represents *p*-elements (Si, P, Ge, As, ...). These compounds very often crystallize in a so-called $ThCr_2Si_2$ (space group $I4/mmm$) body-centered tetragonal structure type. This is the case for $GdRh_2Si_2$ and $HoRh_2Si_2$, whose crystal structure is depicted in figure 6.1. In this crystal structure, the bonds occur mainly between the transition metal and the non metal element, which are distant about 2.5Å from each other. They form a framework in which the rare earth elements are centered and separated by about 3.1Å from the nearest neighbouring atoms. The rare earth is immersed in a tetragonal D_{4h} environment. Rhodium forms tetrahedral bonds with its four Si nearest neighbours. Silicon instead forms pyramidal bonds with the four nearest Rh and a Si atom at the vertex. This is

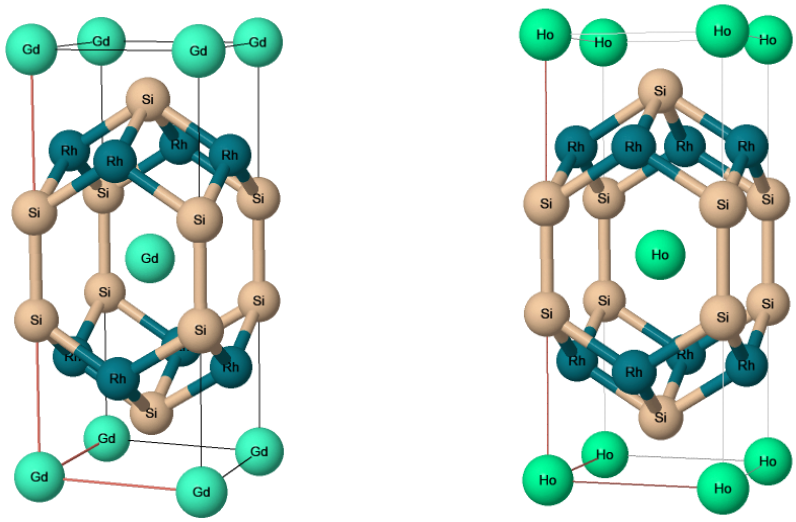

(a) **(b)**

Figure 6.1: Crystal structure of the ternary 122 compounds (a) $GdRh_2Si_2$ and (b) $HoRh_2Si_2$. They crystallize in a $ThCr_2Si_2$-type body-centered tetragonal crystal structure of space group $I4/mmm$. The length of the drawn bonds is 2.5Å, the distance of the RE from the nearest neighbours is about 3.1Å. Lattice parameters for $GdRh_2Si_2$ are: $a = b = 4.045$Å$, c = 9.980$Å. Lattice parameters for $HoRh_2Si_2$ are: $a = b = 4.084$Å$, c = 10.009$Å. Crystals structures drawn and data taken from Ref. [72].

general for all the compounds with $ThCr_2Si_2$ structure type and can be summarized as: $RE^{tet}T^{tet}X^{py}X^{py}$.

The ternary 122 compounds can also crystallize in a primitive tetragonal structure of the $CaBe_2Ge_2$-type (space group $P4/nmm$ 129). This is the case for $CeRh_2As_2$. In figure 6.2.(a) the crystal structure of the unit cell is depicted. Also, in this structure the bonds are formed mainly between the transition metal Rh and the p-element As with a bond length of about 2.6Å. However, in this case the two Rh and the two As ions are placed in two non-equivalent lattice sites. In figure 6.2.(b) some polyhedra centered on the atoms are depicted. The nearest neighbors of the atom are placed at the vertices of the polyhedra. In this crystal structure, one of the two Rh (denoted as Rh1 in the figure) sits in a tetrahedral environment, and the other (Rh2) in a pyramidal site. The same is valid for As. This is valid in general for all the compounds with $CaBa_2Ge_2$ structure type and can be summarized as: $RE^{tet}T^{py}X^{tet}X^{py}$. Including also the neighbouring unit cells along *a* and *b* as in figure 6.2.(c), it is possible to see that also in this structure Ce sits in the center of the framework formed by the other atoms to which it is separated by about 3.3Å.

6.1.1 Ce^{3+} locally non-centrosymmetric environment

Figure 6.3 shows the 16 nearest neighbours of Ce. It is possible to see that the local environment of Ce is not invariant under the inversion operation i and is not invariant under the operations that involve a mirror operation for a plane parallel to the ab plane. This means that the local point group symmetry of Ce is C_{4v}, a subgroup of the symmetry group D_{4h} of the crystal. The two Ce ions in the unit cell have this equivalent

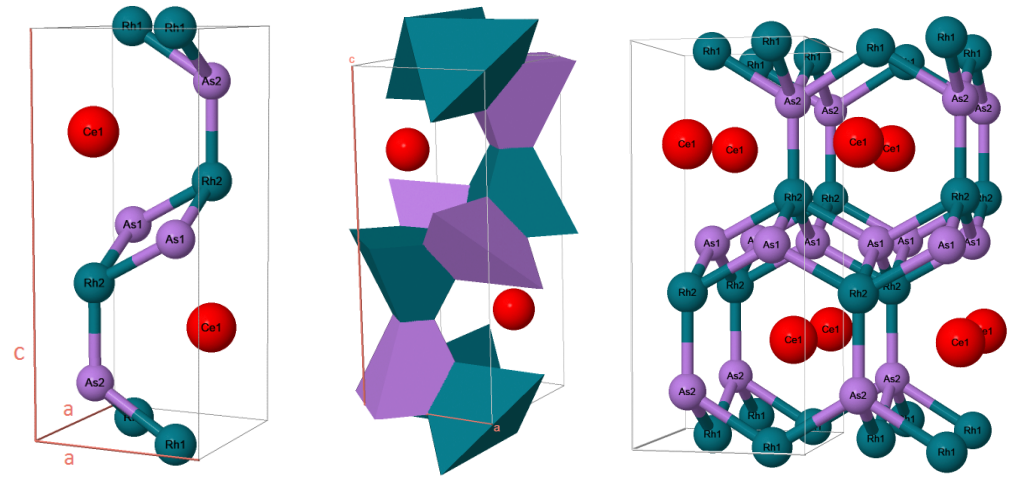

Figure 6.2: Crystal structure of the ternary $CaBe_2Ge_2$-type compound $CeRh_2As_2$. The lattice parameters are $a = b = 4.283$Å$, c = 9.850$Å. The drawn bonds are 2.6Å long. Ce is 3.3Å far from the nearest neighbours. Two Ce atoms are separated by a minimum distance of 4.3Å. (a) Structure of the unit cell. Rh1 sits in an atomic site nonequivalent to the one of Rh2. The same is valid for As. (b) The polyhedra are centered on the Rh and As atoms. At the vertices of the polyhedra are positioned the nearest neighbours. Rh1 and As1 see a tetragonal environment, while Rh2 and As2 see a pyramidal environment. (c) Two units cells along the equivalent directions a and b are drawn. Ce is at the center of a framework formed by the other elements. Data taken from Ref. [73].

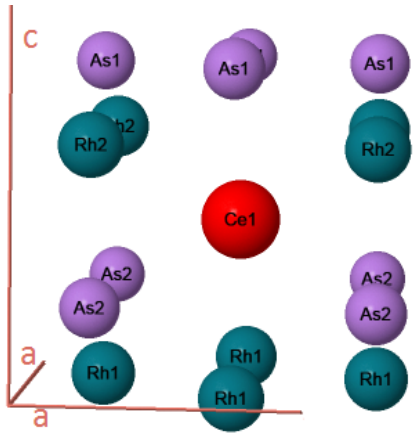

Figure 6.3: The 16 nearest neighbours of the Ce in $CeRh_2As_2$. With respect to a tetragonal D_{4h} symmetry, the local environment of Ce lacks the inversion symmetry and the mirror operations with respect planes perpendicular to the principal axis, parallel to c. The local point group symmetry is C_{4v}.

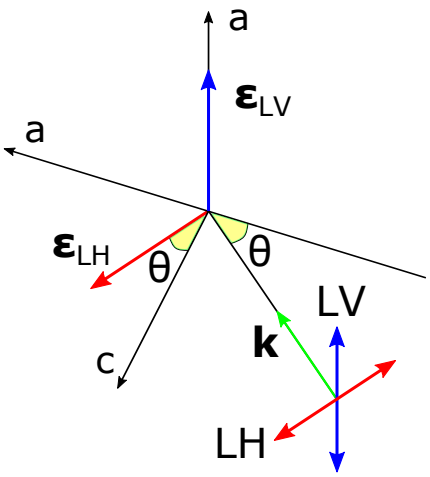

Figure 6.4: Definition of the geometry used in the XAS experiments. The axes a and c refer to the crystallographic axes. The surface of the sample is perpendicular to the c axis. An x-ray with wave vector $\mathbf{k}$ is impinging on the sample with an angle of incidence θ with respect to the surface. The polarization vector ϵ can be linearly polarized on the vertical plane (LV) thus lying on the aa plane. It can also be linearly polarized on the horizontal plane (LH), thus having a component along the c axis: $\epsilon_c = \cos\theta$.

local point group symmetry, but their environment is specular: with reference to figure 6.2.(a), the planes formed by the Rh2 and As1 atoms are placed in a positive direction along c for the lower Ce ion, while with respect to the upper Ce ion, the same planes are placed along the negative c direction.

The C_{4v} symmetry of Ce cannot be modeled by the effective crystal field model as explained in chapter 2.1. The V_{CEF} used to model the two Ce ions in the calculations has D_{4h} symmetry and is the same for both the ion sites. This means that in the calculations it is sufficient to consider just one of the two ions.

6.2 Experimental spectra

6.2.1 XAS TEY LD experimental data

The XAS experimental spectra at the $M_{4,5}$ edges of $CeRh_2As_2$ were measured at ID32 of ESRF. The total electron yield (TEY) technique was used. The geometry of the experiment was defined as in figure 6.4. The axes refer to the crystallographic axes and the surface of the sample is perpendicular to the c axis. The polarization vector $\boldsymbol{\epsilon}$ can be linearly polarized along the vertical direction (LV) which means that it lies in the plane formed by the two equivalent crystallographic directions a and b, both labelled as a. The polarization can also be linearly polarized in the horizontal plane (LH), which means that the polarization vector has a component along the c direction equal to $\epsilon_c = \cos\theta$. Vertical and horizontal directions are defined with respect to the plane of the storage ring.

The experiment aimed at measuring the difference between the x-ray absorption for a polarization lying in the plane ab of the crystal and the x-ray absorption for a polarization lying along the out of plane direction c. The incident angle was $\theta = 30°$. The experimental data shown in the following are treated as explained in chapter 4.2.2. The XAS spectra obtained are shown in figure 6.5. The natural linear dichroism (LD) is plotted in green as the difference between the spectra acquired with LH polarization (red), with an incident angle $\theta = 30°$, and the spectra acquired with LV polarization (blue): LD=LH-LV. The spectra in 6.5.(a) were acquired at ambient temperature $T_{amb} \approx 300\,\mathrm{K}$. The spectra in 6.5.(b) instead were acquired at $25\,\mathrm{K}$ in order to ther-

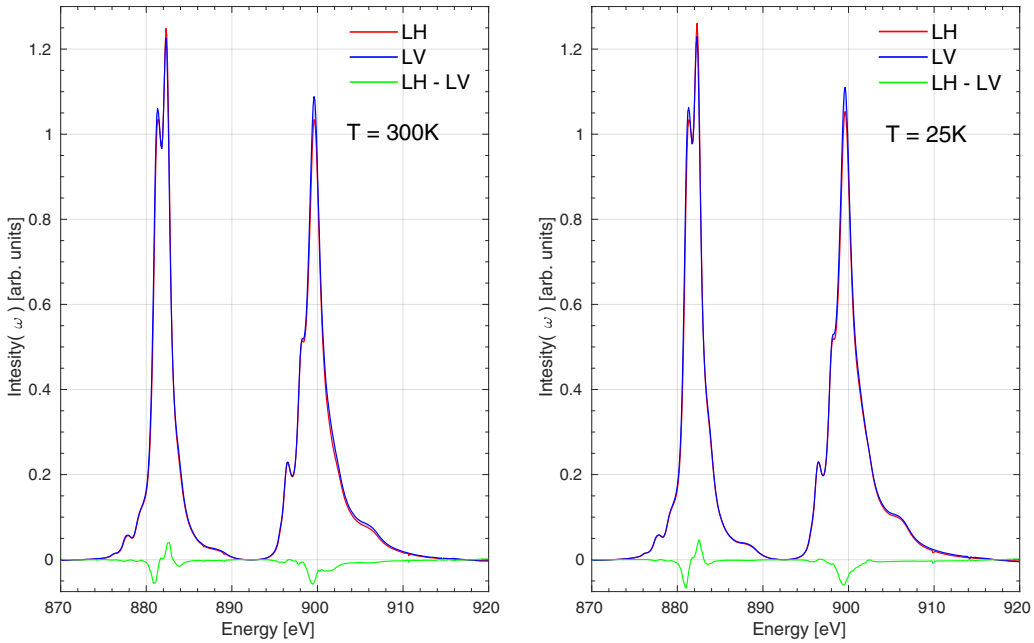

(a) Spectra acquired at T=300K

(b) Spectra acquired at T=25K

Figure 6.5: Experimental XAS TEY spectra of Ce $M_{4,5}$ edge in $CeRh_2As_2$ acquired at ID32 of the ESRF. The linear dichroism (LD) is plotted in green, the difference between the red spectra, acquired with LH polarization ($\theta = 30°$), and the blue spectra acquired with LV polarization. The spectra in (a) are acquired at ambient temperature 300 K. The spectra in (b) are acquired at a temperature of 25 K.

mally populate mainly the lowest energy levels.

The LD signal is $\approx 3\%$ of the XAS intensity at its maximum. It shows a small variation with the temperature.

$4f_0$ contribution

The main difference between the LD(300 K) measured at ambient temperature and the LD(25 K) measured at low temperature can be pointed out comparing the spectra acquired with the same polarization at the two temperatures. In figure 6.6 the spectra acquired with the same linear polarization are compared: in (a) with LV polarization, in (b) with LH polarization. The main difference, which is present in both figures 6.6.(a) and (b), is the increase of the intensity of the peaks labeled as $4f^0$ moving from 300 K to 25 K. These peaks are present due to the hybridization of the $4f$ electron with the conduction electrons as a consequence of the Kondo effect [74]. In this material the interaction has an energy of about $T_K \approx 30$ K (private communications). If the Kondo interaction prevails the f electron becomes delocalized increasing the weight of the $4f_0$ configuration. As the temperature grows, instead, and the thermal fluctuations overcome the Kondo interaction, the $4f$ electrons become more and more localized.

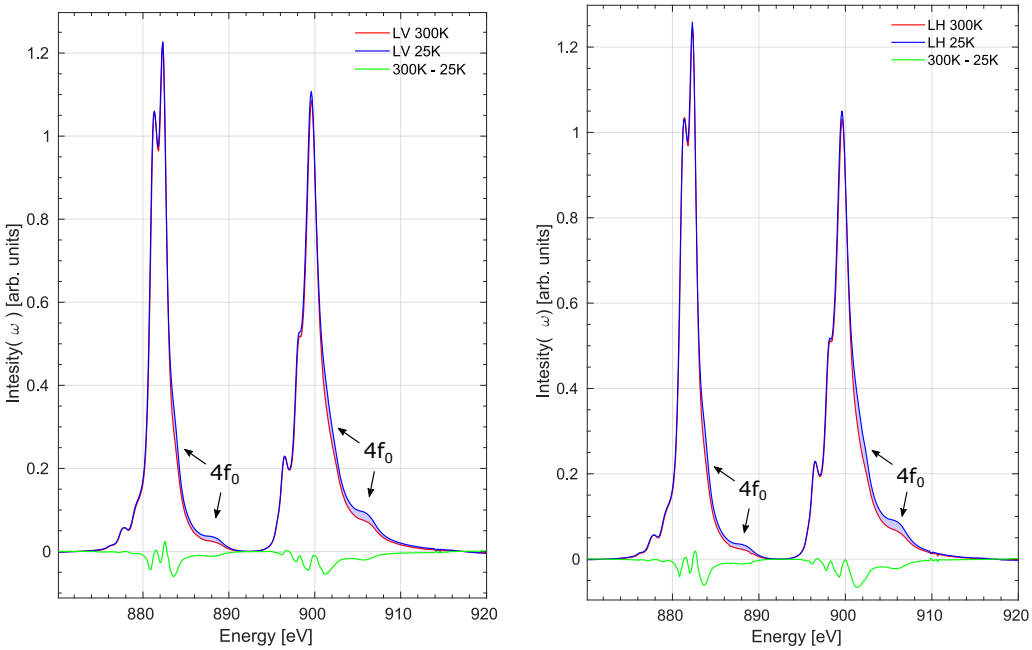

(a) LV polarization.

(b) LH polarization.

Figure 6.6: Comparison between the spectra acquired at 300 K (red) and 25 K (blue) separately for the two polarizations: in (a) for LV polarization, in (b) for LH polarization with incident angle $\theta = 30°$. In both (a) and (b) there are four peaks that arise from the contribution of the Ce^{4+} with configuration $4f^0$. The intensity of these peaks clearly increase at low temperature. This mixed valence state is a consequence of the Kondo interaction.

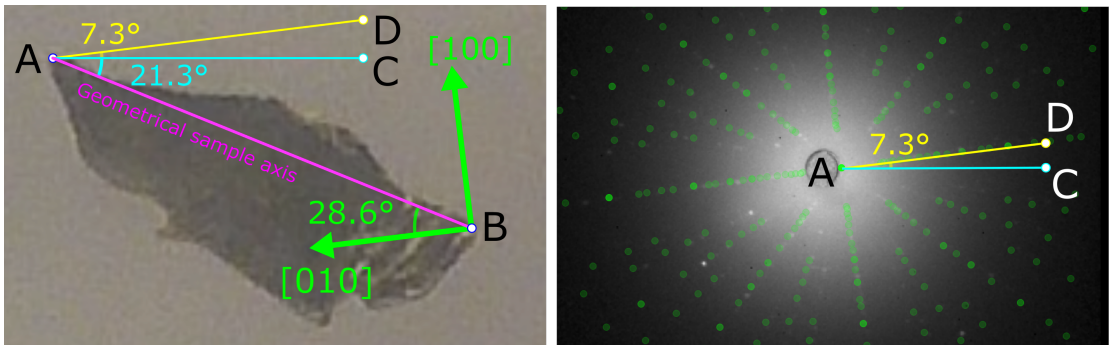

Figure 6.7: Determination of the crystal orientation through Laue diffraction. The segment $\overline{AC}$ is parallel to the horizontal plane of the Laue diffraction camera. The Laue diffraction pattern obtained with this orientation lies along the segment $\overline{AD}$ that forms an angle of 7.3° with $\overline{AC}$. Defining a clearly identifiable geometrical sample axis $\overline{AB}$ as in the left figure it is found that the equivalent directions [100] and [010] form an angle of 28.6° with $\overline{AB}$ as in figure.

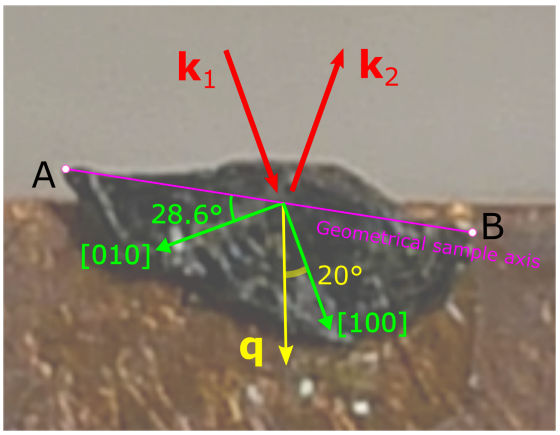

Figure 6.8: Picture of the sample mounted on the sample holder. $\mathbf{k}_1$ is the direction of the incoming x-ray beam, $\mathbf{k}_2$ is the direction of the scattered x-ray beam. The exchanged momentum is determined to form an angle of 20° with respect to the crystallographic direction $[100]$.

6.2.2 XRS LD experimental data

Laue diffraction

As explained in chapter 3.3.3, XAS is not sensitive to symmetries lower than 2-fold. As a consequence, the spectra are not sensitive to the direction of the polarization in the plane ab. Instead, XRS is sensitive both to the out of plane natural linear dichroism and to the *in plane* natural dichroism. This means that the direction of the exchanged momentum in the plane has to be known. The orientation of the crystallographic axes of the sample was obtained through x-ray Laue diffraction. A white beam of x-rays impinges on the fixed sample. For highly absorbing materials the back reflection method is used, in which the detector is placed between the source and the crystal. Since a white beam is used, Bragg's law is satisfied for several crystal planes at the same time.

In the case of the $CeRh_2As_2$ single crystal shown in 6.7 the flat surface is perpendicular to the c axis. Defining an easily identifiable geometrical sample axis, going through points A and B, it was determined that the crystallographic direction $[100]$ (or $[010]$ equivalently) forms an angle of $28.6°$ with respect to it. The sample was mounted in the sample holder as in figure 6.8. The measurement was performed with the exchanged momentum q forming an angle of $20°$ with respect to the $[100]$ crystallographic direction.

XRS data

XRS data on $CeRh_2AS_2$ were collected at the ID20 of the ESRF. The spectra were acquired with a single crystal analyzer module in the horizontal plane. The signal coming from 12 crystal analyzers was summed up. The measurements were performed with an incoming energy $E_0 = 9.7\,\mathrm{keV}$. The module was placed at an angle of such that the exchanged momentum was about 9.3Å^{-1}. The measurements were performed with the sample kept inside a dynaflow cryostat that kept the sample at a temperature of $10\,\mathrm{K}$. Two sets of measurements were performed in order to measure the natural out-of-plane dichroism. A measurement was performed with the exchanged momentum vector parallel to the c axis ($[001]$ crystallographic direction) and a second measurement was performed with the exchanged momentum forming an angle of $20°$ with the $[100]$ crystallographic direction. The acquired data were treated as explained in chapter 4.1.4. After the subtraction of the Compton profile each spectrum was divided by the value

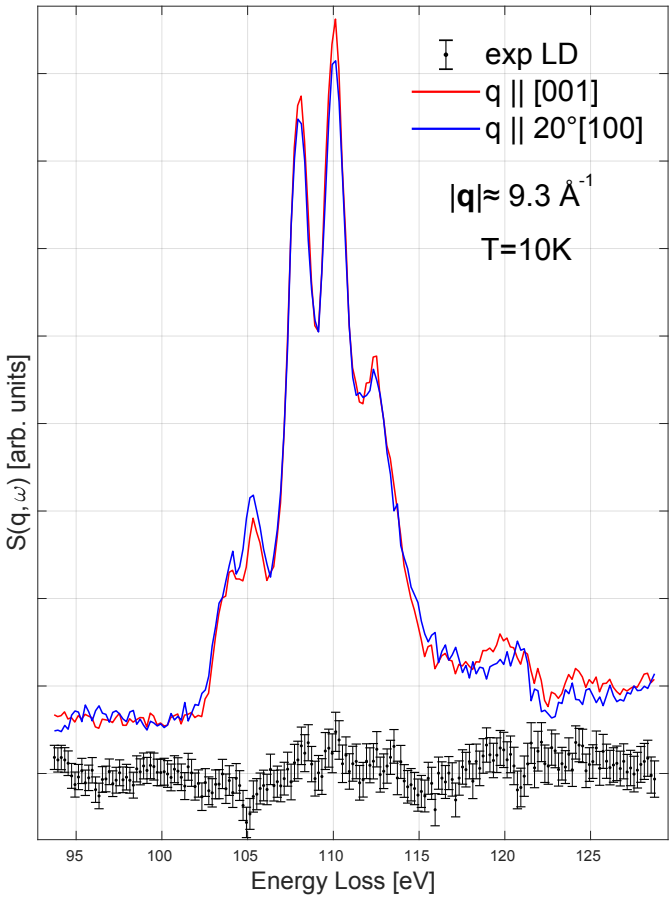

Figure 6.9: XRS spectra of the $N_{4,5}$ edge of Ce in $CeRh_2As_2$. Experimental data acquired at ID20 of the ESRF. Acquisition performed at $T = 10\,\mathrm{K}$. The spectra were recorded with a modulus of the exchanged momentum of about $9.3\mathring{\mathrm{A}}^{-1}$. The spectra were measured with $\mathbf{q}$ oriented in two directions with respect to the crystallographic axes: with $\boldsymbol{q}$ along the c direction [001] and with $\boldsymbol{q}$ at 20° with respect to the direction [100] (or [010] equivalently). Spectra normalized by the value of their integral over the range $100\,\mathrm{eV} - 116\,\mathrm{eV}$.

of its integral calculated in the energy range $100\,\mathrm{eV}$-$116\,\mathrm{eV}$. The data are shown in figure 6.9. The experimental LD, given by the difference $\mathrm{LD} = S(q \parallel [001]) - S(q \parallel 20°[100])$, is plotted as black error bars. The length of the error bar is the standard deviation.

6.3 Crystal field levels scheme

In the following is shown how to determine a set of possible values for the crystal field splitting of the $4f^1$ levels of Ce^{3+} in $CeRh_2As_2$. The determination will be achieved through the comparison of the XAS and XRS experimental data with the atomic multiplets simulations. A set of possible crystal filed schemes is determined.

6.3.1 Restriction of the possible CF configurations

From the RIXS measurements, shown in appendix A, performed on $CeRh_2As_2$, it is possible to put an upper bound to the splitting between the crystal field levels. It is found to be lower than $\Delta E_{CF}^{max} < 50\,\mathrm{meV}$. A lower bound for the energy level splitting can be found looking at how the experimental XAS LD of figure 6.5 changes with temperature going from $25\,\mathrm{K}$ to $300\,\mathrm{K}$. If all the three lowest doublets can be populated with the same probability, the resulting state would have spherical symmetry and would show no dichroism. Since the variation of the experimental dichroism with temperature is very small, it is possible to guess that the CF configuration contains at least one

level which is far from the ground state level by at least $7.5\,\mathrm{meV}$. With this splitting it is guaranteed that the highest level has a Boltzmann weight at $300\,\mathrm{K}$ lower than $0.75 \approx \exp(-7.5\,\mathrm{meV}/(k_B 300\,\mathrm{K}))$.

The simulations presented in the following were performed using the following parameters for the XAS $M_{4,5}$ edge: scal_3d4f= 0.825, scal_4f4f= 0.56, scal_zeta_4f= 0.82 and scal_zeta_3d= 0.963. For the XRS $N_{4,5}$ edge instead were used: scal_4d4f= 0.83, scal_4f4f= 0.7, scal_zeta_4f= 0.82 and scal_zeta_4d= 0.97. The name refers to the variables used in the code presented in chapter 5.1. They were chosen in order to best reproduce the shape of the experimental spectra as shown in detail in appendix A.

Is it possible to exclude some CF configurations just by looking at the simulated linear dichroism LD for pure $|J_z\rangle$ states. The simulations of respectively the XAS and XRS spectra performed on Ce^{3+} in absence of a crystal field Hamiltonian are shown in figures 6.10 and 6.11. In this case all the states are cylindrically symmetric around the c axis and are all degenerate in energy. These states show no natural linear dichroism for *in plane* directions both in the XAS and the XRS spectra. This means that the spectrum is the same for all the directions in the plane ab of the polarization in XAS, and of the exchanged momentum in XRS. Instead, they show natural linear dichroism for *out of plane* directions. The difference between the intensity of the spectrum obtained with the polarization in the plane ab $I(\epsilon \parallel ab)$ and the spectrum obtained with the polarization along the c axis $I(\epsilon \parallel c)$ is clearly distinguishable from state to state.

Including also a tetragonal D_{4h} crystal field in the simulations the states $|\pm 5/2\rangle$ mix with the states $|\mp 3/2\rangle$ while the states $|\pm 1/2\rangle$ remain almost pure states. The dependence of the state $\Gamma_7^1 = \alpha\,|\pm 5/2\rangle + \sqrt{1-\alpha^2}\,|\mp 3/2\rangle$ on the value of the mixing parameter α is shown in figure 6.12. The dependence of the XAS $M_{4,5}$ edge spectra simulated with linear polarization in the vertical plane (LV) in blue, and with the linear polarization in the horizontal plane (LH) at an incident angle of $\theta = 30°$ is shown in part (a) of the same figure. In part (b) the dependence of the XRS simulations on α is shown. The simulations were performed with $\mathbf{q} \parallel [001]$ (in red), with $\mathbf{q} \parallel [100]$ (in blue) and with $\mathbf{q} \parallel 20°[100]$ (in green) as in the experiments. In part (b) also the density of the state Γ_7^1 is plotted.

In figure 6.13 are compared the XAS and XRS LD simulations to the experimental LD, with focus on the relevant features of the M_5 and M_4 edges, for the representative crystal field levels schemes sketched in the figure. The XAS dichroism show less features with respect to the XRS dichroism, and the comparison is more straightforward. Note that all the simulated dichroisms cross the zero at the same energy. This justifies the choice for the normalization adopted for the XAS spectra explained in section 4.2.2. The experimental spectra are normalized so that they show a zero in the dichroism at the same energy of the simulated dichroism. The following configurations sketched in the figure can be excluded:

- ☒ (a) $\Gamma_7^1 \ll \Gamma_7^2 \approx \Gamma_6$ with $\alpha \gtrsim 0.3$ gives a dichroism of opposite sign with respect to the experimental XAS LD.
- ☒ (b) $\Gamma_7^1 \ll \Gamma_7^2 \approx \Gamma_6$ with $\alpha \approx 0$ gives the correct sign but the relative intensity of the dichroism is too high.
- ☒ (c) $\Gamma_6 \ll \Gamma_7^1 \approx \Gamma_7^2 \;\; \forall\alpha$ gives a too high XAS LD but with correct sign and XRS LD shows big discrepancies.

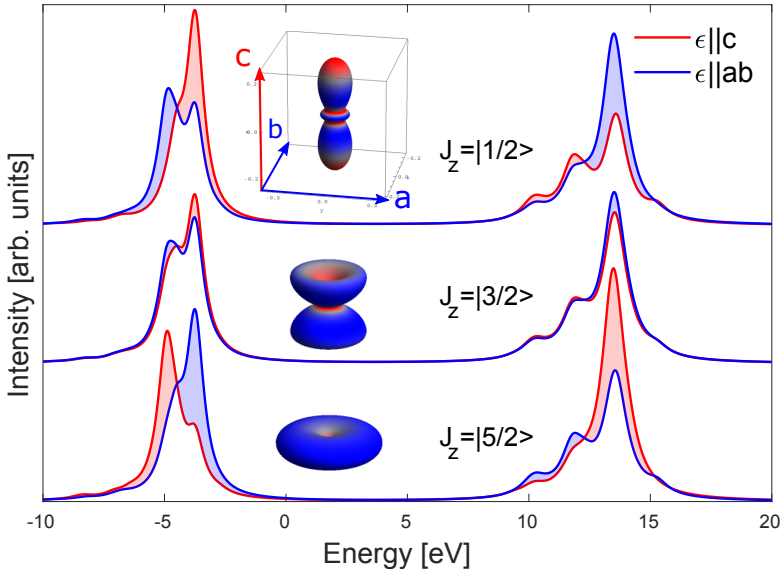

Figure 6.10: Atomic simulations of the XAS $M_{4,5}$ edge of Ce^{3+} calculated for pure $|J_z\rangle$ states. The states are cylindrically symmetric around the c axis and the directions a and b are equivalent. In red the intensity of the spectrum for $\epsilon \parallel c$. In blue the intensity for $\epsilon \parallel ab$. The absorption spectra is the same for all the polarization lying on the plane ab. Instead pure J_z states show a marked natural out of plane linear dichroism which makes the three states clearly distinguishable. The sum of the three states gives a spherically symmetric state which shows no dichroism.

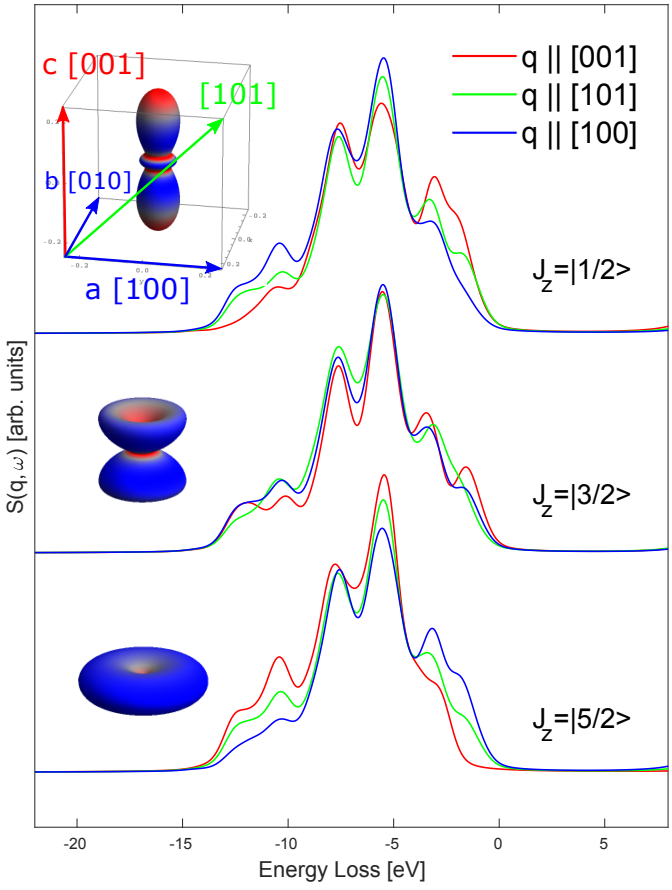

Figure 6.11: Atomic simulations of the XRS $N_{4,5}$ edge of Ce^{3+} calculated for the pure $|J_z\rangle$ states. The exchanged momentum is $q = 9.3\text{Å}^{-1}$. For pure J_z states, that are cylindrically symmetric around the c axis, all the directions in the plane ab are equivalent. Instead they show a characteristic out of plane dichroism. Note that the spectra simulated for $q \parallel [101]$ are not just the linear combination of the spectra simulated for the directions $q \parallel [100]$ and $q \parallel [001]$.

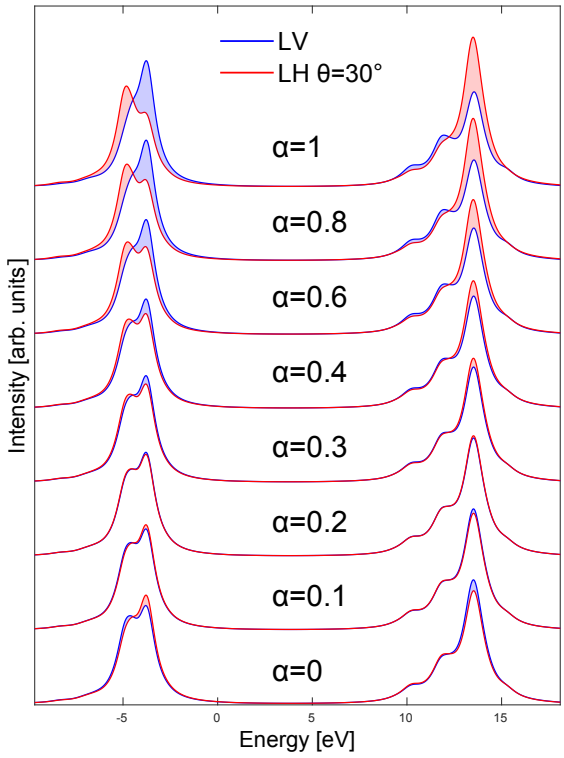

(a) XAS $M_{4,5}$ edges.

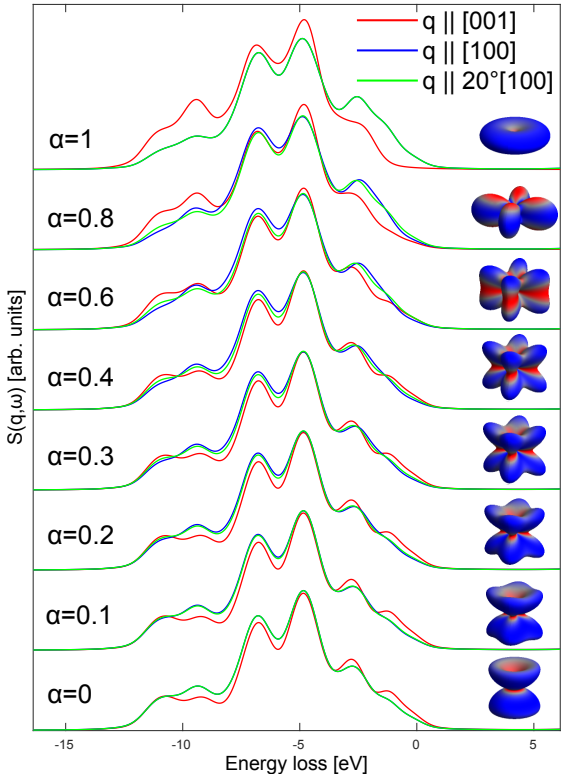

(b) XRS $N_{4,5}$ edges.

Figure 6.12: Simulations of the XAS (a) and XRS (b) spectra of the state $\Gamma_7^1 = \alpha\,|\pm 5/2\rangle + \sqrt{1-\alpha^2}\,|\mp 3/2\rangle$ as a function of the mixing parameter α. XRS is sensitive also to the in plane dichroism. From the density of the state plotted in figure (b) it is possible to see that α is related to the elongation of the orbital along the c axis. For $\alpha = 0$ the state is a pure $|\pm 3/2\rangle$, while for $\alpha = 1$ is a pure $|\pm 5/2\rangle$.

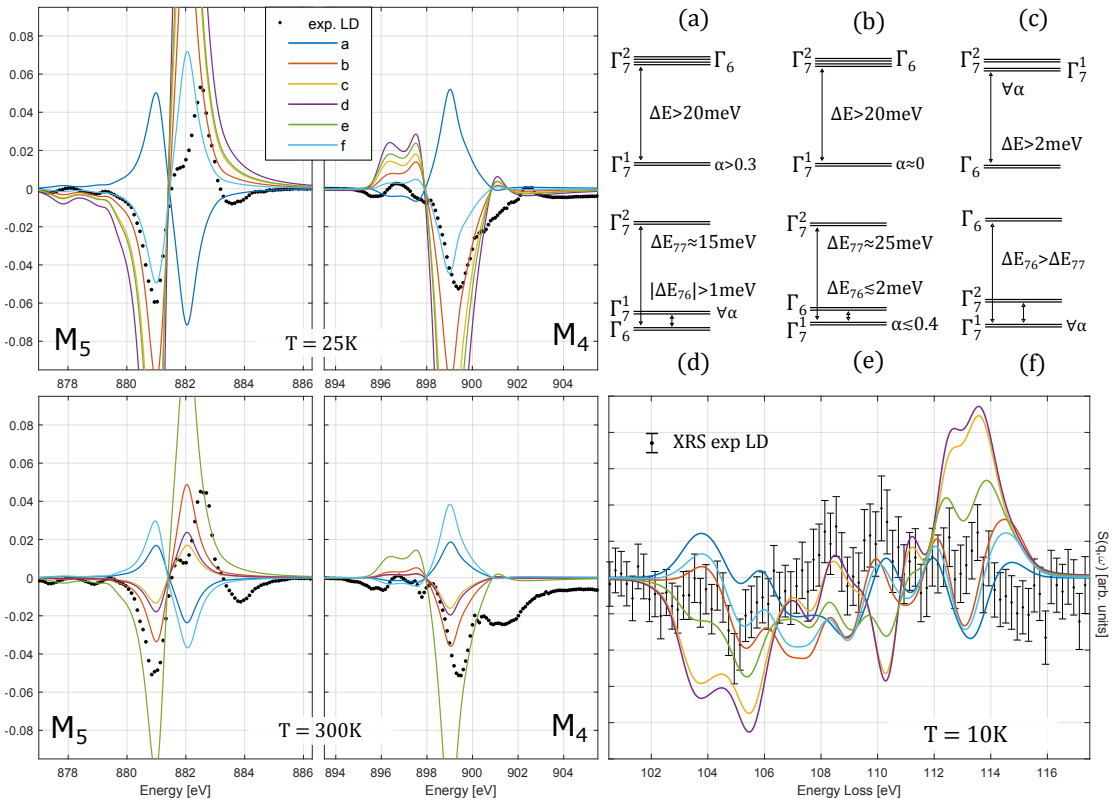

Figure 6.13: Comparison of the experimental XAS and XRS LD with the simulations for the sketched crystal field states schemes (a) to (f). The comparison of the XAS spectra, which contain less features with respect to XRS, is more straightforward. For the configuration (a) the simulated XAS LD has an opposite sign. In the scheme (b) the dichroism has the correct sign, but the intensity is too high and the XAS spectrum at 300 K cannot be reproduced. (c) has the correct sign but with too high intensity. (d) the relative intensity of the XAS LD at 25 K is too high $\forall\alpha$. (e) the XAS LD at 25 K is too intense. (f) the XAS at 25 K can be reproduced for $\alpha = 0.3$ (the plotted simulation)but the spectra at 300 K has a dichroism of opposite sign. Also this configuration can be excluded $\forall\alpha$.

The configurations where the GS is a doublet lying far in energy below the other two quasi degenerate doublets can be excluded. This means that configurations with the higher lying states at different distances from the ground state have to be considered. Also in this case some configurations can be excluded. For example, also the following configurations, sketched in figure 6.13, have to be excluded:

☒ (d) $\Gamma_6 - \Gamma_7^1 - \Gamma_7^2$ if $|\Delta E_{76}|$ is higher than $1\,\mathrm{meV}$ the relative intensity of the XAS LD is too high $\forall\alpha$.

☒ (e) $\Gamma_7^1 - \Gamma_6 - \Gamma_7^2$ with $\alpha \lesssim 0.4$ and at the same time $\Delta E_{76} \lesssim 2\,\mathrm{meV}$ the XAS LD at $25\,\mathrm{K}$ is too intense.

☒ (f) $\Gamma_7^1 - \Gamma_7^2 - \Gamma_6$ the XAS LD at $300\,\mathrm{K}$ cannot be reproduced $\forall\alpha$.

The same conclusions can be drawn through the comparison of the XRS spectra. Consider in detail the case (d) in which Γ_6 is the ground state. In figure 6.14 the XAS experimental data are shown and compared to the simulations of the configuration sketched in the inset of the figure. The configuration $\Gamma_6 \overset{1}{\longleftrightarrow} \Gamma_7^1 \overset{15}{\longleftrightarrow} \Gamma_7^2$ with $\alpha \approx 1$, where the symbol $\overset{\mathrm{meV}}{\longleftrightarrow}$ represents the difference in energy between the excited levels and the ground state in meV, reproduces the LD at $25\,\mathrm{K}$, while the LD at $300\,\mathrm{K}$ has the opposite sign. This is clear when looking again at the dichroism of the pure $|\pm 5/2\rangle$ state in figure 6.10. From this configuration, both an increase of $|\Delta E_{76}|$ and a decrease of α would result in a too intense LD at $25\,\mathrm{K}$.

To reach a possible solution it is thus reasonable, looking at the pure J_z and Γ_7^1 simulations, to suppose that $|\Delta E_{76}|$ should be smaller and simultaneously α should decrease in order to reproduce the LD at $25\,\mathrm{K}$. If ΔE_{76} is positive instead, the configuration is $\Gamma_7^1 - \Gamma_6 - \Gamma_7^2$ and this is going to be analyzed in detail in the following.

Between the two configurations there is a configuration (g) $\Gamma_7^1 \equiv \Gamma_6 - \Gamma_7^2$ with $\alpha = \sqrt{5/6} \approx 0.91$ and the resulting ground state quartet has cubic symmetry. In compounds with cubic symmetry as for CeB_6 [47], the ${}^2F_{5/2}$ multiplet is split in a doublet and a quartet. α is fixed to the value $\sqrt{5/6}$, the parameter $A_2^0 = 0$ and the ratio between A_4^0 and A_4^4 is constant. In figure 6.15 are compared both the XAS and XRS LD for this configuration with the experimental spectra. As expected, the XAS cannot resolve a cubic symmetry. The simulated XRS spectra is not totally incompatible with the experimental one but this perfectly cubic crystal field has to be discarded.

The ground state would have cubic symmetry also in the case in which the doublet Γ_7^1 is the ground state with $\alpha \approx 0.4$, as can be understood from the density plot in figure 6.12.(b).

The remaining possible configuration $\Gamma_7^1 - \Gamma_6 - \Gamma_7^2$ is considered now in detail. From the cubic crystal field scheme, in order to get the correct XAS dichroism at $25\,\mathrm{K}$, α has to decrease. While simultaneously ΔE_{76} has to increase. At the same time in order to obtain the correct behaviour at $300\,\mathrm{K}$ ΔE_{77} has to decrease. Continuously modifying the configuration in this way yields a set of possible solutions that cannot be discarded:

☑ (A) $\Gamma_7^1 \overset{0.1}{\longleftrightarrow} \Gamma_6 \overset{32}{\longleftrightarrow} \Gamma_7^2$ with $\alpha = 0.8$ is shown in figure 6.16.

☑ (B) $\Gamma_7^1 \overset{0.9}{\longleftrightarrow} \Gamma_6 \overset{25}{\longleftrightarrow} \Gamma_7^2$ with $\alpha = 0.64$ is shown in figure 6.17.

☑ (C) $\Gamma_7^1 \overset{3}{\longleftrightarrow} \Gamma_6 \overset{14}{\longleftrightarrow} \Gamma_7^2$ with $\alpha = 0.45$ is shown in figure 6.16.

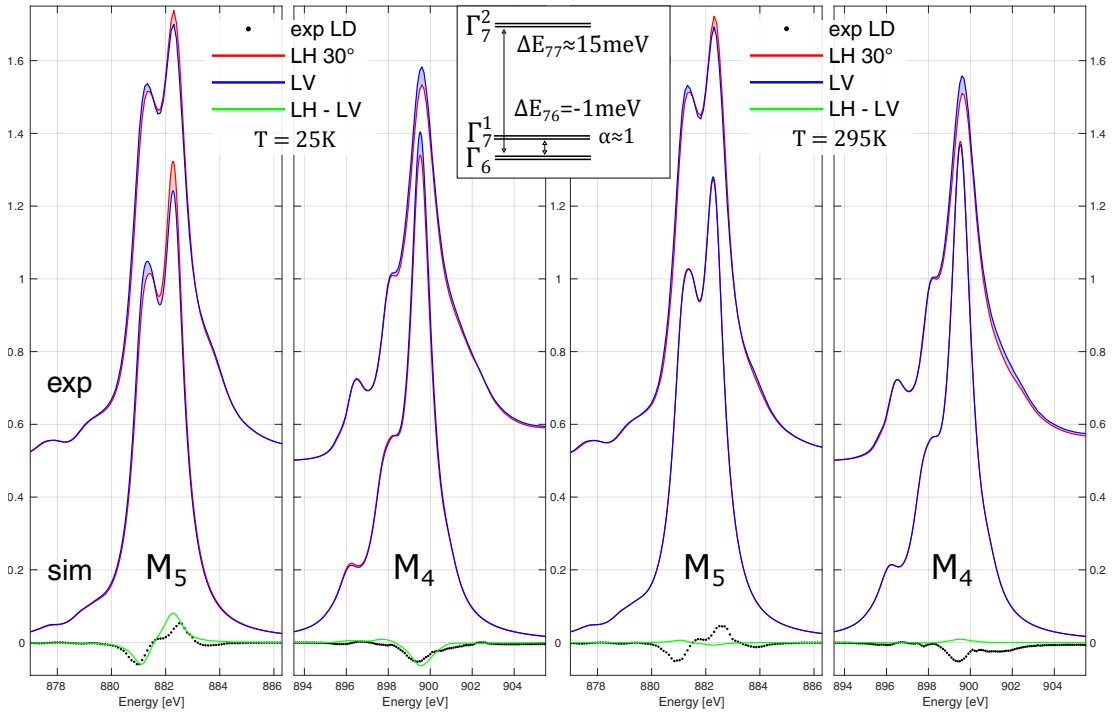

Figure 6.14: XAS simulated spectra versus experimental one for a CF scheme as in the inset: $\Gamma_6 - \Gamma_7^1 - \Gamma_7^2$. This configuration does not reproduce the spectra at 300 K. If $|\Delta E_{76}| > 1\,\text{meV}$ the dichroism in the spectrum at 25 K would be too intense $\forall\alpha$. The same behaviour for same splitting and smaller alpha. A smaller ΔE_{77} would result in a very small dichroism at 300 K.

All these states and the one in between give a correct reproduction of the XAS LD at both $25\,\text{K}$ and $300\,\text{K}$. There are some discrepancies common in all the simulations: the features in the experimental dichroism peaked at $883.5\,\text{eV}$ and $901\,\text{eV}$ could not be reproduced. These features are at the position of the $4f^0$ peaks, which are not considered in the simulations. Moreover the features in the energy range $894\,\text{eV}$-$898\,\text{eV}$ could not be reproduced. In the simulations a negative dichroism for the peak at $899.5\,\text{eV}$ is incompatible with a negative dichroism in the above-mentioned range. For what concerns the kink at $882\,\text{eV}$, in the simulations there is a change of slope but it is not as marked as in the experimental dichroism.

The XRS simulations do not predict all the features of the experimental dichroism at the same time. However, none of the spectra in figures 6.16, 6.17 and 6.18 shows big discrepancies that allow to undoubtedly discarded one.

Figure 6.19 summarizes the result of this discussion. For a given triad of α, ΔE_{76} and ΔE_{77}, through the equations 2.21 and 2.22 the values of the three crystal field parameters A_2^0, A_4^0 and A_4^4, that give that mixing parameter and those splittings can be calculated. A crystal field scheme as the one sketched in figure 6.19.(a) is proposed: $\Gamma_7^1 - \Gamma_6 - \Gamma_7^2$ where the mixing parameter is $0.35 \lesssim |\alpha| \lesssim 0.8$, $\Delta E_{76} = E_{\Gamma_6} - E_{\Gamma_7^1}$ is $0 \lesssim \Delta E_{76} \lesssim 6\,\text{meV}$ and $\Delta E_{77} = E_{\Gamma_7^2} - E_{\Gamma_7^1}$ is $13 \lesssim \Delta E_{77} \lesssim 35\,\text{meV}$. The parameters are not free to vary inside these intervals but they are such that as $\alpha \uparrow$ increases, then $\Delta E_{76} \downarrow$ decreases and $\Delta E_{77} \uparrow$ increases.

Supposing that linearly varying $(\alpha, \Delta E_{76}, \Delta E_{77})$ between the aforementioned boundary values $(0.35, 6\,\text{meV}, 13\,\text{meV}) \rightarrow (0.8, 0\,\text{meV}, 35\,\text{meV})$ and solving the system of

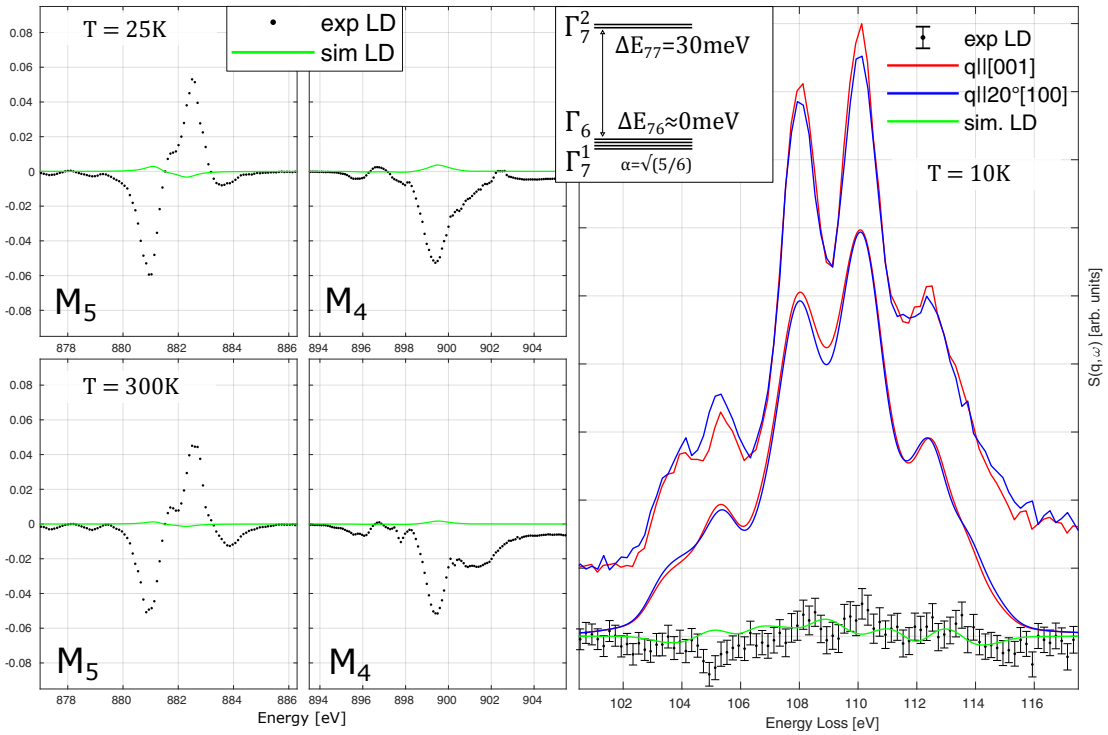

Figure 6.15: Simulation of the dichroism for an almost perfectly cubic crystal field and configuration (g) $\Gamma_7^1 \equiv \Gamma_6 - \Gamma_7^2$ with $\alpha = \sqrt{5/6} \approx 0.91$. In this case, the XAS cannot resolve the out of plane natural dichroism.

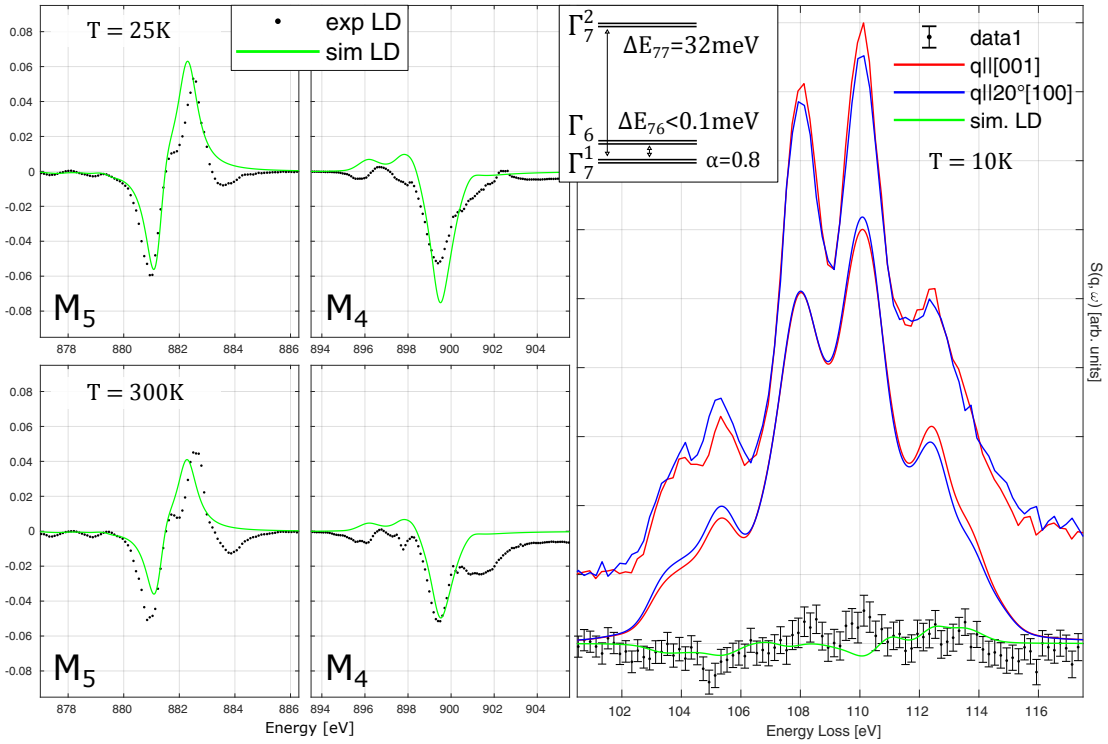

Figure 6.16: Comparison of XAS and XRS simulation for the configuration (A) $\Gamma_7^1 \overset{0.1}{\longleftrightarrow} \Gamma_6 \overset{32}{\longleftrightarrow} \Gamma_7^2$ with $\alpha = 0.8$.

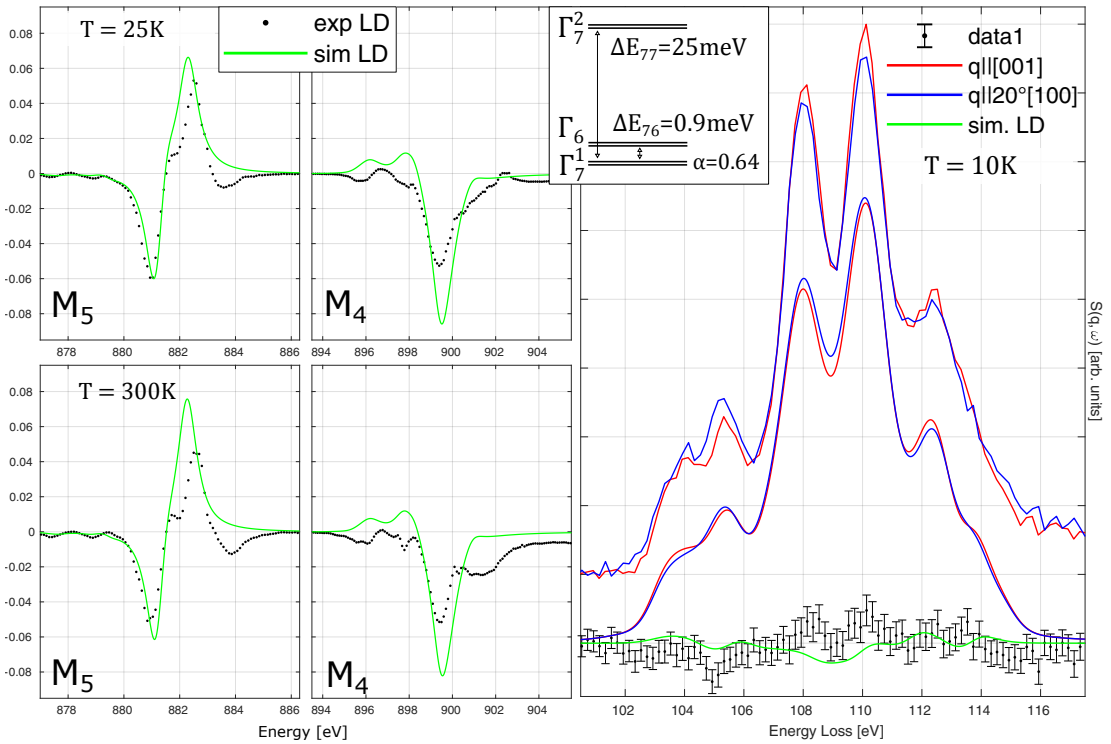

Figure 6.17: Comparison of XAS and XRS simulation for the configuration (B) $\Gamma_7^1 \overset{0.9}{\longleftrightarrow} \Gamma_6 \overset{25}{\longleftrightarrow} \Gamma_7^2$ with $\alpha = 0.64$.

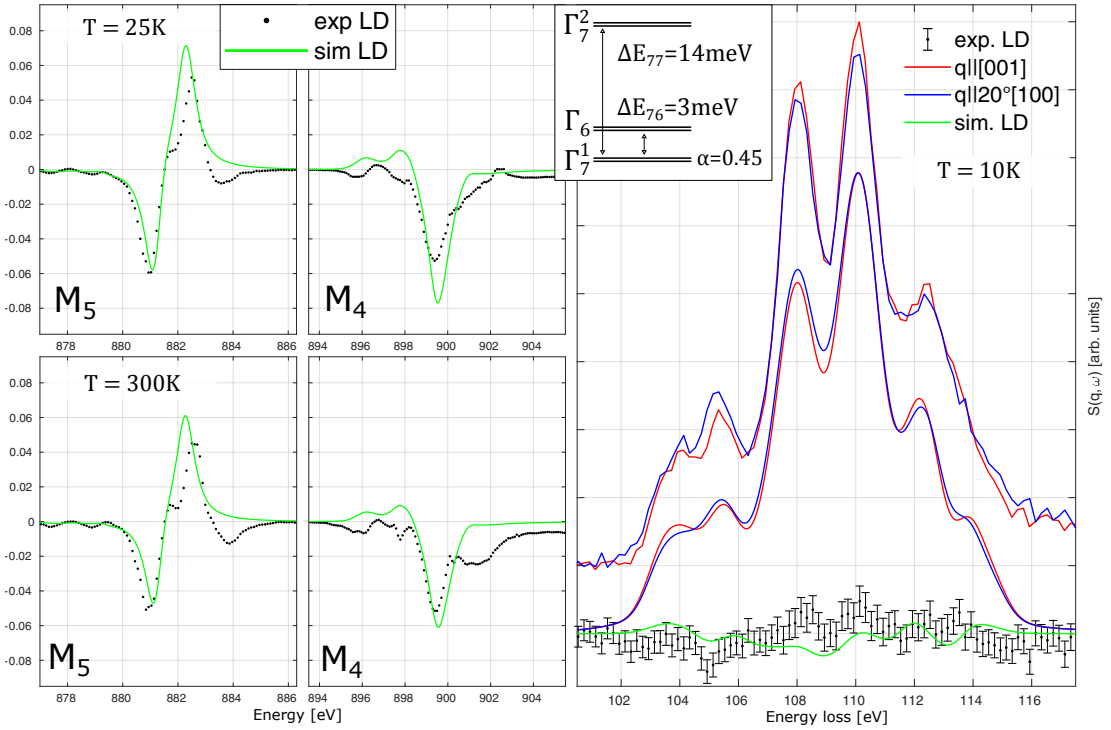

Figure 6.18: Comparison of XAS and XRS simulation for the configuration (C) $\Gamma_7^1 \overset{3}{\longleftrightarrow} \Gamma_6 \overset{14}{\longleftrightarrow} \Gamma_7^2$ with $\alpha = 0.45$.

equations, the values centered on the blue circles in figure 6.19 are obtained. This is the *qualitative* set of the possible crystal field parameters. A_2^0 is the only parameter that is well bounded: it is negative and $-25\,\mathrm{meV} < A_2^0 < -10\,\mathrm{meV}$. If A_4^0 is positive, it is not higher than $25\,\mathrm{meV}$, but a negative value down to $\approx -100\,\mathrm{meV}$ is compatible with the results. The parameter A_4^4 is bounded in a big interval: $20\,\mathrm{meV} < A_4^4 < 100\,\mathrm{meV}$ and its sign could not be determined with the performed experiments.

For the predicted values of alpha, the expectation value of the angular momentum operator along z on the ground state level $\langle \Gamma_7^1(+)|J_z|\Gamma_7^1(+)\rangle$ is bounded between -1.01 and $+1.06$, values respectively for $\alpha = 0.35$ and $= 0.8$. The expectation value of the ground state crosses zero at exactly $\alpha = \sqrt{3/8} = 0.6124$, a value close to the simulation in figure 6.17.

6.3.2 Mean squared error approach

An alternative approach to find the best crystal field parameters, that reproduce the experimental spectra, is based on the iterative calculation of the total mean squared error between the experimental spectra and the simulated spectra. In particular, simulations of the XAS dichroism were performed varying the crystal field parameters in the intervals $(-0.04 \leq A_2^0 \leq 0.02\,\mathrm{eV})$, $(-0.075 \leq A_4^0 \leq 0.075\,\mathrm{eV})$ and $(0 \leq A_4^4 \leq 0.1\,\mathrm{eV})$ going from one extreme to the other of each parameter in 15 steps. Both the XAS LD at $25\,\mathrm{K}$ and at $300\,\mathrm{K}$ was simulated. The total mean squared error was calculated as: $\mathrm{MSE}_{tot} = \mathrm{MSE}_{25\,\mathrm{K}} + \mathrm{MSE}_{300\,\mathrm{K}}$, where $\mathrm{MSE} = \sum_E (\mathrm{LD}_E^{exp} - \mathrm{LD}_E^{sim})^2/(\#E)$, where E indexes the energy values at which the experimental spectra were acquired. A small MSE_{tot} means a good agreement of the simulation with the experimental data.

In figure 6.20 the result of the calculations are shown. The mean squared error for a given combination (A_2^0, A_4^0, A_4^4) is represented as point. The dimension of the point is proportional to the inverse of the MSE_{tot}. Also, the color of the points vary from blue to yellow proportionally to the inverse of MSE_{tot}. The points corresponding to a too high MSE (too small dimension) were omitted for clarity.

In the figure the points corresponding to the configurations labeled as (A), (B) and (C) of figure 6.16, 6.17 and 6.18 are also plotted.

The region of crystal field parameters, that best fit the experimental linear dichroism, obtained in this way shows a good agreement with the conclusions drawn in section 6.3.1. However, due to the discrepancies between the simulated and the experimental spectra, pointed out in the previous section, these calculations should be considered just as a qualitative result.

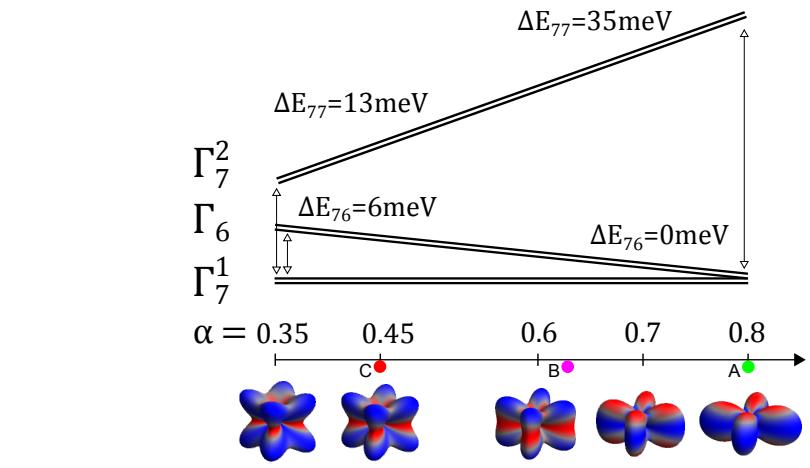

(a)

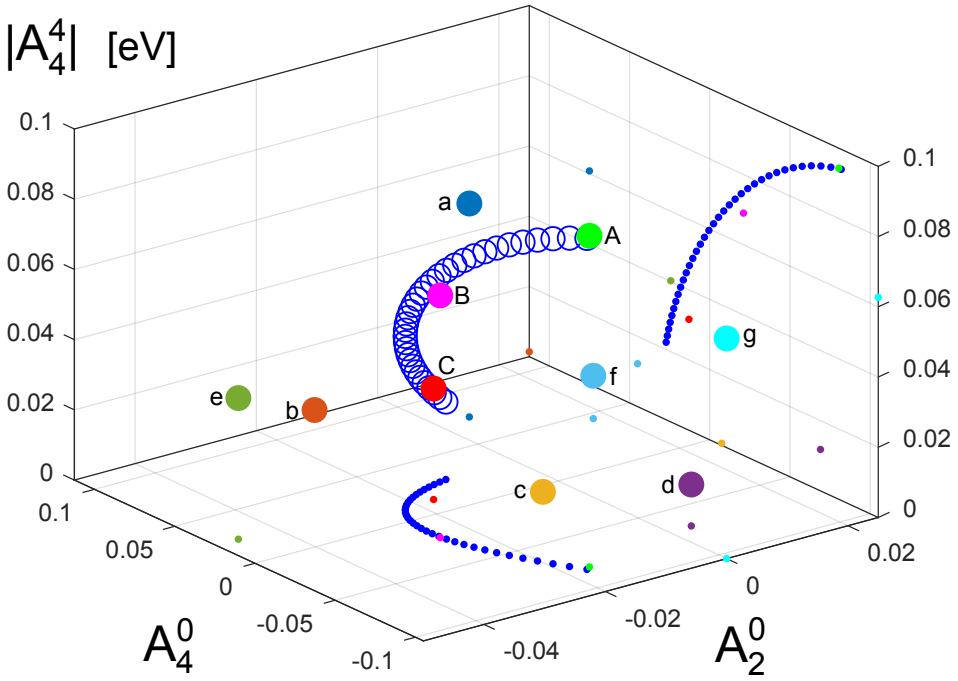

(b)

Figure 6.19: Summary of the results discussed in the chapter. A crystal field scheme as the one in the scheme (a) is proposed. The three parameters are such that if $\alpha \uparrow$ increases $\Delta E_{76} \downarrow$ decreases and $\Delta E_{77} \uparrow$ increases. In figure (b) is plotted as blue circles the *qualitative* set of the possible crystal field parameters A_2^0, A_4^0 and A_4^4 that gives a crystal field scheme as the one sketched in (a). A_k^m were calculated through the solution of the system of equations 2.21 and 2.22. A linear behaviour was considered for the variation of $(\alpha, \Delta E_{76}, \Delta E_{77})$ from one to the other boundary configurations: $(0.35, 6\,\text{meV}, 13\,\text{meV}) \rightarrow (0.8, 0\,\text{meV}, 35\,\text{meV})$. The points labelled with the letters from (a) to (f) refer to the labels used in figure 6.13 to identify the different configurations that can be excluded. (g) is the configuration of figure 6.15. The points labelled as (A), (B) and (C) refer to the configurations respectively of figure 6.16, 6.17 and 6.18 that cannot be excluded. The projections of the points are inserted to clarify the dependence on the crystal field parameters.

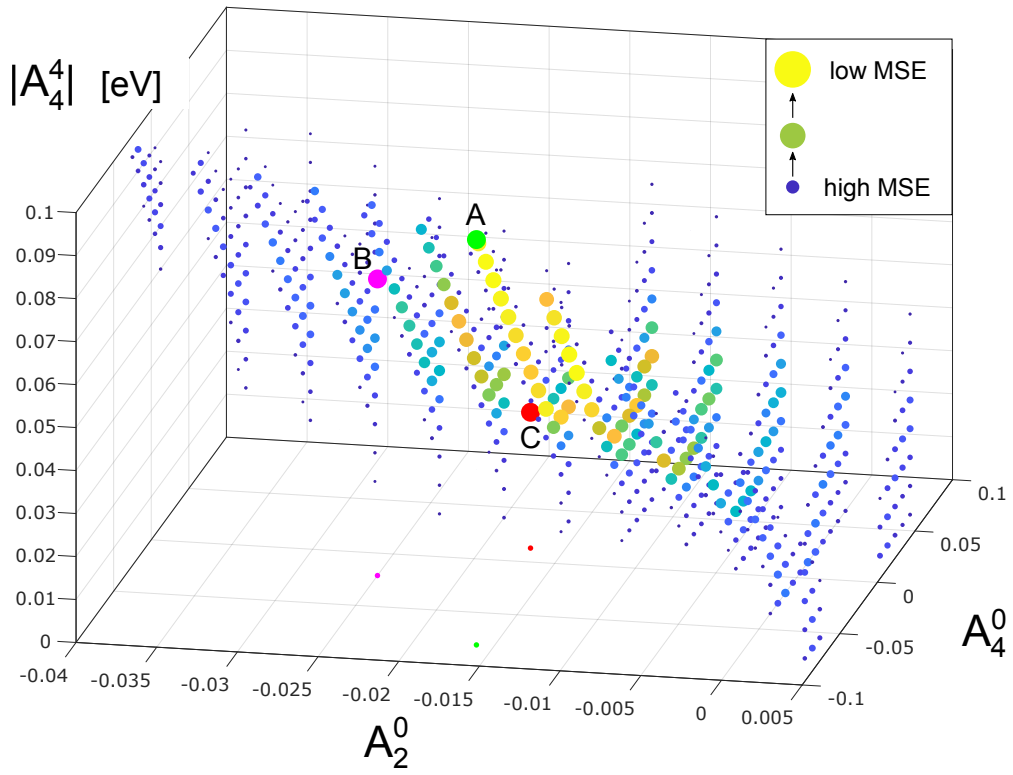

Figure 6.20: Result of the calculation of the total mean squared error calculated on the XAS spectra as: $\mathrm{MSE}_{tot} = \mathrm{MSE}_{25\,\mathrm{K}} + \mathrm{MSE}_{300\,\mathrm{K}}$, where $\mathrm{MSE} = \sum_E (\mathrm{LD}_E^{exp} - \mathrm{LD}_E^{sim})^2/(\#E)$, where E indexes the energy values at which the experimental spectra were acquired. The crystal field parameters were varied in the intervals $(-0.04 \leq \mathrm{A}_2^0 \leq 0.02\,\mathrm{eV})$, $(-0.075 \leq \mathrm{A}_4^0 \leq 0.075\,\mathrm{eV})$ and $(0 \leq \mathrm{A}_4^4 \leq 0.1\,\mathrm{eV})$ going from one extreme to the other of each parameter in 15 steps. A low MSE_{tot} means a good agreement of the simulations with the experimental data. The dimension of the points is proportional to the inverse of the MSE_{tot}. Also, the color of the points vary from blue to yellow proportionally to the inverse of MSE_{tot}. The points corresponding to a too high MSE (too small points) were omitted for clarity. The points labeled as (A), (B) and (C) correspond to the configurations of figure 6.16, 6.17 and 6.18 (their dimension is not related to their MSE). The region of crystal field parameters that best fit the experimental data are in agreement with the results shown in section 6.3.1.

CHAPTER 7

Discussion of the results and outlook

In this thesis the newly investigated heavy fermion system $CeRh_2As_2$ was analyzed. The goal of the research was to provide an independent determination of the crystal electric field (CEF) scheme and crystal electric field parameters acting on the rare earth Ce ion starting with the mere knowledge of its crystal structure. The determination of the CEF scheme was carried out using x-ray absorption at the $M_{4,5}$ edge and x-ray Raman scattering spectroscopy at the $N_{4,5}$ edge (XAS and XRS), described in chapter 3. The symmetry reduction due to the presence of the neighbouring atoms causes the presence of a natural out of plane linear dichroism that is observed in the experimental spectra acquired with these techniques. In XAS the spectra depends on the direction of the linear polarization vector. In XRS the dependence is on the direction of the exchanged momentum vector. The experiments were performed respectively at ID32 and ID20 of the ESRF. These techniques proved to be able to give information about the sample CEF scheme. To extract the information, the experimental spectra were compared to atomic multiplet simulations performed with Quanty, presented in chapter 5.1. The atomic approach is justified by the fact that the f electrons are strongly localized at the crystallographic Ce site. The atomic model was shown in chapter 5.2 to provide a correct prediction of the multipolar transitions of the $N_{4,5}$ edge of Ce. The interaction of the ion with the surrounding ions in the crystal can be modeled as an effective crystal field Hamiltonian and inserted as a perturbation to the Hund's rule ground state (chapter 2.1). The complex crystal environment is modeled as a single Ce ion, which interacts with an effective CEF described by three crystal field parameters A_2^0, A_4^0 and A_4^4. A combination (A_2^0, A_4^0, A_4^4) of these parameters uniquely determines the crystal field scheme, that is described by the three quantities ($\alpha, \Delta E_{76}, \Delta E_{77}$).

Through the analysis presented in chapter 6.3 the CEF scheme was determined to be such that:

- CEF scheme: $\Gamma_7^1 - \Gamma_6 - \Gamma_7^2$
- mixing parameter: $0.35 \lesssim |\alpha| \lesssim 0.8$
- $\Delta E_{76} = E_{\Gamma_6} - E_{\Gamma_7^1}$ is $0 \lesssim \Delta E_{76} \lesssim 6\,\mathrm{meV}$
- $\Delta E_{77} = E_{\Gamma_7^2} - E_{\Gamma_7^1}$ is $13 \lesssim \Delta E_{77} \lesssim 35\,\mathrm{meV}$

The parameters are not free to vary inside these intervals but they are such that as $\alpha \uparrow$ increases, then $\Delta E_{76} \downarrow$ decreases and $\Delta E_{77} \uparrow$ increases as sketched in figure 6.19a.

The main conclusion is that the first CEF excited state is close to the CEF ground state leading to a quasi-degenerate quartet as ground state. This result is compatible with the results obtained from the measurements of the physical properties (specific heat, entropy, susceptibility and resistivity) of this material [75]. In particular the measurements of the entropy as a function of the temperature suggested the presence of a quasi degenerate quartet ground state. This sample rose interest because of the possible presence of a quadrupolar quantum critical point (QCP). There are very few examples of Ce compounds of tetragonal symmetry showing quadrupolar ordering [76]. Most of them are of cubic symmetry as CeB_6 [47, 77] shown in figure 2.3. The ground state in that case is the Γ_8 quartet and the presence of the quartet allows a quadrupolar ordering. Similarities were found with the heavy fermion system $CeCu_2Si_2$ for what concerns the behaviour close to a quantum critical point. Quadrupolar QCP are poorly studied and poorly understood but are an emergent topic. Moreover, this sample shows an unconventional superconductivity phase close to the QCP that could be an heavy fermion superconductivity. In addition, the non centrosymmetric local environment of each layer of the material could lead to new exotic phenomena [78].

Another conclusion is that the crystal field parameter A_2^0 is negative and bounded between $-25\,\mathrm{meV} < A_2^0 < -10\,\mathrm{meV}$. This parameter is related to an oblate or prolate shape of the orbital and to the presence of a magnetic hard or easy axis [20, 79] (a different CEF parameters convention is used [80]). A negative A_2^0, means that the axis z is an hard axis for the orientation of the magnetic moment, which aligns more favorably in the plane. This is in agreement with the magnetic susceptibility measurements that show a higher in plane susceptibility with respect to the out of plane susceptibility. Moreover, the closer this parameter is to zero, the more the crystal field is close to a cubic symmetry.

Combining the information coming from the magnetic susceptibility measurements with the results of the presented investigations could lead to a reduction of the set of possible ground state configurations. In fact the magnetic anisotropy is related to the mixing parameter α that, as can be seen in figure 6.12, is related to the elongation of the orbital along the z axis. For example, if $\alpha = \sqrt{3/8} = 0.6124$ the state is a pure XY system with large in plane susceptibility [81].

Another relevant observation is the presence of a marked contribution in the XAS spectra from a Ce^{4+} valence due to the Kondo interaction, as can be seen in figure 6.6. The Kondo temperature is estimated, from the physical measurements, to be about $T_K \approx 30\,\mathrm{K} \approx 2.6\,\mathrm{meV}$. This value is of the order of the proposed crystal field splitting between the the ground state and the first CEF excited state. In Ref. [42] it was suggested that the atomic model is no more accurate if the Kondo temperature is of the order of the CEF splitting and the model should be extended using the Anderson

impurity model [82]. However, before changing the model there is still some work that can be done within the atomic model. The main weakness of the presented simulations is the fitting of the Slater and spin-orbit scaling parameters. A better fitting procedure could be found and some of the discrepancies observed in the XAS and XRS spectra could be solved.

XAS proved not able to give a unique solution for the crystal field configuration. XRS lead to the same conclusions. This is because these techniques can give direct information only about the ground state, and only indirectly give information about the excited CEF states through the temperature dependence of the spectra. However, in this particular case, as the splitting is very small, the excited states are populated also at the low temperatures at which the experiments were conducted.

A more detailed XRS experiment, comprising a measure of the temperature dependence of the spectra, aimed at resolving also the in plane dichroism could give a unique solution for the crystal field scheme and crystal field parameters. In this way also the sign of the mixing parameter α (and of A_4^4) could be determined. However, as explained, the scattering cross section for XRS is small and the acquisition of a spectrum requires several hours. Moreover, the sign of the parameter, which is related to the orientation of the orbital [83], was not of interest in this preliminary investigation of the CEF.

APPENDIX $\mathcal{A}$

Scaling of the Hartree-Fock parameters

The values of Slater integrals (F^k and G^k) and the values of the spin-orbit parameters (ζ_{nl}) used in the Quanty calculations presented in chapter 5.1 were obtained from atomic Hartree-Fock calculations. In particular, the values were taken from Crispy [68], a graphical user interface to generate Quanty input files, that has stored the values for several elements and for several edges. These values in most of the cases have to be reduced by a certain scaling factor in order to fit the experimental data. In the following sections it is shown how the XAS and NIXS spectra vary as a function of the scaling factors. It is shown also what information about the scaling can be obtained from the RIXS experiments. The reduction values that can be found in literature for similar compounds are usually a good starting point [47, 74, 83]. However, the deviation from the atomic value depends also on the particular crystal environment of the ion and the best values for the reduction factors change from compound to compound. The best way to fit these parameters is comparing the simulations with an experimental spectrum measured in isotropic conditions, for example through the measurement of powdered sample, or through the measurement at a temperature that ensure the fully population of the crystal field states. In this way the dependence on the crystal field parameters is removed thus reducing the number of free parameters to fit.

A.1 XAS

For the $M_{4,5}$ edge, the value of the Slater integrals are reduced scaling parameters are usually around scal_4f4f= 0.6, scal_3d4f= 0.8 respectively for the terms describing the interactions between the $4f$ electrons and the one between $4f$ and $4d$. Instead for the spin orbit parameters the scaling is usually lower and around scal_zeta4f= 0.87 scal_zeta3d= 0.97.

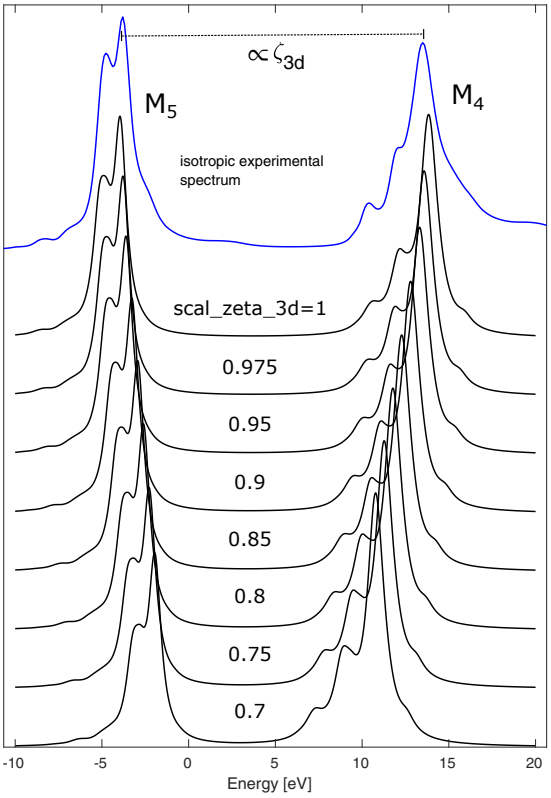

Figure A.1: Dependence of the simulated isotropic XAS $M_{4,5}$ spectra of Ce^{3+} on the scaling of the parameter ζ_{3d}. The two multiplets, corresponding to the edges M_5 on the left and M_4 on the right, correspond to the transitions respectively from the levels $3d_{5/2}$ and $3d_{3/2}$. The splitting between this two levels is linearly proportional to the spin orbit parameter ζ_{3d}. A detailed comparison with the isotropic experimental spectrum (in blue) gives the optimum value for the scaling of the Hartree-Fock value equal to scal_zeta_3d$= 0.963$.

In figure A.1, A.2 and A.3 is shown the dependence of the simulated isotropic spectra respectively on scal_zeta_3d, scal_4f4f and scal_3d4f. They are compared to the isotropic experimental data, built from the spectra acquired with an incident angle $\theta = 30°$ as: $I_{ISO} = I(\mathrm{LH})/\cos(30°) + I(\mathrm{LV})(2 - \tan 30°)$.

The scaling factors were chosen equal to: scal_zeta_3d$= 0.963$, scal_4f4f$= 0.56$ and scal_3d4f$= 0.825$.

In the XAS experiments the broadening of the two spin-orbit split multiplets is different because the core hole lifetime if different for the two holes in the states $3d_{5/2}$ and $3d_{3/2}$. A broadening of $0.8\,\mathrm{eV}$ for the M_5 and of $1.0\,\mathrm{eV}$ for the M_4 was used in the calculations.

A.2 XRS

For what concerns the XRS, an isotropic spectrum was not available. Anyway, since the the experimental data show a small anisotropy, it is reasonable to assume that the XRS experimental data shown in figure 6.9 are close to the shape of the isotropic spectrum.

The N_4 and N_5 edges are superposed and the effect of the ζ_{4d} is less visible with respect to the XAS $M_{4,5}$ edges. The same for the parameter ζ_{4f} which can be directly obtained instead from the RIXS spectra (see A.3).

In figure A.1, A.2 and A.3 is shown the dependence of the simulated isotropic spectra respectively on scal_zeta_4d, scal_4f4f and scal_4d4f, compared to the experimetnal data shown in figure 6.9.

The scaling factors were chosen equal to: scal_zeta_4d$= 0.97$, scal_4f4f$= 0.7$ and scal_4d4f$= 0.83$.

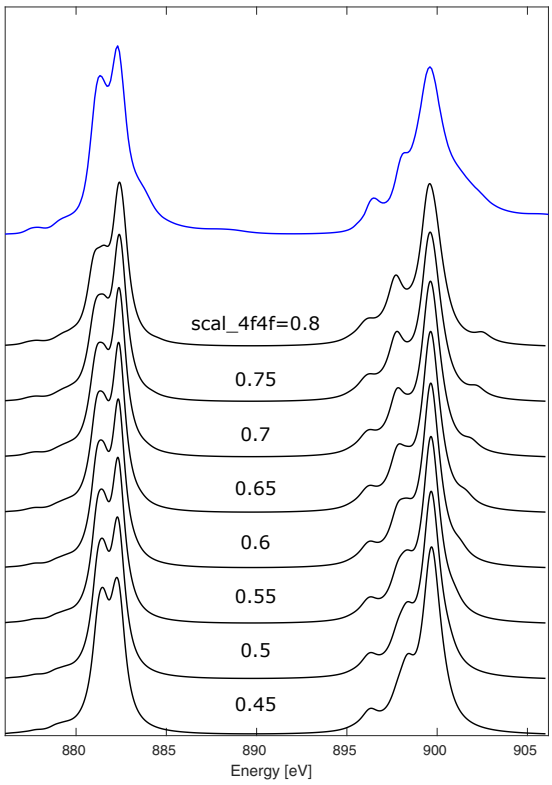

Figure A.2: Dependence of the simulated isotropic XAS $M_{4,5}$ spectra of Ce^{3+} on the scaling of the $4f4f$ Slater integrals. In blue is plotted the isotropic experimental spectra. The shape of the peaks is best reproduced for a scaling factor scal_4f4f$= 0.56$.

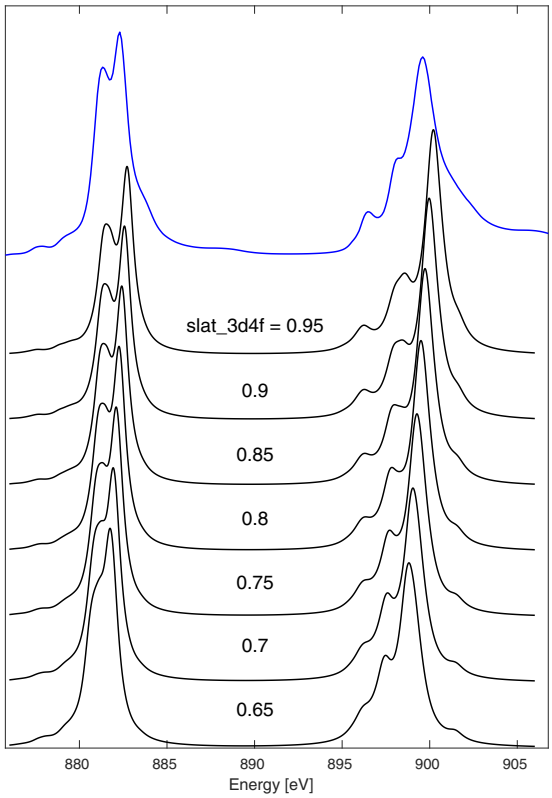

Figure A.3: Dependence of the simulated isotropic XAS $M_{4,5}$ spectra of Ce^{3+} on the scaling of the $3d4f$ Slater integrals. In blue is plotted the isotropic experimental spectra. The shape of the peaks is best reproduced for a scaling factor scal_3d4f$= 0.825$.

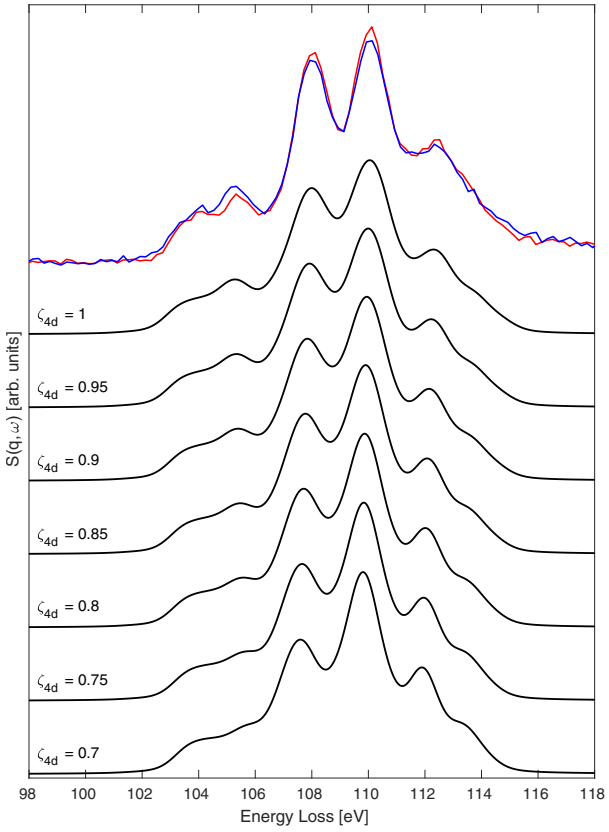

Figure A.4: Dependence of the simulated isotropic XRS $N_{4,5}$ spectra of Ce^{3+} on the scaling of the parameter ζ_{4d}. Plotted in red and blue the data presented in figure 6.9. To best reproduce the spectra a value for the reduction equal to scal_zeta_4d$= 0.97$ was chosen.

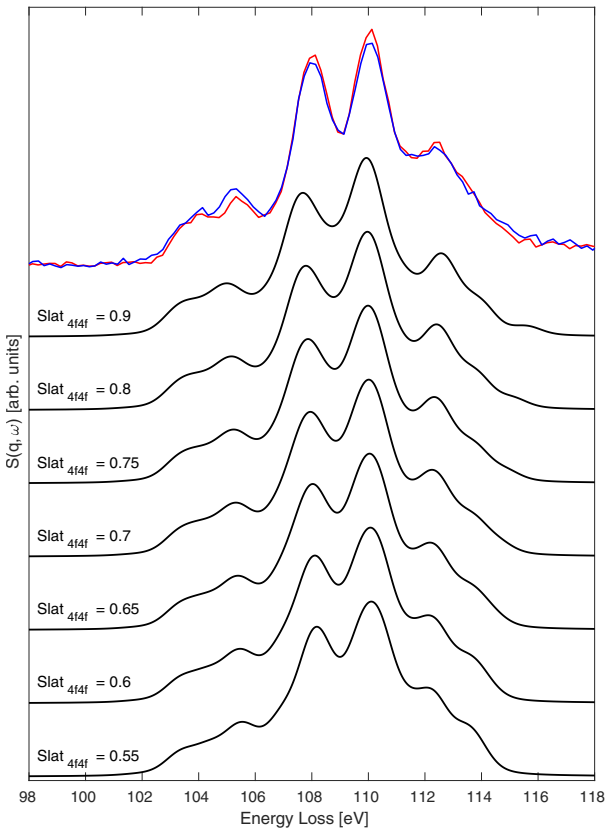

Figure A.5: Dependence of the simulated isotropic XRS $N_{4,5}$ spectra of Ce^{3+} on the scaling of the $4f4f$ Slater integrals. Plotted in red and blue the data presented in figure 6.9. To best reproduce the shape of the spectra a value for the reduction equal to scal_4f4f$= 0.7$ was chosen.

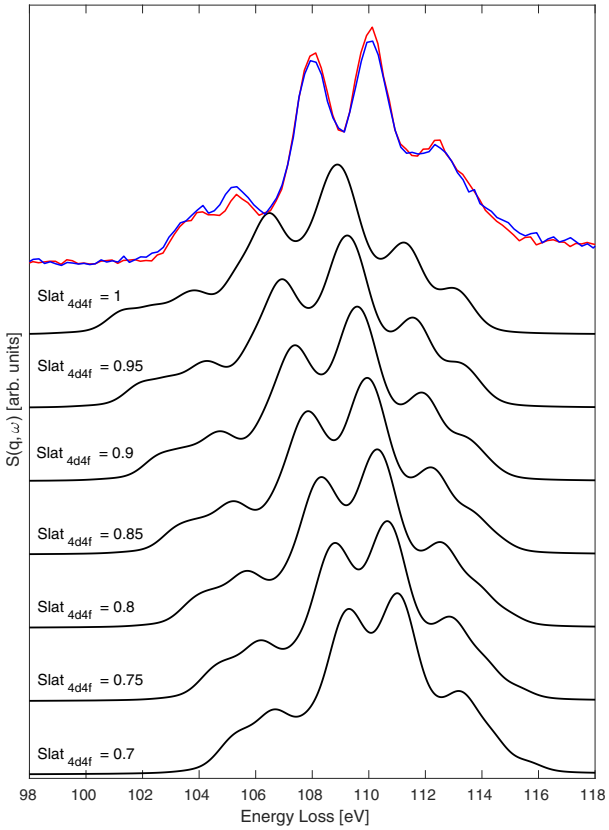

Figure A.6: Dependence of the simulated isotropic XRS $N_{4,5}$ spectra of Ce^{3+} on the scaling of the $4d4f$ Slater integrals. Plotted in red and blue the data presented in figure 6.9. The simulated spectra are all shifted arbitrarily by $115.3\,\mathrm{eV}$. To best reproduce the shape of the spectra a value for the reduction equal to scal_4d4f$=0.83$ was chosen.

A.3 RIXS

Resonant Inelastic X-ray Scattering (RIXS) measurements at the M_5 edge of Ce were performed at ID32 of the ESRF. The experimental spectra shown in figure A.7 gives directly information about the splitting between the ${}^2F_{5/2}$ and the ${}^2F_{7/2}$ multiplets. Their distance is proportional to ζ_{4f}. This allows to easily and univocally find the scaling of the ζ_{4f} parameter. It was calculated to be equal to scal_4f$=0.87$. This value was then used both in the XAS and XRS simulations.

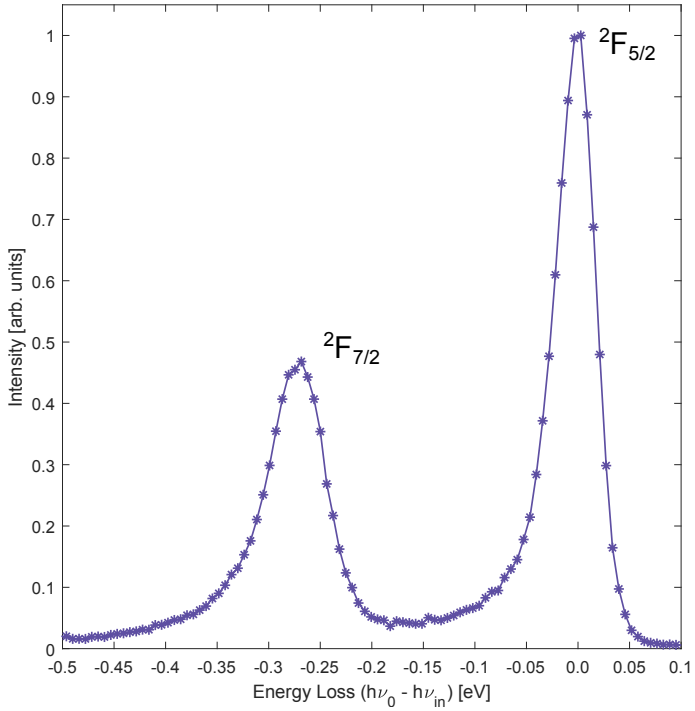

(a)

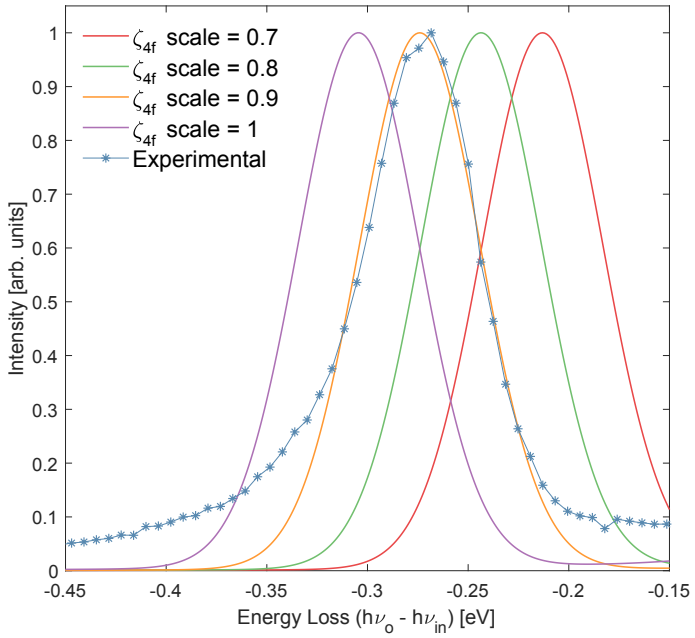

(b)

Figure A.7: (a) RIXS spectrum acquired on $CeRh_2As_2$. The peak centered at $0\,\mathrm{eV}$ energy loss is the elastic peak. Hidden below the peaks are present the contributes from the transitions between the crystal field levels of the multiplet $^2F_{5/2}$. The resolution achieved during these experiments was not enough to resolve the single peaks. (b) RIXS gives a direct measure of the splitting between the $^2F_{5/2}$ and the $^2F_{7/2}$ multiplets. The distance between the two multiplets is about $270\,\mathrm{meV}$. Fitting the spectra with the simulations allows to find the scaling of the ζ_{4f} parameter. The best fitting gives a value scal_4f$=0.87$. Courtesy of Riccardo Bona.

Bibliography

[1] Z. Fisk et al. "Heavy-electron metals". In: *Nature* 320.6058 (1986), pp. 124–129. ISSN: 1476-4687. DOI: 10.1038/320124a0. URL: https://doi.org/10.1038/320124a0.

[2] See GR Stewart. "Heavy-fermion systems". In: *Reviews of Modern Physics* 56.4 (1984), p. 755.

[3] Piers Coleman. "Heavy Fermions: Electrons at the Edge of Magnetism". In: *Handbook of Magnetism and Advanced Magnetic Materials*. American Cancer Society, 2007. ISBN: 9780470022184. DOI: 10.1002/9780470022184.hmm105. eprint: https://onlinelibrary.wiley.com/doi/pdf/10.1002/9780470022184.hmm105. URL: https://onlinelibrary.wiley.com/doi/abs/10.1002/9780470022184.hmm105.

[4] Philipp Gegenwart, Qimiao Si, and Frank Steglich. "Quantum criticality in heavy-fermion metals". In: *Nature Physics* 4 (Mar. 2008). Review Article, 186 EP. URL: https://doi.org/10.1038/nphys892.

[5] Piers Coleman. "Heavy fermions and the Kondo lattice: a 21st century perspective". In: *arXiv preprint arXiv:1509.05769* (2015).

[6] J. M. D. Coey. "Ferromagnetism and exchange". In: *Magnetism and Magnetic Materials*. Cambridge University Press, 2010, pp. 128–194. DOI: 10.1017/CBO9780511845000.006.

[7] Dai Aoki, William Knafo, and Ilya Sheikin. "Heavy fermions in a high magnetic field". In: *Comptes Rendus Physique* 14.1 (2013). Physics in High Magnetic Fields / Physique en champ magnétique intense, pp. 53–77. ISSN: 1631-0705. DOI: https://doi.org/10.1016/j.crhy.2012.11.004. URL: http://www.sciencedirect.com/science/article/pii/S1631070512001569.

[8] S Doniach. "The Kondo lattice and weak antiferromagnetism". In: *Physica B+ C* 91 (1977), pp. 231–234.

[9] WJ De Haas, J De Boer, and GJ Van den Berg. "The electrical resistance of gold, copper and lead at low temperatures". In: *Physica* 1.7-12 (1934), pp. 1115–1124.

[10] F. Steglich et al. "Superconductivity in the Presence of Strong Pauli Paramagnetism: $CeCu_2Si_2$". In: *Phys. Rev. Lett.* 43 (25 Dec. 1979), pp. 1892–1896. DOI: 10.1103/PhysRevLett.43.1892. URL: https://link.aps.org/doi/10.1103/PhysRevLett.43.1892.

[11] K. Andres, J. E. Graebner, and H. R. Ott. "$4f$-Virtual-Bound-State Formation in $CeAl_3$ at Low Temperatures". In: *Phys. Rev. Lett.* 35 (26 Dec. 1975), pp. 1779–1782. DOI: 10.1103/PhysRevLett.35.1779. URL: https://link.aps.org/doi/10.1103/PhysRevLett.35.1779.

[12] ND Mathur et al. "Magnetically mediated superconductivity in heavy fermion compounds". In: *Nature* 394.6688 (1998), p. 39.

[13] F Steglich et al. "Routes to heavy-fermion superconductivity". In: *Journal of Physics: Conference Series*. Vol. 449. 1. IOP Publishing. 2013, p. 012028.

[14] O. Stockert et al. "Magnetically driven superconductivity in CeCu2Si2". In: *Nature Physics* 7 (Dec. 2010), 119 EP -. URL: https://doi.org/10.1038/nphys1852.

[15] Thomas Willers et al. "Correlation between ground state and orbital anisotropy in heavy fermion materials". In: *Proceedings of the National Academy of Sciences* 112.8 (2015), pp. 2384–2388.

[16] O. Gunnarsson and N. E. Christensen. "Crystal-field and configuration dependence of hopping-matrix elements for $CeCu_2Si_2$". In: *Phys. Rev. B* 42 (4 Aug. 1990), pp. 2363–2367. DOI: 10.1103/PhysRevB.42.2363. URL: https://link.aps.org/doi/10.1103/PhysRevB.42.2363.

[17] G. Liu, B. Jacquier. *Spectroscopic Properties of Rare Earths in Optical Materials*. Springer, 2005.

[18] *Crystal Field Handbook*. Cambridge University Press, 2000. DOI: 10.1017/CBO9780511524295.

[19] Eva Pavarini. "Crystal-field theory, tight-binding method and jahn-teller effect". In: *Correlated electrons: from models to materials* 2 (2012), pp. 6–2.

[20] J. M. D. Coey. "Magnetism of localized electrons on the atom". In: *Magnetism and Magnetic Materials*. Cambridge University Press, 2010, pp. 97–127. DOI: 10.1017/CBO9780511845000.005.

[21] Peter Fulde. "Chapter 17 Crystal fields". In: *Alloys and Intermetallics*. Vol. 2. Handbook on the Physics and Chemistry of Rare Earths. Elsevier, 1979, pp. 295–386. DOI: https://doi.org/10.1016/S0168-1273(79)02008-0. URL: http://www.sciencedirect.com/science/article/pii/S0168127379020080.

[22] Maurits W Haverkort. "Spin and orbital degrees of freedom in transition metal oxides and oxide thin films studied by soft x-ray absorption spectroscopy". In: *arXiv preprint cond-mat/0505214* (2005).

[23] Frank De Groot. "Multiplet effects in X-ray spectroscopy". In: *Coordination Chemistry Reviews* 249.1-2 (2005), pp. 31–63.

[24] Frank De Groot and Akio Kotani. *Core level spectroscopy of solids*. CRC press, 2008.

[25] BT Thole et al. "3d x-ray-absorption lines and the 3 d 9 4 f n+ 1 multiplets of the lanthanides". In: *Physical Review B* 32.8 (1985), p. 5107.

[26] Fabio Strigari. "Hybridization and crystal-field effects in Kondo insulators studied by means of core-level spectroscopy". PhD thesis. Universität zu Köln, 2015.

[27] Andrea Amorese. "Complete characterisation of the crystal electric field in Ce Kondo lattices with resonant inelastic soft X-ray scattering". Theses. Université Grenoble Alpes, Mar. 2017. URL: https://tel.archives-ouvertes.fr/tel-01645428.

[28] J. C. Slater. "The Theory of Complex Spectra". In: *Phys. Rev.* 34 (10 Nov. 1929), pp. 1293–1322. DOI: 10.1103/PhysRev.34.1293. URL: https://link.aps.org/doi/10.1103/PhysRev.34.1293.

[29] E. U. Condon, G.H. Shortley. *The Theory of Atomic Spectra*. Cambridge University Press, 1935.

[30] R.D. Cowan. *The Theory of Atomic Structure and Spectra*. Los Alamos Series in Basic and Applied Sciences. University of California Press, 1981. ISBN: 9780520906150. URL: https://books.google.fr/books?id=tHOXLrXkJRgC.

[31] Maurits W Haverkort. *Coulomb repulsion operator (U)*. URL: http://www.quanty.org/documentation/standard_operators/coulomb_repulsion.

[32] Vinny R Sastri et al. *Modern aspects of rare earths and their complexes*. Elsevier, 2003.

[33] Jim Branson. *Parity of the Spherical Harmonics*. URL: https://quantummechanics.ucsd.edu/ph130a/130_notes/node211.html.

[34] KWH Stevens. "Matrix elements and operator equivalents connected with the magnetic properties of rare earth ions". In: *Proceedings of the Physical Society. Section A* 65.3 (1952), p. 209.

[35] J Sievers. "Asphericity of 4f-shells in their Hund's rule ground states". In: *Zeitschrift für Physik B Condensed Matter* 45.4 (1982), pp. 289–296.

[36] Hans A Bethe. "Splitting of terms in crystals". In: *Ann. Physik* 3.5 (1929), p. 133.

[37] HA Kramers. "HA Kramers, Proc. Acad. Sci. Amsterdam 33, 959 (1930)." In: *Proc. Acad. Sci. Amsterdam*. Vol. 33. 1930, p. 959.

[38] Eugene Wigner. "Über die Operation der Zeitumkehr in der Quantenmechanik". In: *Nachrichten von der Gesellschaft der Wissenschaften zu Göttingen, Mathematisch-Physikalische Klasse* 1932 (1932), pp. 546–559.

[39] Maurits W Haverkort. *Solid State Physics Mathematica package*. URL: http://www.solstatphys.org/solid_state_physics/index.php.

[40] Stefan Hufner. *Optical spectra of transparent rare earth compounds*. Elsevier, 2012.

[41] E. Borchi and S. De Gennaro. "Kondo effect in cerium intermetallics: Magnetic susceptibility". In: *Phys. Rev. B* 14 (5 Sept. 1976), pp. 1989–1994. DOI: 10.1103/PhysRevB.14.1989. URL: https://link.aps.org/doi/10.1103/PhysRevB.14.1989.

[42] P. Hansmann et al. "Determining the Crystal-Field Ground State in Rare Earth Heavy Fermion Materials Using Soft-X-Ray Absorption Spectroscopy". In: *Phys. Rev. Lett.* 100 (6 Feb. 2008), p. 066405. DOI: 10.1103/PhysRevLett.100.066405. URL: https://link.aps.org/doi/10.1103/PhysRevLett.100.066405.

[43] T Willers et al. "Crystal-field ground state of the noncentrosymmetric superconductor CePt 3 Si: A combined polarized soft x-ray absorption and polarized neutron study". In: *Physical Review B* 80.11 (2009), p. 115106.

[44] T Willers et al. "Crystal-field and Kondo-scale investigations of Ce M In 5 (M= Co, Ir, and Rh): A combined x-ray absorption and inelastic neutron scattering study". In: *Physical Review B* 81.19 (2010), p. 195114.

[45] FMF De Groot. "X-ray absorption and dichroism of transition metals and their compounds". In: *Journal of Electron Spectroscopy and Related Phenomena* 67.4 (1994), pp. 529–622.

[46] RA Gordon et al. "Orientation-dependent x-ray Raman scattering from cubic crystals: Natural linear dichroism in MnO and CeO2". In: *Journal of Physics: Conference Series*. Vol. 190. 1. IOP Publishing. 2009, p. 012047.

[47] Martin Sundermann et al. "The quartet ground state in CeB6: An inelastic x-ray scattering study". In: *EPL (Europhysics Letters)* 117.1 (2017), p. 17003.

[48] C. V. RAMAN and K. S. KRISHNAN. "A New Type of Secondary Radiation". In: *Nature* 121 (Mar. 1928), 501 EP -. URL: https://doi.org/10.1038/121501c0.

[49] KS Krishnan. "The Raman effect in X-Ray scattering". In: *Nature* 122.3086 (1928), p. 961.

[50] R Jenkins et al. "Nomenclature, symbols, units and their usage in spectrochemical analysis-VIII. Nomenclature system for X-ray spectroscopy (Recommendations 1991)". In: *Pure and applied chemistry* 63.5 (1991), pp. 735–746.

[51] Albert C Thompson, Douglas Vaughan, et al. *X-ray data booklet*. Vol. 8. 4. Lawrence Berkeley National Laboratory, University of California Berkeley, CA, 2001. URL: http://xdb.lbl.gov/.

[52] Winfried Schülke. *Electron dynamics by inelastic X-ray scattering*. Vol. 7. Oxford University Press, 2007.

[53] Luuk JP Ament et al. "Resonant inelastic x-ray scattering studies of elementary excitations". In: *Reviews of Modern Physics* 83.2 (2011), p. 705.

[54] M Blume. "Magnetic scattering of x rays". In: *Journal of Applied Physics* 57.8 (1985), pp. 3615–3618.

[55] G. van der Laan. "Nonresonant inelastic x-ray scattering from actinides and rare earths". In: *Phys. Rev. B* 86 (3 July 2012), p. 035138. DOI: 10.1103/PhysRevB.86.035138. URL: https://link.aps.org/doi/10.1103/PhysRevB.86.035138.

[56] MW Haverkort et al. "Nonresonant Inelastic X-ray scattering involving excitonic excitations: the examples of NiO and CoO". In: *Physical review letters* 99.25 (2007), p. 257401.

[57] RA Gordon et al. "High multipole transitions in NIXS: Valence and hybridization in 4f systems". In: *EPL (Europhysics Letters)* 81.2 (2007), p. 26004.

[58] R.A. Gordon et al. "Studying low-energy core-valence transitions with bulk sensitivity using q-dependent NIXS". In: *Journal of Electron Spectroscopy and Related Phenomena* 184.3 (2011). Advances in Vacuum Ultraviolet and X-ray Physics, pp. 220–223. ISSN: 0368-2048. DOI: https://doi.org/10.1016/j.elspec.2010.12.007. URL: http://www.sciencedirect.com/science/article/pii/S0368204810002781.

[59] RA Gordon et al. "Orientation-dependent x-ray Raman scattering from cubic crystals: Natural linear dichroism in MnO and CeO2". In: *Journal of Physics: Conference Series*. Vol. 190. 1. IOP Publishing. 2009, p. 012047.

[60] S. Huotari et al. "A large-solid-angle X-ray Raman scattering spectrometer at ID20 of the European Synchrotron Radiation Facility". In: *Journal of Synchrotron Radiation* 24.2 (Mar. 2017), pp. 521–530. DOI: 10.1107/S1600577516020579. URL: https://doi.org/10.1107/S1600577516020579.

[61] Jens Als-Nielsen and Des McMorrow. *Elements of modern X-ray physics*. John Wiley & Sons, 2011.

[62] Peter J. E. M. van der Linden et al. "A compact and versatile dynamic flow cryostat for photon science". In: *Review of Scientific Instruments* 87.11 (2016), p. 115103. DOI: 10.1063/1.4966270. eprint: https://aip.scitation.org/doi/pdf/10.1063/1.4966270. URL: https://aip.scitation.org/doi/abs/10.1063/1.4966270.

[63] Ch. J. Sahle et al. "Planning, performing and analyzing X-ray Raman scattering experiments". In: *Journal of Synchrotron Radiation* 22.2 (Mar. 2015), pp. 400–409. DOI: 10.1107/S1600577514027581. URL: https://doi.org/10.1107/S1600577514027581.

[64] Simo Huotari et al. "X-ray-Raman-scattering-based EXAFS beyond the dipole limit". In: *Journal of Synchrotron Radiation* 19.1 (Jan. 2012), pp. 106–113. DOI: 10.1107/S0909049511039422. URL: https://doi.org/10.1107/S0909049511039422.

[65] K Kummer et al. "The high-field magnet endstation for X-ray magnetic dichroism experiments at ESRF soft X-ray beamline ID32". In: *Journal of synchrotron radiation* 23.2 (2016), pp. 464–473.

[66] NB Brookes et al. "The beamline ID32 at the ESRF for soft X-ray high energy resolution resonant inelastic X-ray scattering and polarisation dependent X-ray absorption spectroscopy". In: *Nuclear Instruments and Methods in Physics Research Section A: Accelerators, Spectrometers, Detectors and Associated Equipment* 903 (2018), pp. 175–192.

[67] Maurits W Haverkort. *Quanty documentation*. URL: http://www.quanty.org/documentation/start.

[68] Marius Retegan. *Crispy: v0.7.2*. 2019. DOI: 10.5281/zenodo.1451209. URL: https://zenodo.org/badge/latestdoi/53660512.

[69] John J Rehr. "Theory and calculations of X-ray spectra: XAS, XES, XRS, and NRIXS". In: *Radiation Physics and Chemistry* 75.11 (2006), pp. 1547–1558.

[70] Subhra Sen Gupta et al. "Coexistence of bound and virtual-bound states in shallow-core to valence x-ray spectroscopies". In: *Phys. Rev. B* 84 (7 Aug. 2011), p. 075134. DOI: 10.1103/PhysRevB.84.075134. URL: https://link.aps.org/doi/10.1103/PhysRevB.84.075134.

[71] Maurits W Haverkort. "Quanty for core level spectroscopy-excitons, resonances and band excitations in time and frequency domain". In: *Journal of Physics: Conference Series*. Vol. 712. 1. IOP Publishing. 2016, p. 012001.

[72] FIZ Karlsruhe – Leibniz-Institut für Informationsinfrastruktur GmbH. *Inorganic Crystal Structure Database*. URL: http://www2.fiz-karlsruhe.de/icsd_home.html?&L=.

[73] "New ternary pnictides with the $CaBe_2Ge_2$-type structure in the systems, rare-earth-Rh_2Si_2 and rare-earth-Rh_2As_2". In: *Journal of the Less Common Metals* 133.2 (1987), pp. 303–311. ISSN: 0022-5088. DOI: https://doi.org/10.1016/0022-5088(87)90241-4. URL: http://www.sciencedirect.com/science/article/pii/0022508887902414.

[74] T. Willers et al. "Spectroscopic determination of crystal-field levels in $CeRh_2Si_2$ and $CeRu_2Si_2$ and of the $4f^0$ contributions in CeM_2Si_2 (M=Cu, Ru, Rh, Pd, and Au)". In: *Phys. Rev. B* 85 (3 Jan. 2012), p. 035117. DOI: 10.1103/PhysRevB.85.035117. URL: https://link.aps.org/doi/10.1103/PhysRevB.85.035117.

[75] Christoph Geibel. "A new Ce-based heavy fermion system close to a possibly multipolar Quantum Critical Point: CeRh2As2". In: *Emergent phenomena in strongly correlated quantum matter.* 2018. URL: https://youtu.be/ZgMlDuoWfFo.

[76] A Thamizhavel, R Kulkarni, and SK Dhar. "Quasi-quartet crystal electric field ground state in a tetragonal CeAg2Ge2 single crystal". In: *Physica B: Condensed Matter* 403.5-9 (2008), pp. 792–794.

[77] AM Strydom et al. "Possible field-induced quantum criticality in Ce3Pd20Si6". In: *Journal of Physics: Conference Series*. Vol. 51. 1. IOP Publishing. 2006, p. 239.

[78] Xiuwen Zhang et al. "Hidden spin polarization in inversion-symmetric bulk crystals". In: *Nature Physics* 10.5 (2014), p. 387.

[79] D Fruchart and S Miraglia. "Hydrogenated hard magnetic alloys from fundamental to applications". In: *Journal of Applied Physics* 69.8 (1991), pp. 5578–5583.

[80] M Rotter. *Crystal Field and Parameter Conventions*. URL: http://www2.cpfs.mpg.de/~rotter/homepage_mcphase/manual/node130.html.

[81] A Amorese et al. "Crystal electric field in CeRh2Si2 studied with high-resolution resonant inelastic soft x-ray scattering". In: *Physical Review B* 97.24 (2018), p. 245130.

[82] P. W. Anderson. "Localized Magnetic States in Metals". In: *Phys. Rev.* 124 (1 Oct. 1961), pp. 41–53. DOI: 10.1103/PhysRev.124.41. URL: https://link.aps.org/doi/10.1103/PhysRev.124.41.

[83] T. Willers et al. "Determining the In-Plane Orientation of the Ground-State Orbital of $CeCu_2Si_2$". In: *Phys. Rev. Lett.* 109 (4 July 2012), p. 046401. DOI: 10.1103/PhysRevLett.109.046401. URL: https://link.aps.org/doi/10.1103/PhysRevLett.109.046401.